Nanosized Iron Crystallites for Fischer-Tropsch Synthesis

Evans Itai Mabaso
BSc (Chem. Eng), MSc (Eng), UCT

Thesis submitted to the University of Cape Town
in fulfilment of the requirements
for the degree of
Doctor of Philosophy

Catalysis Research Unit
Department of Chemical Engineering
UNIVERSITY OF CAPE TOWN
Rondebosch

May, 2005

ACKNOWLEDGEMENTS

It is indeed a great pleasure to thank the many people who made this thesis a resounding success. The main credit for such support, of course, should undoubtedly go to my supervisor, Dr Michael Claeys, whose inspiring interest in the whole project, ceaseless enthusiasm in careful reading of the original manuscript and above all, his detailed and perceptive comments contributed immensely to the shape and clarity of the finished thesis. It is also difficult to overstate my gratitude to Prof. Eric van Steen whose inspiration and great efforts to explain things clearly and simply, and most of all, lots of good ideas I would have lost without him.

I am indebted to my colleagues; Ademola, Lucrécio, Velaphi, Noko, Pete, Tumelo, Cathrin, Renate, Elvera, Reagan, Mrs Rachel Cupido, just to mention a few; for providing a stimulating and fun environment in which to learn and grow.

I would like to thank Mr M. Jaffer of the Electron Microscope Unit, University of Cape Town, for the transmission electron micrographs, his patience was much appreciated. I would also like to thank Mrs H. Divey for BET measurements, her experience with the use of the machine is invaluable. I am grateful to Akzo Nobel for providing me with the much needed surfactant (Berol 050) and fully acknowledge financial support from NRF, THRIP and Sasol.

To my son, Takudzwa, I say thank you for putting a smile on my face when I so dearly needed it. You contributed in no small way to the success of this work by continually reminding me - "Daddy go and work". I still owe you the many visits to the beach that I promised but never owned up. To my mother, Eunice, your compassionate heart had to endure 10 years of my sojourning in South Africa in pursuit of higher knowledge.

Finally, and most importantly, my wife, Chengetanai, has always been my pillar, my joy and my guiding light, and above all, a great source of strength all through this work. You turned any fears of failure into desires to succeed and you taught me that "The key to success is knowing what you want and taking the initiative". I would like to dedicate this thesis to my family - my wife and son - for their love and patience

and endless encouragement despite the shortage of time together, nonetheless, our love and friendship have still deepened. This work is also dedicated to the loving memory of my father, Johnson Sanyapi, who passed away on the 18^{th} of July, 2003.

Synopsis

Fischer-Tropsch synthesis is the production of hydrocarbons from CO and H_2. The catalytically active metals for industrial application are cobalt and iron. In this work iron-based catalysts were studied. To ensure maximum metal utilisation and therefore a high weight specific catalytic activity, the metal crystallites should possess large specific surface areas and that is only achievable with small metal crystallites. However, a minimum crystallite size might exist below which catalyst activity drops. Consequently, in order to investigate the role of crystallite size on the stability, the activity and selectivity of iron based catalysts, supported catalysts with a known narrow metal crystallite size distribution were prepared via precipitation in water-in-oil microemulsions in which water-to-surfactant ratio was the main design parameter.

The study was subdivided into firstly characterisation of a suitable water-in-oil microemulsion system. Secondly preparation of nanosized oxidic iron crystallites with controlled crystallite size via precipitation in water-in-oil microemulsion. Thirdly preparation of the supported catalyst using the same but selected microemulsion systems. Finally catalyst testing under Fischer-Tropsch reaction conditions in a fixed bed reactor.

A strictly linear relationship between water-to-surfactant ratio and crystallite size was observed. The catalyst preparation technique for unsupported iron oxides resulted in uniform nanocrystallites tailored to a size range of 2-16 nm. The morphology of the crystallites on supports remained largely unchanged upon reductive pretreatment. This made catalysts prepared in microemulsions ideally suitable for investigating the effect of crystallite size during Fischer-Tropsch synthesis.

The average Fischer-Tropsch activity at the initial stages of Fischer-Tropsch experiments showed that small crystallites (<7-8 nm) were less active than their larger counterparts which showed the same metal surface specific activity. Although not

conclusively proven experimentally, this was attributed to possible oxidation of these small crystallites to supposedly inactive iron oxides. Small crystallites are suspected to readily oxidise due to water and CO_2 at Fischer-Tropsch reaction conditions. Some sintering was observed from analysis of spent catalysts, which is most likely due to inhomogeneity of crystallite distribution on the supports studied. However, the information that small crystallites result in less active catalysts is of utmost importance when designing catalysts with improved activity and lifetime which impact on the overall process economics.

Fischer-Tropsch product selectivity results generally showed some positive effects with increase of iron crystallite size, possibly due to structure sensitivity with decreasing methane selectivity, increase of chain growth probability, selectivity to long chain α-olefins and oxygenates. However, a conclusive interpretation of the selectivity data was hindered by effects of unoptimised potassium loading. Consequently, recommendations have been made with regard to improvement of catalyst preparation; especially on deposition of crystallites onto supports and the available options for optimising potassium levels in a series of catalysts to be studied.

Contents

List of Figures

List of Tables

Nomenclature

Notation		Unit
A	Absorbance	-
A_i	GC peak area of species i	-
C_{rm}	Concentration of reverse micelles in solution	mol/m^3
C_s	Concentration of the surfactant in solution	mol/m^3
$d_{c,l-TEM}$	Length based crystallite diameter from TEM analysis	m
$d_{c,v-TEM}$	Volume based crystallite diameter from TEM analysis	m
$\overline{d}_{c-BET}$	Average crystallite diameter from BET analysis	m
$\overline{d}_{c-XRD}$	Average crystallite diameter from XRD analysis	m
d_H	Hydrodynamic diameter	m
D_o	Diffusion constant	cm^2/s
f_i	Mass specific response factor used in FID analyses	-
$f_{TCD,i}$	Relative calibration factor used in TCD analyses	-
K	Empirical constant	
k	Debye-Scherrer shape factor	-
k_B	Boltzmann's constant, 1.3807 x 10^{-23}	J/K
K_{eq}	Equilibrium constant	
N_A	Avogadro's constant, 6.022 x 10^{23}	mol^{-1}
n_{ag}	Aggregation number	-
N_C	Number of carbon atoms	-
n_i	Number of moles of species i	mol
p_g	Chain growth probability	-
r_d	Rate of chain desorption	e.g. $mol/(m^2s)$
r_{FT}	Rate of formation of Fischer-Tropsch product	$\mu mole/(m^2_{Fe}\ s)$
r_g	Rate of chain growth	e.g. $mol/(m^2s)$
r_{wp}	Radius of waterpool in microemulsion	m
$S_{g,Fe}$	Specific surface area of metallic iron per gram of catalyst	m^2/g
S_{wt}	Surface area per gram catalyst	m^2/g

$S_{i,C}$	Selectivity of species i on carbon basis	C%
S_{pn}	Surface species with carbon number N	-
T	Temperature	°C
t_s	Thickness of the surfactant layer	m
V_A	Avogadro volume, 0.0224(NTP)	m^3/mol
V_{rm}	Volume of a reverse micelle	m^3
V_T	Total volume of reverse micelle solution	m^3
V_w	Volume of water in reverse micelle solution	m^3
W_N	Mass fraction of a product consisting of N carbon atoms	wt%
X_i	Molar conversion of species i	%
$Y_{i,C}$	Yield of species i on carbon basis	C-%

Subscripts	Abbreviations
ag	Aggregate
C	Carbon
c	Crystallite
d	Desorption
f	Formation
g	Growth
i	Species
rm	Reverse micelle
s	Surfactant
w	Water
wp	Waterpool
wt	Weight

Greek letters		
α	Diffusion viral coefficient	-
β	Line broadening of FWHM	radians

ϕ	Volume fraction of suspended particles	-
η	Viscosity of suspension	cp
η_o	Viscosity of suspending medium	cp
λ	Wavelength	m
λ_s	Wavelength threshold	m
θ	Diffraction angle	^{o}(degrees)
$\rho_{Fe_2O_3}$	Density of Fe_2O_3	kg/m^3
ρ_s	Density of surfactant	kg/m^3
ρ_w	Density of water	kg/m^3
ω_{wt}	Water-to-surfactant weight ratio	g/g

Abbreviations

ASF	Anderson-Schulz-Flory
BET	Brunauer-Emmett-Teller
EDX	Energy Dispersive X-ray
FTS	Fischer-Tropsch Synthesis
FWHM	Full Width at Half Maximum intensity
GC	Gas Chromatography
GHSV	Gas Hourly Space Velocity
HCNs	Hydrocarbons
HTFT	High Temperature Fischer-Tropsch synthesis
JCPDS	Joint Committee for Powder Diffraction Standards
LTFT	Low Temperature Fischer-Tropsch synthesis
NTP	Normal Temperature and Pressure, (0 °C, 1.01325 bar
SEM	Scanning Electron Microscope
TCD	Thermal Conductivity Detector
TEM	Transmission Electron Microscope
VOC	Volatile Organic Compounds

Chapter 1

Introduction

1.1 Background

The catalytic synthesis of hydrocarbons from CO and H_2 has a long history. In 1902, methane was synthesised over a nickel catalyst at atmospheric pressure (Sabatier and Senderens, 1902). In the early 1920's, Fischer and Tropsch pioneered the technology for the production of longer chain hydrocarbons from CO and H_2 using metal catalysts at high pressure of up to 300 bar (Fischer et al., 1925) and at relatively low pressures (1-5 bar) with the use of a precipitated cobalt catalyst (Fischer and Tropsch, 1926).

Fischer-Tropsch synthesis (FTS) is a practical way of converting coal and natural gas to gasoline, diesel oil, wax and chemicals such as olefins, alcohols and aldehydes (Anderson, 1984). Coal and natural gas can be converted via gasification and steam reforming processes respectively into a gaseous mixture containing mainly CO and H_2, commonly known as synthesis gas. Synthesis gas can also be produced from biogas or fast growing, renewable resources such as elephant grass (Tijmensen et al., 2002; Jun et al., 2004). In Germany the technology was used during the Second World War to produce fuel from coal. SASOL plants in South Africa have been

producing fuel and chemicals on commercial scale since 1955 using the same technology, which is now better known as Fischer-Tropsch synthesis. The enormous reserves of coal deposits and low value methane (natural gas) represents a major potential source of liquid transport fuels (Steynberg, 2004). The fuel from the Fischer-Tropsch synthesis is very clean, since the synthesis gas used in the process may only contain a few parts per billion of sulphur (Schulz, 1999). Furthermore, the diesel produced in this process has excellent combustion properties (cetane number > 60).

The Fischer-Tropsch process is not selective since it is a polymerisation process (Schulz, 1999). The product distribution shows a wide spectrum of mainly linear hydrocarbons ranging from methane to heavy waxes. The wide variety of products can be a drawback, because expensive treatment facilities are needed to separate and upgrade the Fischer-Tropsch products. If the production of liquid products from synthesis gas is desired then the technological challenge will be to maximise the selectivity towards the C_{5+} cut and minimise the formation of gases, C_1-C_4.

Recent research in Fischer-Tropsch synthesis has been aimed mainly at improving product selectivity and catalytic activity. Thus far, selectivity of CO/H_2 reactions to a single organic species, except for production of the C_1 products (CH_4 and CH_3OH), has not been accomplished. The product distribution depends on reaction temperature, total pressure, H_2/CO ratio and most importantly the nature of the catalyst (Dry, 1981; Boudart, 1984; Schulz et al., 1994). The transition metals Ni, Co, Fe and Ru have significant activity for the Fischer-Tropsch synthesis (Vannice, 1975, 1977; Vanhove et al., 1979). The selectivity changes to light products, mainly methane, with nickel as reaction temperature increases; a tendency also observed with cobalt and ruthenium but to a lesser extent. Methane selectivity also increases with increasing temperature on iron but remains at acceptable levels even at the high temperature $\approx$340 °C (Dry, 1981; Schulz, 1999). Ruthenium is the most active Fischer-Tropsch synthesis catalyst (Vannice, 1977), yet its high price and limited world resources exclude it from industrial application. Since the discovery of the

Fischer-Tropsch synthesis process, only Fe and Co have been used on a commercial scale in low temperature Fischer-Tropsch processes (220-250 °C, 25-40 bar) (Dry, 2004a). Iron has also been used as a catalyst in high temperature Fischer-Tropsch processes (330-350 °C, 25 bar) for petrol and chemical production (Anderson, 1984). Iron is much cheaper than cobalt while cobalt has a higher activity and longer life (Dry, 1993).

1.2 Crystallite size, catalyst activity and selectivity

Industrial catalysts often consist of three major components; the support, promoters and the active catalytic agent, that is, the metal, which is primarily responsible for the catalytic function. Fischer-Tropsch reaction takes place on the surface of the metal, so to ensure maximum metal utilisation and therefore high weight specific catalyst activity. A high metal surface area can be achieved with small crystallites. Loss in activity can be caused by a loss of active surface area due to crystalline growth (sintering), deposition of carbonaceous material and/or chemical poisoning of the surface, for example, by sulphur (Dry, 1981; Forzatti and Lietti, 1999; Bartholomew, 2001; Moulijn et al., 2001). Conversion of the active phase to an inert phase can also result in a loss of catalytic activity.

During Fischer-Tropsch synthesis α-Fe is carburised to iron carbides, Fe_xC, and/or oxidised to Fe_3O_4. Typically a mixture of these phases is present in a working iron catalyst. However, if α-Fe crystallites of identical size are exposed to identical reaction conditions, thermodynamically a single phase should be present. It is therefore likely that multiple phases in iron Fischer-Tropsch catalysts might be due to the presence of crystallites of widely different sizes, which are transformed into different phases at reaction conditions. Iglesia (1997) stated that for cobalt, small crystallites (d<5-6 nm) would become inactive due to oxidation of these small crystallites

by product water under Fischer-Tropsch conditions. Cobalt crystallites larger than this critical diameter were shown to display activity for Fischer-Tropsch synthesis independent of specific metal surface area and therefore no structure sensitivity with respect to activity.

A thermodynamic analysis of nanosized cobalt crystallites support the possibility that small crystallites can indeed oxidise under Fischer-Tropsch process conditions (van Steen et al., 2005). A similar behaviour might be expected for iron-based Fischer-Tropsch catalysts where the active phases are believed to be iron carbides (Mansker et al., 1999; Bian et al., 2002; Li et al., 2002). During Fischer-Tropsch synthesis, high H_2O and CO_2 partial pressures may cause the transformation of the active small metallic and/or iron carbide crystallites to the supposedly inactive oxides. The exact crystal size, at which iron might transform under reaction condition, is not yet known.

Little is known on possible structure sensitivity or crystallite size effects on selectivity in Fischer-Tropsch synthesis. According to Schulz et al. (2002), of the large number of different reactions taking place during Fischer-Tropsch synthesis, some take place on sites of low coordination (e.g. growth, CO-insertion) whereas others occur on high coordination sites (C-hydrogenation). This concept would suggest that selectivity changes are expected to be different when testing catalysts with varying crystallite sizes and therefore varying ratios of low to high coordination sites. Systematic studies on effects of crystallite size on the selectivity of Fischer-Tropsch synthesis are however not available in literature. In order to investigate possible effects of crystallite size on catalyst activity and product composition, catalysts with a known narrow metal crystallite size distribution are required. This is a challenge by itself as it is not easy to synthesize metal crystallites with a narrow size distribution and at the same time have better control of crystallite size (Figure 1.1).

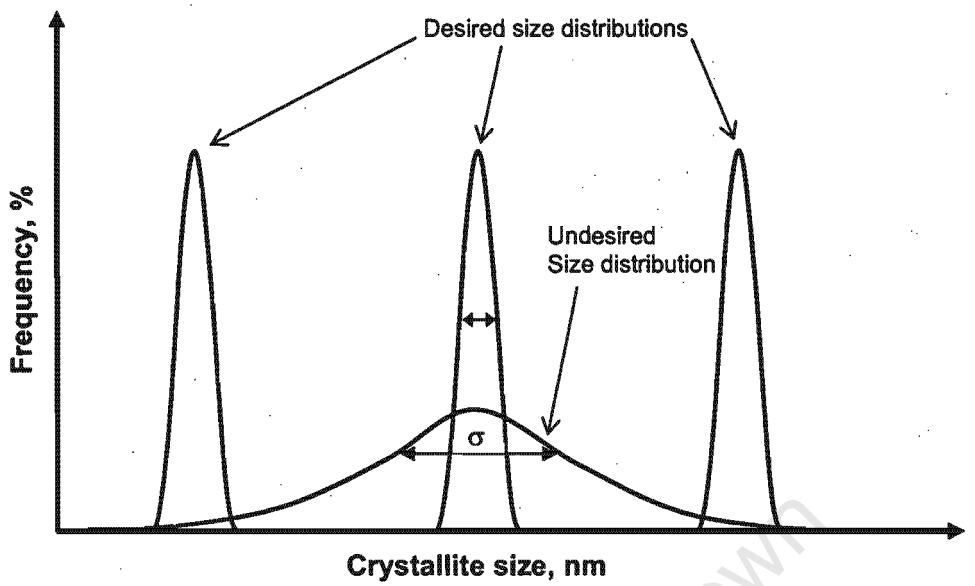

Figure 1.1: The challenge in preparing crystallites with a narrow size distribution

1.3 Nanocrystallite technology for catalyst preparation

Nanomaterials are of current interest because they mark a material transition range between molecular and bulk properties. With decreasing crystallite size, bulk properties are lost as the fraction of surface atoms becomes large (Ozin, 1992; Agostiano et al., 2000). Catalysis represents one of the single most important application of nanotechnology (Kung and Kung, 2003, 2004). The size of metal crystallites on a support might be very important to developing a catalyst, which meets the activity, stability and selectivity requirements of a particular catalytic process (Boudart, 1984; Lin et al., 1986; Abrevaya, 1990). In order to achieve a deeper understanding of the reaction mechanisms and kinetics of catalytic processes, well-defined model catalysts are an indispensable tool.

Traditionally, supported catalysts have been produced by wet impregnation using water-soluble metal salts, which results in well-dispersed catalysts with high activity and good thermal stability. The average crystallite size of the active phase is

usually in the nanometer range but with a broad size distribution. Therefore, with a wet impregnation technique there is no good control over the crystallite size formed. This then renders the interpretation of size dependent mechanistic phenomena of the catalyst impossible. Thus, it is considered important to apply a preparation technique which allows synthesis of model type catalysts. Research in recent years has shown that the so-called microemulsion technique can result in better control of the crystallite size (Pillai et al., 1995; Pileni, 2003; Eriksson et al., 2004; Capek, 2004). This technique can also be employed to prepare supported catalysts (Abrevaya and Targos, 1987; Abrevaya, 1990; Hanaoka et al., 1997; Capek, 2004) according to the preparation conditions of the microemulsions.

The aim of the present research is, therefore, to prepare model iron Fischer-Tropsch catalysts with narrow crystallite size distribution and to test the effect of crystallite size on activity and selectivity in Fischer-Tropsch synthesis.

Chapter 2

Literature Overview

2.1 The Fischer-Tropsch synthesis

The Fischer-Tropsch synthesis has a sparkling history that spans more than 80 years. It is regarded as the backbone of coal to liquid, and gas to liquid technologies. The world's enormous reserves of coal deposits and low value methane (natural gas) represent a major potential source of liquid transport fuels and chemicals. Both coal and methane can be converted through gasification and steam reforming into a gaseous mixture containing mainly hydrogen and carbon monoxide. Synthesis gas (H_2 and CO) can also be produced from fast growing, renewable resources or biogas. The overall Fischer-Tropsch process configuration is shown in Figure 2.1. The three main sections involved include: synthesis gas production, Fischer-Tropsch synthesis and product workup. The interest in Fischer-Tropsch synthesis has been growing tremendously over the last years as recent figures of process and catalyst development in this field show (van der Laan, 1999; Steynberg, 2004). Companies active in catalyst and process development in Fischer-Tropsch synthesis are *inter alia*: BP, Exxon, PetroSA, Rentech, Sasol, Shell, Statoil, Syntroleum. PetroSA, Sasol and Shell are currently using Fischer-Tropsch processes on a commercial scale, and large

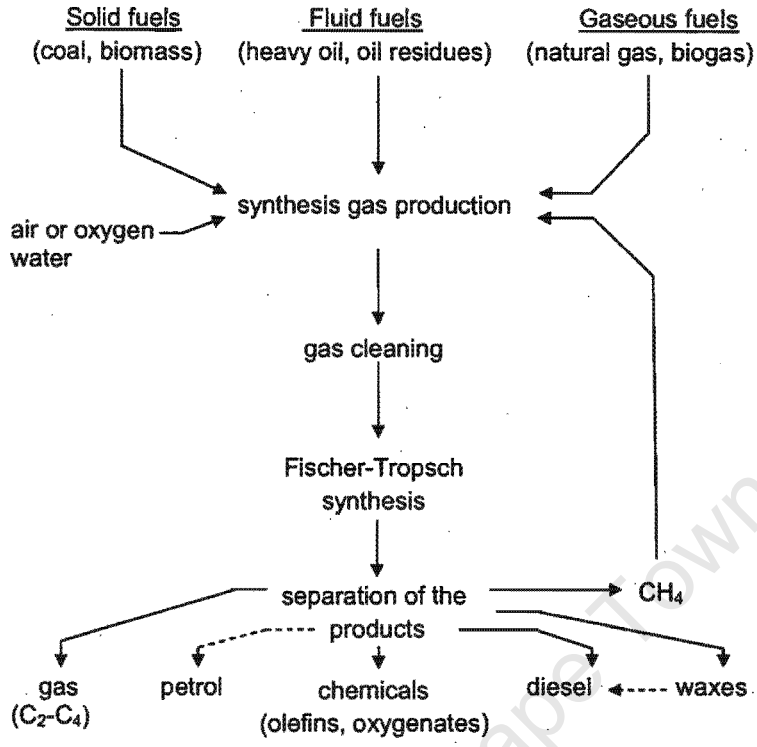

Figure 2.1: Process overview for fuels and chemicals production via Fischer-Tropsch synthesis

new plants to convert natural gas into mainly diesel fuel are currently being built (e.g. by Sasol in Qatar, (Sasol, 2003)). The diesel selectivity of the overall process can be increased by further processing of product wax via mild hydrocracking.

2.1.1 Fischer-Tropsch reaction

The highly exothermic Fischer-Tropsch reaction converts synthesis gas (H_2/CO) into a wide range of organic products, mainly linear hydrocarbons such as paraffins and olefins. The CO hydrogenation capacity of nickel and cobalt was first reported by Sabatier and Senderens in 1902. However, it was only after the pioneering work of Franz Fischer and Hans Tropsch in the 1920's that the commercial interest in the production of hydrocarbons started to grow. The stoichiometry of this polymerisation reaction implies a H_2:CO ratio of 2 for the synthesis of the hydrocarbon chain

monomer, and water is released as a primary product.

$$\text{FTS}: \quad 2H_2 + CO \Longrightarrow -(CH_2) - + H_2O \quad \Delta H_{R,270^oC} = -151.9 \text{ kJ/mol} \quad (2.1)$$

Branched hydrocarbons and oxygenates such as primary alcohols and aldehydes are also formed, but typically in minor quantities. The kind of product and its average carbon number obtained is determined by the process temperature, pressure, and the catalyst used. Typical operation conditions are 220-250 °C for production of long chain products mainly diesel and wax (Low Temperature Fischer-Tropsch Synthesis) and 320-350 °C for production of light products, petrol and chemicals (High Temperature Fischer-Tropsch Synthesis) (Dry, 2004b). Operating pressures are typically between 15 and 40 bar (Steynberg et al., 2004). Although all group VIII metals display some activity in the C-C coupling reaction during Fischer-Tropsch synthesis, the most active metals are ruthenium, iron, cobalt, and nickel (Vannice, 1975, 1977; Dry, 1981). This is related to the capacity of the metals to dissociate CO. Of these metals only cobalt and iron catalysts are used commercially.

2.1.2 Formation of CO_2

Product water can react further via water gas shift reaction:

$$\text{WGS}: \quad H_2O + CO \Longleftrightarrow CO_2 + H_2 \quad \Delta H_{R,270^oC} = -39.3 \text{ kJ/mol} \quad (2.2)$$

This side reaction is mainly catalysed by iron catalysts, cobalt has almost no water gas shift activity. However, the water-gas shift activity of iron catalysts makes them flexible towards the H_2:CO feed ratio of the synthesis gas. If the H_2:CO ratio is lower than stoichiometrically required, it can be adjusted in the reactor via the reaction of CO and H_2O produced during the FT-reaction to form additional H_2. This allows the utilization of feed-stocks with a low H_2:CO ratio such as typically obtained from gasification of coal. The water gas shift reaction is undesirable for Fischer-Tropsch

synthesis with hydrogen-rich syngas produced from natural gas as it results in low carbon efficiency in a gas-to-liquid process because carbon is lost as CO_2.

CO_2 is produced mainly by the WGS reaction, but can also be formed via the Boudouard reaction. This disproportionation of CO also leads to the formation of carbon which can cause catalyst deactivation (Dry, 2004b).

$$\text{Boudouard}: \quad 2CO \Longleftrightarrow C + CO_2 \quad \Delta H_{R,270^{\circ}C} = -172.4 \text{ kJ/mol} \tag{2.3}$$

2.2 Mechanisms of product formation

Transition metal surfaces have unique properties with regard to catalysing a sequence of complex reactions which occur in Fischer-Tropsch synthesis. The properties begin with the dissociative adsorption of CO and H_2 followed by complex rearrangements through the formation and breaking of bonds and finally desorption of the products (Dry, 1981; Anderson, 1984). Several competing reactions may all occur with similar probability, thereby reducing the selectivity to the desired products. Fischer-Tropsch synthesis is viewed as a surface polymerisation reaction in which widely recognised steps form the key sequence of reaction pathways: reactant adsorption - chain initiation - chain growth - product desorption - readsorption of reactive products and further reaction. Numerous reaction pathways have been proposed to explain the observed product distribution in the Fischer-Tropsch synthesis. These include: the surface carbide mechanism (Fischer and Tropsch, 1926), a mechanism including an enolic intermediate (Storch et al., 1951), the CO-insertion mechanism (Pichler and Schulz, 1970) and an alkenyl intermediate mechanism (Maitlis et al., 1999). Extensive reviews of these mechanisms can be found in literature (Dry, 1981; Anderson, 1984; Claeys and van Steen, 2004).

2.2.1 Proposed growth mechanisms

Figure 2.2 shows a summary of the proposed four reaction pathways. The alkyl mechanism developed on the basis of the carbide-mechanism (Fischer and Tropsch, 1926; Craxford and Rideal, 1939) is presently the most widely accepted mechanism for chain growth in the Fischer-Tropsch synthesis (Claeys and van Steen, 2004). In this mechanism CH_x species are formed after dissociative CO chemisorption, the resulting surface carbon, C (3) is subsequently hydrogenated with surface hydrogen (H) yielding, in consecutive reactions, CH (4), CH_2 (5) and CH_3 (6) surface species (Erley et al., 1983; Wang and Ekerdt, 1984; Kaminsky et al., 1986). The CO-insertion mechanism, developed by Pichler and Schulz (1970), has identical steps leading to the formation of CH_x surface species. In essence, the two mechanisms have the same chain initiator, the surface methyl species (6), but different chain propagation monomers. Chemisorbed CO (1) is the monomer in the case of the insertion mechanism whereas a CH_2 (5) surface species is regarded as the monomer for the alkyl mechanism. Chain propagation can involve CH_2 insertion (alkyl mechanism) to form an alkyl species (10) or CO-insertion in a metal-alkyl bond (7) leading to a surface acyl (8) species, which can subsequently be hydrogenated to form species (9). Chain termination reactions of these oxygen containing species leads to the formation of oxygenates (Anderson and Ekerdt, 1985; Dry, 1990). Oxygen elimination from the surface species (9) via formation of water leads to the formation of the alkyl species (10), identical to the species formed via the alkyl mechanism. Chain termination of this species occurs via H-addition yielding n-paraffins or via β-H-elimination yielding α-olefins.

With the alkenyl mechanism proposed by Maitlis et al. (1999), the vinyl surface species ($CH = CH_2$) (11), formed through the coupling of methylidyne (CH) (4) and methylene (CH_2) (5), is considered the chain initiator and the CH_2 surface species the chain propagation monomer. Product desorption in the alkenyl mechanism involves the addition of hydrogen to an alkenyl (13) species yielding α-olefins.

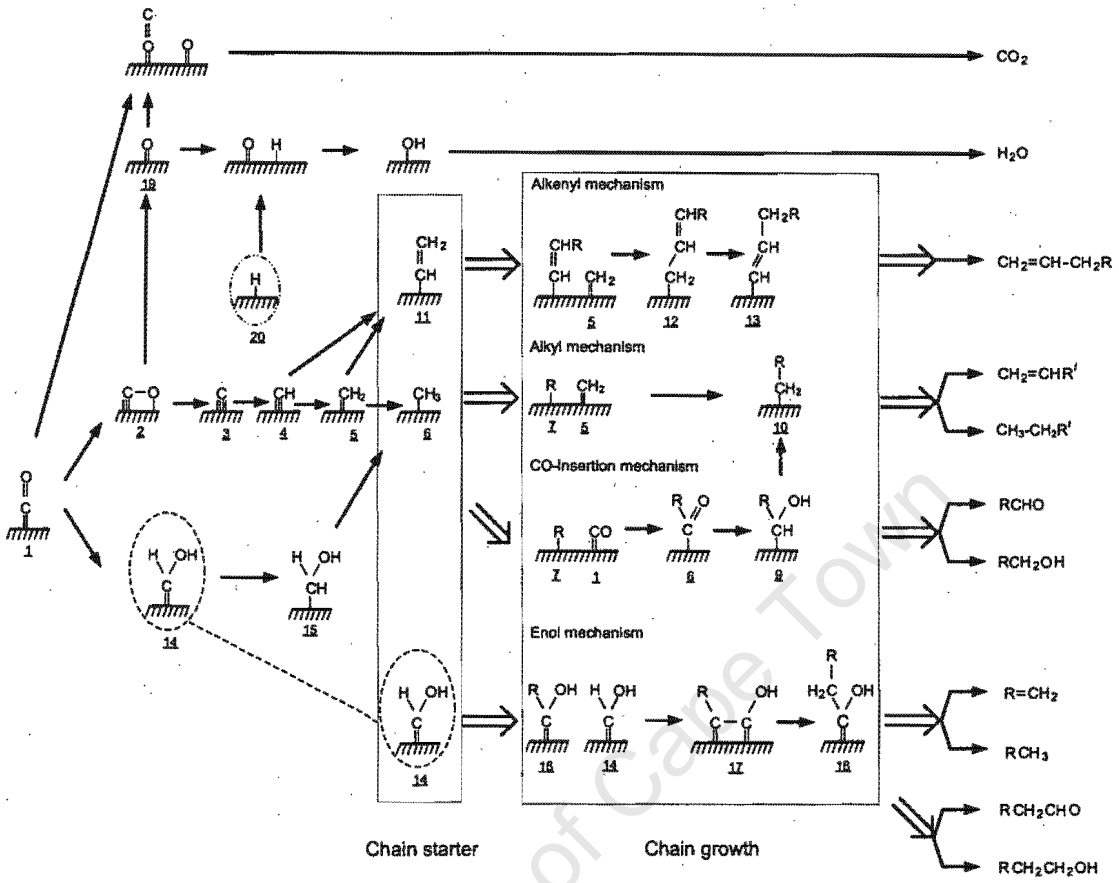

Figure 2.2: Overview of Fischer-Tropsch reaction pathways

This mechanism fails to explain the primary formation of n-paraffins and does not explain the formation of oxygenates (Claeys and van Steen, 2004). Furthermore, there is no experimental evidence for the isomerisation reaction of the allyl species (12) to form the vinyl species (13).

Another mechanism, the enolic mechanism, was proposed by Bureau of Mines Workers (Storch et al., 1951). In this mechanism, chemisorbed CO (1) is hydrogenated to form an enolic surface species (14) which is both the chain initiator and monomer. Chain growth occurs via a condensation reaction between two enol species under formation of water, and chain termination yields oxygenates or α-olefins and n-paraffins. Further hydrogenation of the enolic species (14) will lead to the formation

of surface species (15) which in turn can be converted to methyl species (6), the chain initiator for alkyl and CO-insertion mechanisms. The major drawback of the enol mechanism is that there is no experimental evidence for the existence of the enolic species.

Water is also formed in large quantities as well as carbon dioxide depending on the catalyst used. CO_2 can be formed via the reaction between the chemisorbed CO (1) and surface oxyl species (19). Water is formed by the reaction of the surface oxyl species (19) with abundantly available hydrogen species (20).

Although it fails to explain the formation of oxygenates, the carbide mechanism is the most widely accepted one. Some researchers believe that the co-occurrence of a second mechanism e.g. the CO insertion mechanism would account for the formation of oxygenates (Hindermann et al., 1993). Alternatively oxygenates might be formed via the addition of OH species to surface alkylidene species (21) (see Figure 2.3 for species 21) (Johnston and Joyner, 1993).

2.2.2 Formation of branched hydrocarbons

The alkyl mechanism described above does not account for the formation of branched hydrocarbons. However, a reaction pathway analogous to the alkyl mechanism was proposed by Schulz et al. (1970, 1988, 1990). In this reaction pathway, it was proposed that the formation of branched hydrocarbons (Figure 2.3) involves the reaction of an alkylidene surface species (21) and a methyl surface species (6) to form species (22). Schulz et al. (1970, 1988, 1990) also proposed the partial formation of branched hydrocarbons via olefins such as propene which can re-adsorbed on the penultimate carbon atom (22) and then react with methylene to form a branched surface species (23). A desorption of such species would then yield methyl branched product molecules.

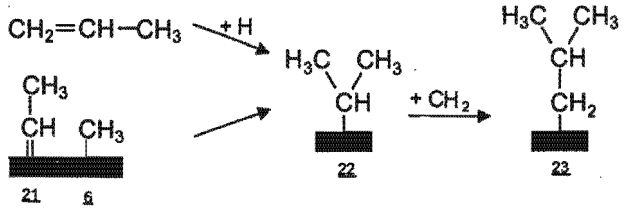

Figure 2.3: Formation of branched hydrocarbons as proposed by Schulz et al. (1970, 1988, 1990)

2.3 Fischer-Tropsch product spectrum

The Fischer-Tropsch synthesis is comparable to a conventional polymerisation process such as ethylene polymerisation resulting in a distribution of different chain-lengths of the products (Anderson, 1984). This behaviour was originally noticed by Schulz (1935) and Flory (1936). The high degree of order with repeating selectivity patterns in different carbon number fractions suggests a strict kinetic basis of this surface polymerisation with stepwise addition of a C_1 monomer species which is well suited for selectivity modelling (Friedel and Anderson, 1950; Claeys and van Steen, 2004). Neglecting the formation of oxygenates and branched hydrocarbons and making the assumption that only one sort of product Pr_N can desorb per carbon number N, one can propose a simple basic chain growth model of this polymerisation as depicted in Figure 2.4.

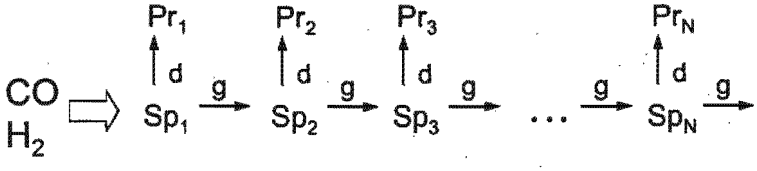

Figure 2.4: Kinetic scheme of chain growth and product desorption

Notably, the entire product spectrum can be characterised by a single parameter,

i.e., chain growth probability p_g, defined as:

$$p_g = \frac{r_g}{r_g + r_d} \tag{2.4}$$

where r_g and r_d are the rates of chain growth and desorption respectively. A mass balance around a surface species Sp_N at steady state results in the theoretical chain length distribution described by means of the so-called Anderson-Schulz-Flory (ASF) equation, which is represented as:

$$\lg\left(\frac{W_N}{N}\right) = N\lg(p_g) + \lg\frac{(1-p_g)}{p_g} \tag{2.5}$$

where W_N is the mass fraction of a product consisting of N carbon atoms. Note that a derivation of above equation is given in Appendix A; p_g is often called α in literature. Equation 2.5 implies that Fischer-Tropsch synthesis is not selective towards a single reaction product or a specific carbon range except for methane as it can be produced with 100% selectivity at a chain growth probability of zero (Dry and Oosthuizen, 1968; Anderson, 1984). Notice that higher values of p_g give higher molecular weight products (Figure 2.5). Hence, the product range is divided into the following carbon number fractions representing different possible enol products: C_1 (methane), $(C_2 - C_4)$ (gaseous hydrocarbons), $(C_5 - C_{11})$ (gasoline), $(C_{12} - C_{18})$ (middle distillate/diesel) and C_{19+} (wax).

2.3.1 Deviations from ideal distributions

The Anderson-Schulz-Flory equation presents straight lines when plotting molar product fractions (W_N/N) logarithmically over the carbon number, with the slope reflecting the chain growth probability. In distributions of real Fischer-Tropsch products often deviations from this behaviour are observed (Iglesia et al., 1993; Schulz and Claeys, 1999; Claeys and van Steen, 2004) with:

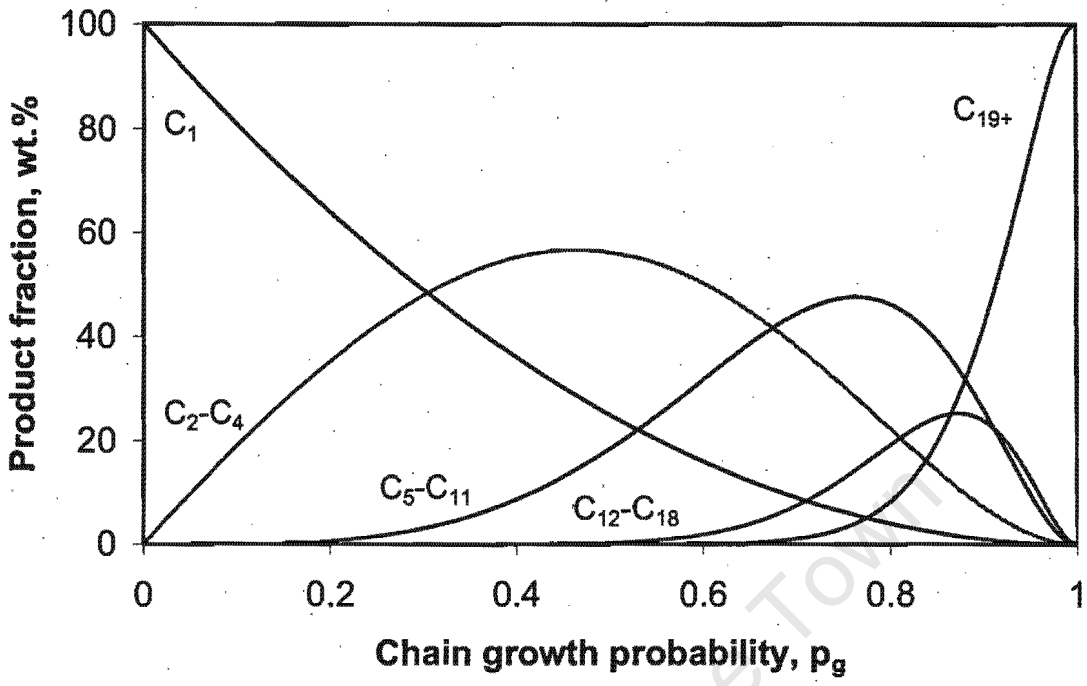

Figure 2.5: Theoretical product distribution as a function of the chain growth probability assuming ideal ASF kinetics

- Relatively high molar methane content; additional sites responsible for solely methane production have been proposed to explain this (Schulz et al., 1995).
- A lower than expected C_2 selectivity.
- A chain length dependent chain growth probability, leading to a curved ASF distribution and higher than expected selectivity of heavy products.

The latter two observations have been attributed to re-insertion of reactive product α-olefins into the chain growth mechanism (see Figure 2.6). α-olefins are believed to be the main primary products of Fischer-Tropsch synthesis with concentration of 70-90 mol% in the corresponding carbon number fractions (Schulz and Claeys, 1999). Their increasing solubility with increasing carbon number (Schulz et al., 1990; Schulz and Claeys, 1999) or their decreasing diffusivity (Iglesia et al., 1993) lead to a carbon number dependent increase of their residence time and therefore an increased

chance for readsorption. The readsorbed species formed is indistinguishable from an alkyl species formed via chain growth and it can initiate further chain growth, which due to the carbon number dependency of the readsorption event, would account for the observed curvature in the ASF distribution. The relatively low amounts of C_2 in Fischer-Tropsch distributions is believed to be due to the much higher reactivity of ethylene compared with the other α-olefins (Schulz, 1999).

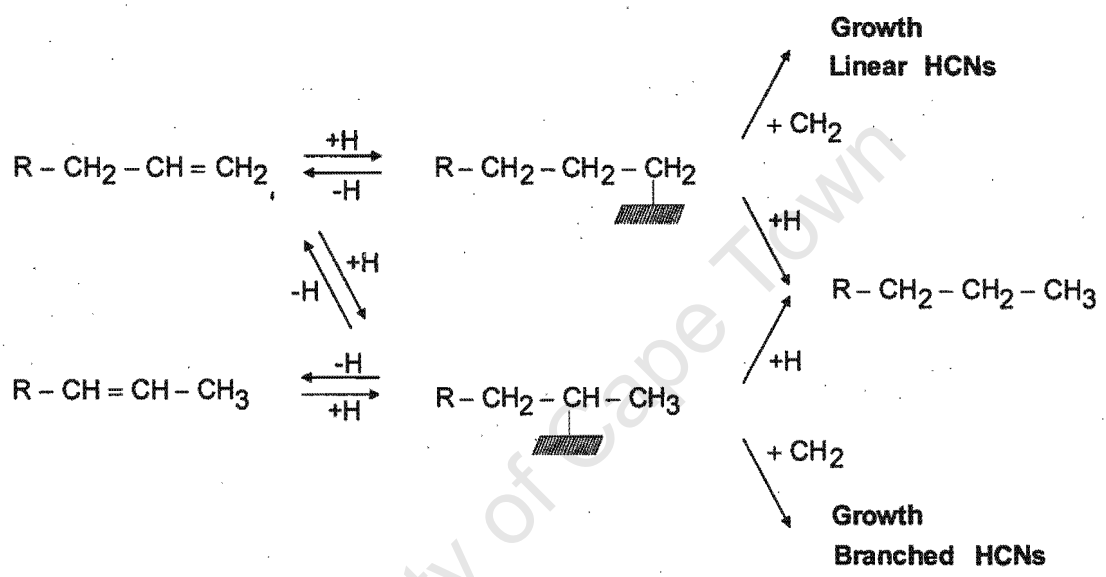

Figure 2.6: Kinetic scheme of the main secondary reactions in FT synthesis (adapted from Schulz and Claeys (1999))

Furthermore, readsorption of n-olefins can lead to their hydrogenation to form the corresponding paraffin of the same carbon number, or it can result in isomerisation via double bond shift to form less valuable olefins with internal double bonds (see Figure 2.6). These secondary reactions would not result in a carbon number alteration of the product distribution. The intermediate of the formation of olefins with internal double bond, an alkyl species attached to the metal surface with a penultimate carbon atom can, after chain growth, also result in the formation of methyl-branched species (see also Figure 2.3). This step is however believed to be severely sterically hindered and suppressed (Schulz and Claeys, 1999). It should be

noted that secondary reactions in particular that of isomerisation can also occur on catalytic centres other than those of Fischer-Tropsch chain growth, e.g. on the catalyst support.

2.3.2 Factors affecting product selectivity

The distribution of the products and their composition depends on the process operating conditions; temperature, pressure, $H_2 : CO$ ratio, residence time, and the properties of the catalyst used. The effect of process conditions on product selectivity is listed in Table 2.1 (adapted from Claeys (1997)).

Table 2.1: Effect of process conditions on product selectivity (adapted from Claeys (1997))

	Temperature	Pressure	H_2:CO	Residence time	K[a]
Methane selectivity	+	-	+	+	-
Chain growth	-	+	-	~	+
Chain branching	+	-	~	~	-
Olefin selectivity	~	~	-	-	+
Oxygenate selectivity	-	+	-	-	+
Carbon deposition	+	~	-	~	+

+ increase with increasing parameter
- decrease with increasing parameter
~ no clear effect

[a]Potassium loading of iron catalysts

Methane selectivity and chain growth are generally affected oppositely. The formation of long chain linear products is favoured at low temperature where chain growth probabilities exceeding 0.9 can be achieved. Low temperature Fischer-Tropsch processes (220-250 °C) mainly aim at production of high molecular weight products such as diesel and wax. The latter can be cracked selectively to increase diesel yields up to 80 wt% (Eilers et al., 1990; Sie et al., 1991). Both iron and cobalt based catalysts are being used in low temperature processes which employ multi-tubular reactors;

slurry beds have also been developed (Espinoza et al., 1999; Steynberg et al., 2004).

Chain growth probabilities in the iron-catalysed high temperature process (330-350 °C) are generally below 0.7 and the process is designed to produce gasoline and light olefins (Steynberg et al., 1999). Fluidised bed reactors are used in this process (Steynberg et al., 1999). Commercial processes are conducted at elevated pressures: 25-40 bar in LTFT and 25 bar in HTFT. Increasing of total pressure generally leads to higher chain growth probabilities.

The H_2:CO ratio has a pronounced effect on chain length and the composition of the products; high ratios leading to a lighter product which can be explained by enhanced product desorption with respect to chain growth in the kinetic Fischer-Tropsch mechanism. At hydrogen rich conditions, low olefin and oxygenates contents are found, which - to a large extent - is due to increased secondary conversion of these valuable products facilitated by hydrogen. Residence time has a similar effect. Table 2.1 also lists the effect of potassium, a crucial promoter in iron based Fischer-Tropsch synthesis. Potassium, which is added in small quantities of less than 5 wt%, dramatically increases chain growth and improves selectivity towards chemicals, mainly via forcing back their secondary reactions (Schulz and Claeys, 1999). It does however also enhance carbon deposition which can lead to catalyst deactivation. Possible effects of metal crystallite size in a Fischer-Tropsch catalyst on product selectivity are described in section 2.6.

2.4 Catalysts for Fischer-Tropsch synthesis

Metals of the Group VIII can be used as catalysts for the Fischer-Tropsch synthesis since these metals can dissociatively adsorb CO and H_2. The most important metals are iron and cobalt which until now are the only ones used for industrial application (Dry, 1981; Anderson, 1984). Iron catalysts have a higher tolerance for sulphur, are cheaper, and can produce more olefin products and oxygenates compared to cobalt

catalyst (Dry, 1993; Schulz, 1999). The lifetime of the iron catalysts is short and in case of high temperature Fischer-Tropsch synthesis is limited to eight weeks time on stream (Dry, 1981). The cobalt based catalysts are in general more active than iron and have a longer life, usually over five years time on stream (Schulz, 1999). Cobalt is well suited for use in Fischer-Tropsch processes with hydrogen-rich synthesis gas with H_2:CO ratios of around 2, as obtained from reforming of natural gas, whereas iron catalysts, which are usually potassium promoted, also catalyse the water gas shift reaction, so that synthesis gas with lower H_2:CO ratios, as obtained from coal gasification, can be used.

Nickel and ruthenium based catalysts are also capable of producing higher molecular hydrocarbons (Vannice, 1977; Dry, 1993). However, the major disadvantage of nickel is that at industrial conditions, it produces mainly methane. Ruthenium catalysts are the most active Fischer-Tropsch catalysts and can produce a high molecular weight wax at reaction temperatures as low as 150 °C. Additionally no promoters are required to stabilize its activity (Schulz, 2003). However, the high price and availability of ruthenium excludes it from being used at an industrial scale thereby limiting its application to academic studies. Most catalysts of practical importance possess large specific surface areas, which can be achieved with small crystallites in the nanosize range. Besides the active catalytic agent Fischer-Tropsch catalysts often contain supports and promoters.

2.4.1 Chemical promoters

Potassium has long been used as a chemical promoter for iron catalysts to effect a change in catalyst activity and product selectivity (Anderson et al., 1952; Dry and Oosthuizen, 1968; McVicker and Vannice, 1980; Amelse et al., 1981; Dry, 1981; Arakawa and Bell, 1983; Donnelly and Satterfield, 1989; Bukur et al., 1990; Raje et al., 1998; Luo and Davis, 2003). Potassium enhances the CO binding strength, facilitates CO dissociation while lowering the strength of metal-hydrogen and metal-

oxygen bonds, thus resulting in an increase of all CO-consuming reactions including Fischer-Tropsch, CO conversion via water gas shift and formation of carbides and free surface carbon (Kölbel and Ralek, 1980; Dry, 1981). Low degrees of potassium promotion therefore lead to an increase of Fischer-Tropsch and water gas shift activity, while at very high loading excessive carbon deposition can lead to the opposite effect. Potassium further compensates acidity introduced by some structural promoters (e.g. Al_2O_3). In doing so it forces back undesired secondary reactions such as olefin isomerisation and largely improved olefin selectivity can be achieved with such catalysts (Claeys, 1997). Consequently, all commercially used iron catalysts are potassium promoted. In contrast to this, potassium promotion of cobalt catalysts leads to decrease in activity (Kazansky et al., 1988; Liu, 1992; Blekkan et al., 1993), however, effects on selectivity similar to those on iron catalysts are observed.

2.4.2 Reduction promoters

The oxidic catalyst precursors are generally exposed to reductive pretreatment in hydrogen, carbon monoxide or mixtures thereof in order to generate the active metallic or carbidic form of the catalyst. Generally, catalysts with high degrees of reduction are more active. However, such reduction degrees can often only be achieved at very high temperature, where sintering processes (increase of crystallite size) become dominant which leads to a loss of active metal surface area or dispersion respectively. The addition of a reduction promoter facilitates the reduction process most likely due to a hydrogen spill-over process from the reduction promoter to the metal oxide (Haggin, 1991). Copper is often used in iron based Fischer-Tropsch catalysts and noble metals such as Pt, Pd or Ru are often used in cobalt Fischer-Tropsch catalysts. It is generally believed that reduction promoters do not impact on the selectivity of the Fischer-Tropsch reaction.

2.4.3 Structural promoters/supports

Structural promoters are sometimes also referred to as supports. Supports are microporous metal oxides which usually possess a high surface area, high thermal and chemical stability and high mechanical strength. The support acts as a dispersing agent of the active metal crystallites (see Figure 2.7) and its major function is to suppress sintering of the active metal.

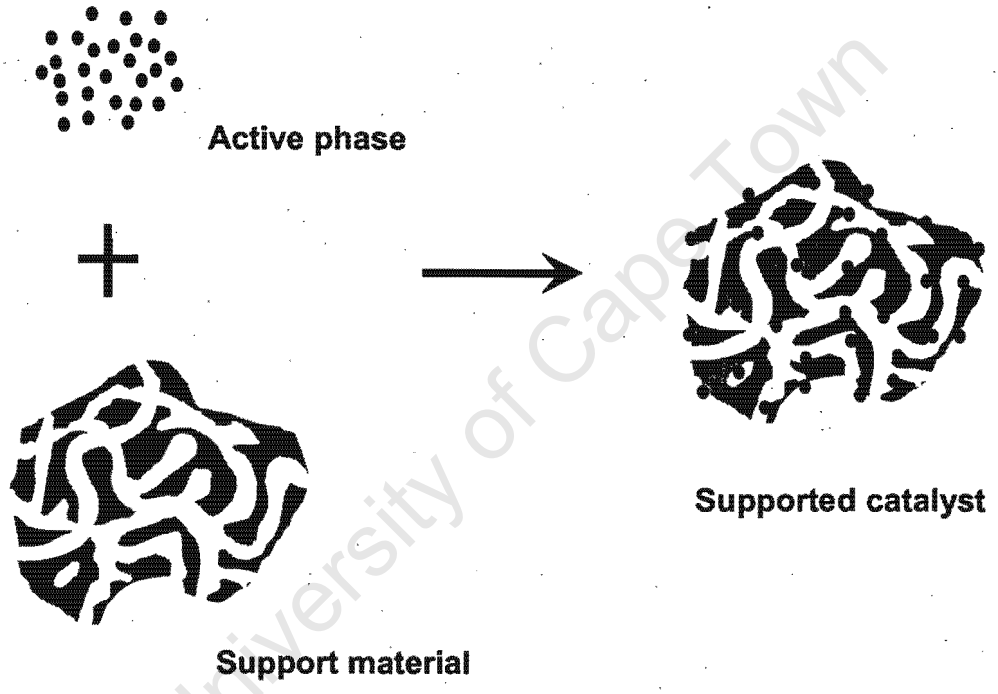

Figure 2.7: Dispersed active phase on support material

Often interactions between active metal and support material occur, which hamper the reducibility of the catalyst precursor (Tauster et al., 1978; Ioannides and Verikios, 1993). All commercial cobalt catalysts are supported in order to ensure maximum utilisation of the expensive active metal. In commercial iron based catalysts only the low temperature catalyst contains small quantities of structural promoters, whereas the high temperature iron catalyst, a fused catalyst, is virtually free of support material (Dry, 1981; Anderson, 1984; Dry, 2004b). Supporting iron

catalysts, in particular those to be used in HTFT, might result in higher catalyst activity and improved catalyst stability or lifetime respectively (Dry, 1981; Bukur et al., 1990; Bartholomew, 2001).

2.5 Catalyst deactivation

Recently several authors have reviewed possible causes of catalyst deactivation (Forzatti and Lietti, 1999; Bartholomew, 2001; Moulijn et al., 2001). During Fischer-Tropsch synthesis, catalysts may loose their activity due to poisoning by contaminants such as sulphur in the feed (Bartholomew, 1987; Rostrup-Nielsen, 1991; Bromfield and Coville, 1999). Catalyst surface and pores may be fouled by carbon produced by cracking reactions of hydrocarbon reactants or products (Rostrup-Nielsen and Trimm, 1977; Trimm, 1983; Bartholomew, 1987; Menon, 1990; Rostrup-Nielsen, 1991; Bartholomew, 2001). At high temperatures, thermal degradation may occur in the form of active phase crystallite growth, sintering (Wanke and Flynn, 1975; Ruckenstein and Dadyburjor, 1983; Bartholomew, 2001). The presence of reactive gases such as CO_2 and H_2O may cause a change in the oxidation state of the catalytically active phase (Dry, 1981; Jager and Espinoza, 1995; Dry, 2004b). Therefore catalyst deactivation can be thought to be a result of a number of unwanted chemical and physical changes. Accordingly, the causes of deactivation are classically divided into three basic categories: chemical, mechanical and thermal in which basic mechanisms such as poisoning, fouling, sintering and vapour-solid reactions are involved. Table 2.2 briefly summarizes the selected mechanisms.

2.5.1 Poisoning

Catalyst poisoning involves a strong irreversible adsorption of either reactants, products or impurities on the catalytic site thereby physically blocking the adsorption

Table 2.2: Types and mechanisms of catalyst deactivation (Bartholomew, 2001)

Type	Mechanism	Description
Chemical	Poisoning	Strong chemisorption of species on catalytic sites, thereby blocking sites for catalytic reactions
	Gas-solid reactions	Reaction of fluid with catalytic phase to produce inactive phase
Mechanical	Fouling	Physical deposition of species from fluid phase onto the catalytic surface and in catalyst pores
Thermal	Sintering	Thermally induced loss of catalytic surface area

site and thus rendering the site inactive. These species once adsorbed onto the site may also induce changes in the electronic or geometric structure of the surface, that is, poison-induced reconstruction of the catalytic surface (Forzatti and Lietti, 1999; Bartholomew, 2001). The most common poisons for Fischer-Tropsch catalysts are H_2S, COS, arsenic, NH_3 and metal carbonyls (Bartholomew, 2001). Sulphur poisoning of commercial iron catalysts is one of the most serious deactivation problems in Fischer-Tropsch synthesis. This problem is most commonly encountered with coal derived synthesis gas. A few parts per billion of sulphur containing compounds can drastically reduce catalyst activity and the catalyst life (Shultz et al., 1962; Bartholomew et al., 1979; Dry, 1981; Bromfield and Coville, 1999; Bartholomew, 2001). Therefore, sufficient sulphur removal from the synthesis gas is of utmost importance, in particular if expensive cobalt based catalysts are used (Schulz, 1999).

2.5.2 Fouling

The effects of fouling by carbon on a supported metal catalyst occur in two noticeable ways, namely; carbon or carbonaceous species may totally encapsulate a metal crystallite and render the crystallite inactive, and micro- and mesopores may be plugged such that access of reactants is denied to crystallites inside these pores (Bartholomew, 2001). Carbon formation on metals can be thought to be structure-

sensitive, that is, sensitive to surface structure and metal crystallite size (Bitter et al., 1999; Bartholomew, 2001). Larger Pt crystallites were found to deactivate more rapidly during CO_2/CH_4 reforming than those containing small crystallites (Bitter et al., 1999). Conversely, higher rates of carbon formation were obtained during methanation on Ni catalysts with smaller metal crystallites (Rostrup-Nielsen, 1974; Bartholomew, 1987).

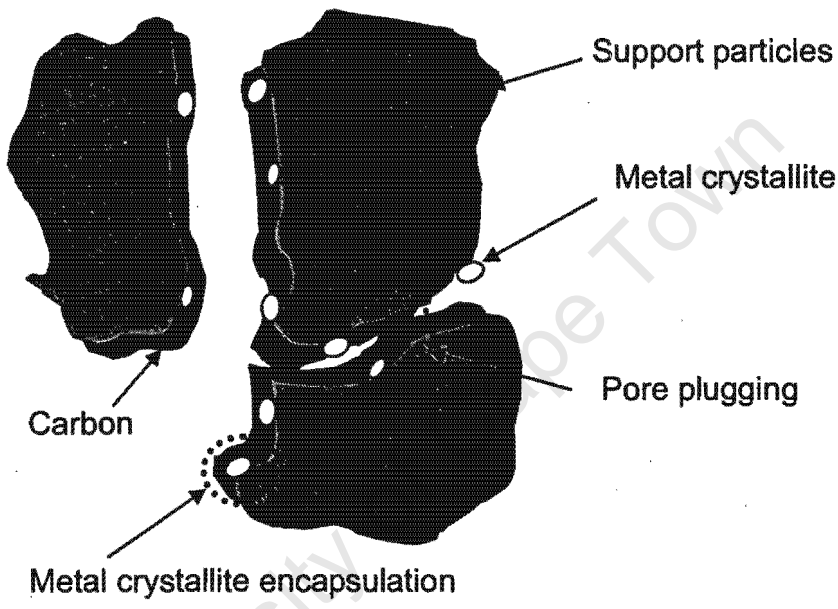

Figure 2.8: Possible effects of fouling by carbon on a supported metal catalyst (taken from Bartholomew (2001))

2.5.3 Sintering

Thermally induced deactivation of catalysts results mainly from loss of effective catalytic surface area due to crystallite growth (sintering) of the catalytically active phase (Wanke and Flynn, 1975; Ruckenstein and Dadyburjor, 1983; Bartholomew, 2001). Sintering is probably the main cause for deactivation of Fischer-Tropsch catalysts. Experimental observations have shown that these catalysts mostly lose their activity at high temperature and sintering is generally accelerated by the presence

of water vapour which is a product of the synthesis (Dry, 1981; Forzatti and Lietti, 1999; Bartholomew, 2001; Moulijn et al., 2001).

The mechanism of sintering is directly related to the melting temperature as defined by the two semi-empirical relations, the so-called Hüttig and Tamman temperatures. When temperature is increased the mobility of atoms increases (Moulijn et al., 2001). Upon reaching the Hüttig temperature, atoms at defects will become mobile (surface recrystallisation). At the Tamman temperature atoms from the bulk will exhibit mobility (bulk recrystallization). At the melting temperature, the mobility will be so high that liquid phase behaviour is observed. The two semi-empirical relations shown in Equations 2.6 and 2.7 are recommended for use and Table 2.3 gives data of $T_{Hüttig}$ and T_{Tamman} for commonly used Fischer-Tropsch metals and support material similar to those in this work.

$$T_{Hüttig} = 0.3T_{melting} \tag{2.6}$$

$$T_{Tamman} = 0.5T_{melting} \tag{2.7}$$

Table 2.3: $T_{Hüttig}$, T_{Tamman}, $T_{melting}$ values of metals relevant for Fischer-Tropsch synthesis (Moulijn et al., 2001) and support materials similar to those used in this work

Compound	$T_{melting}$ K	T_{Tamman} K	$T_{Hüttig}$ K
Ru	2723	1362	817
Fe	1808	904	542
Co	1753	877	526
Ni	1725	863	518
Al_2O_3	2318	1159	695
$C_{graphite}$	[a]3652	1826	1096

[a]sublimes at this temperature

However, for small crystallites the temperature at which mobility occurs may be much lower than that indicated by $T_{Hüttig}$ or T_{Tamman}. Thermostable supports such

as alumina are generally used in supported metal catalysts and small metal clusters are often anchored to them by chemical bonds, so avoiding sintering (Moulijn et al., 2001). Metals also sinter relatively quickly under an oxidizing atmosphere, however the process is slow under reducing and diluted atmospheres (Wanke and Flynn, 1975). In general, sintering processes are difficult to reverse and therefore need to be prevented.

2.5.4 Gas-solid reactions

Dispersed metals, metal oxides, and metal carbides are all typical catalytic phases with surfaces similar in composition to the bulk phases. For a given reaction, one of these catalyst types is generally substantially more active than the others. For example metallic iron and some iron carbides Fe_3C, Fe_5C_2 and Fe_7C_3 are thought to be active for Fischer-Tropsch synthesis while the oxides are thought to be inactive (Dry, 1981; Anderson, 1984; Mansker et al., 1999; Bian et al., 2002; Li et al., 2002). While these chemical modifications are closely related to poisoning, the distinction here is that the loss of activity is due to the formation of a new phase altogether rather than to the presence of an adsorbed species. For example, an iron Fischer-Tropsch catalyst can be transformed from either metallic iron or iron carbides to inactive magnetite, Fe_3O_4, at high carbon monoxide conversions and hence high water partial pressures (Dry, 1981).

Figure 2.9 shows temporal changes of the composition of a high temperature iron catalyst during a Fischer-Tropsch process (Dry, 1981), from initially metallic iron to a mixture of magnetite and iron carbides. Such changes have also been observed by Storch et al. (1951), Mansker et al. (1999), Schulz et al. (1999), Schulz et al. (2002), and Li et al. (2002). There are indications that oxidation of cobalt during Fischer-Tropsch synthesis might be a cause of catalyst deactivation (Iglesia, 1997; Hilmen et al., 1999; Jacobs et al., 2004; van Steen et al., 2005). Iglesia (1997) stated that only small cobalt crystallites (d<5-6 nm) would become inactive due to oxidation

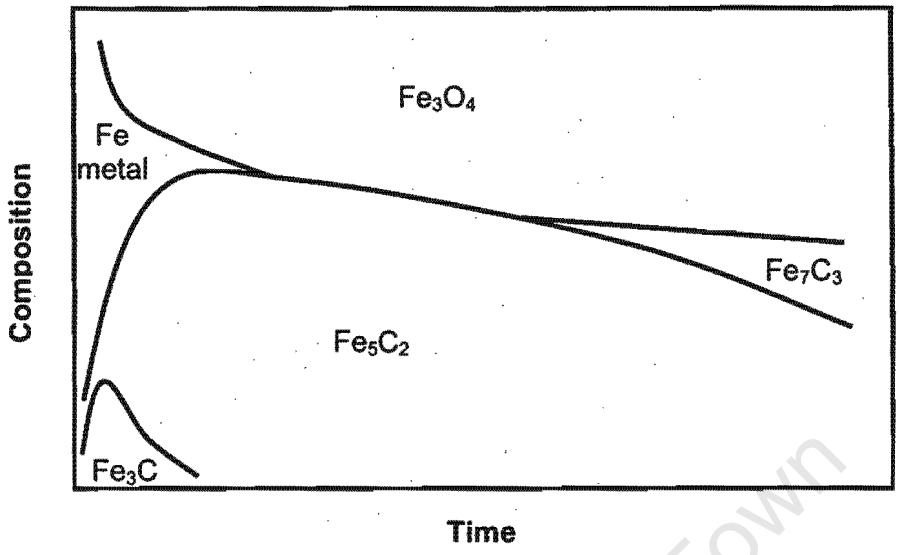

Figure 2.9: The change in the composition of an iron catalyst during high temperature Fischer-Tropsch synthesis (adapted from Dry (1981, 2004b))

of these small crystallites by product water under Fischer-Tropsch conditions. A thermodynamic analysis shows that oxidation of bulk metallic cobalt is not feasible under commercial Fischer-Tropsch conditions (Anderson, 1956). However a detailed thermodynamic analysis done by van Steen et al. (2005) seems to suggest that small cobalt crystallites (less than 4.4 nm) can be oxidised under conditions which do not allow the oxidation of bulk metallic cobalt. This was attributed to the surface energy contribution on the overall energetics of the system. Therefore, thermodynamic analysis of nanosized cobalt crystallites support the possibility that small crystallites can indeed oxidise under Fischer-Tropsch process conditions.

A similar behaviour might be expected for iron-based Fischer-Tropsch catalysts where the active phases are believed to be metallic iron and iron carbides (Mansker et al., 1999; Bian et al., 2002; Li et al., 2002). In the case of iron catalysts it well known that the gases, H_2O and CO_2, can reoxidize metallic iron and iron carbides during synthesis (Dry, 1981; Duvenhage et al., 1994; Jager and Espinoza, 1995; Hilmen et al., 1999) and therefore cause catalyst deactivation. This was demon-

strated by Espinoza et al. (1999); a fixed bed reactor was divided into 3 regions namely top, middle and bottom regions. The top region (inlet) usually experiences a low water partial pressure whereas the bottom region (outlet) is exposed to the highest partial pressure of water. Espinoza et al. (1999) found that, in the top region, the crystallite size remained nearly unchanged while re-oxidation was very low. The middle section of the reactor was found to be a mild catalyst deactivation region. With samples near the bottom of the reactor, the extent of re-oxidation was higher than that for samples from the middle section. The cause for deactivation and therefore loss in activity was attributed to the high water partial pressure.

2.6 Structure sensitivity in Fischer-Tropsch synthesis

Despite extensive research that spans over 80 years, a possible structure sensitivity of Fischer-Tropsch synthesis is still an unresolved question (Boutonnet et al., 1982; Boudart, 1984). Taking the definition of structure as the atomic arrangement at the surface, for structure sensitive reactions one can expect changes in catalyst activity per surface metal atoms exposed and changes in selectivity at crystallite sizes smaller than 5 nm (van Hardeveld and Hartog, 1969). This dependency has been ascribed to a combination of structural and electronic properties, both of which change appreciably with crystallite size in the nanometer range. Some reactions require a specific arrangement of the surface atoms responsible for the promotion of the surface reaction steps involved (Weber et al., 2003; Zaera, 2004). These arrangements or "ensembles" are often referred to as the catalytic active site. For example, ensembles of about 13 nickel atoms were found to be essential for CO dissociation to take place in a methanation reaction (Delmon et al., 1987). Consequently, if crystallites become too small, the chance to have such specific ensembles becomes smaller. As has been modeled by van Hardeveld and Hartog (1969), the presence of

certain configurations depends on crystallite size thus possibly affecting the activity and selectivity properties of catalysts.

The rate of CO dissociation has been suggested to depend on, a crystallite structure, number of high versus low coordinated atoms and density of non-idealities such as cracks (de Koster and van Santen, 1991; Ojeda et al., 2004). However, the overall rate of Fischer-Tropsch synthesis is believed to be determined by steps of product desorption and not CO-dissociation (van Steen and Schulz, 1999). Little is known on possible structure sensitivity or crystallite size effects on the selectivity of Fischer-Tropsch synthesis. A large number of reaction steps occur on the metal surface of a Fischer-Tropsch catalyst, *inter alia* CO and H_2 dissociation, formation of CH_x species, chain growth and product desorption. Schulz et al. (2002) proposed that some reactions would preferentially occur on sites of low coordination ("on top sites"), and others on sites of high coordination ("hole sites") or on plane surfaces, and the selectivity of Fischer-Tropsch synthesis should therefore be considered structure sensitive. High concentrations of sites of low coordination are preferably formed on small crystallites. Indeed, small crystallites showed preferred formation of oxygenates as reported by Barbier et al. (2001) and Ojeda et al. (2004) when CO hydrogenation experiments over cobalt and rhodium based catalysts respectively were conducted. This is possibly an indication of a preferred reaction route (CO insertion) on small crystallites. Effects of crystallite size on activity and selectivity i.e. structure sensitivity, on iron based iron Fischer-Tropsch catalyst have not been reported in literature yet.

Intrinsic crystallite size effects can also result from an enhancement in the relative contribution from the metal-support interaction i.e. as crystallite size decreases the fraction of the total metal atoms in contact with the support increases. Clearly, the structural and electronic details of the surface site are crucial in defining catalytic activity and selectivity.

2.7 Conventional preparation of supported catalysts

Specifically designed catalyst preparation techniques can help to gain new insights and give new impetus in catalyst development of existing syntheses. Furthermore, by varying substrate and catalyst components, the possibility of new reaction pathways with practical application can be studied. Catalyst preparation may be subdivided into chemical synthesis steps, calcination steps and activation steps. Therefore, there is a need to understand preparation chemistry (Delmon et al., 1987). Supported Fischer-Tropsch catalysts are mainly prepared by means of precipitation or impregnation. Less commonly used techniques for catalyst preparation include: ion exchange, synthesis from organometallic compounds and vapour phase deposition in which the metal precursor is loaded onto the support surface (Storch et al., 1951; Dry, 1981; Anderson, 1984).

2.7.1 Impregnation method

Preparation of catalysts by impregnation methods starts with a support in the desired specification, size and shape. The precursor of the catalyst is then impregnated onto the surface of the support by combining the support with a salt solution of the precursor, the amount of liquid often matching the pore volume of the support ("incipient wetness technique"). The catalytically active species is transported to the interior of the support via capillary-type forces or by diffusional effects (Adesina, 1996). The liquid is then removed in a drying or calcination step resulting in oxidic catalyst precursors. These processes may be repeated several times in order to reach a desirable level of active metal concentration on the support. This method is fast and allows the final property and configuration to be controllable in advance (Huang and Schwarz, 1987). It is, however, harder to prepare catalyst with high

loadings and to obtain even dispersion of catalyst components on the surface (Dry, 1981; Anderson, 1984; Adesina, 1996). The impregnation technique is also suited to incorporate promoters in the catalyst, either via simultaneous impregnation with the active metal or in a subsequent impregnation step.

2.7.2 Precipitation method

During catalyst preparation by precipitation, the precursors of active components, often in their salt forms, are first dissolved in water or suitable medium to form a homogeneous solution. The solution is then subjected to pH adjustment to force those metal ions to precipitate. This can be done in the presence of a support material or the support material can be formed via simultaneous precipitation of a corresponding precursor/salt (co-precipitation), the latter method often results in a more homogeneous composition (Dry, 1981; Anderson, 1984). After drying and calcination, oxidic catalyst precursors are obtained. In general, this method yields a catalyst with smaller crystallite sizes than catalyst prepared via impregnation, better dispersion and it also allows incorporation of higher loading of the active components in one step synthesis (Vannice, 1975; Nijs and Jacobs, 1980; Reuel and Bartholomew, 1984b,a).

2.7.3 Remarks

With above methods, it is normally not easy to control the crystallite size and size distribution because a of high degree of agglomeration and poor control of crystallite growth processes (Vannice, 1975; Reuel and Bartholomew, 1984b). Therefore, for the synthesis of monodispersed, well-defined crystallites as needed in the anticipated study, another approach is of utmost importance. A recently developed method: the water-in-oil microemulsion technique, has shown great potential for controlling the size and shape of inorganic nanocrystallites (Boutonnet et al., 1982; de Gennes and

Taupin, 1982; Pillai et al., 1995; Pileni, 2003; Capek, 2004; Eriksson et al., 2004) and this simple technique may evolve as a promising tool for Fischer-Tropsch catalyst fabrication (Bartholomew, 1991; Adesina, 1996).

2.8 The microemulsion technique

The idea of using microemulsion systems for catalyst preparation was first suggested by F. G. Gault (Corolleur et al., 1972; Eriksson et al., 2004) and synthesis of metal nanocrystallites using this technique was first reported by Boutonnet et al. (1982). The crystallite properties such as narrow size distribution in the nanometer range and homogeneous composition, make them excellent catalyst precursors (Boutonnet et al., 1982, 1987). Thus microemulsions can be applied in the preparation of nanocrystallites of a desired size. The microemulsion technique has been used for synthesis of a wide range of materials (Pileni, 1989, 1993; Pillai et al., 1995; Capek, 2004; Eriksson et al., 2004) such as metallic crystallites, metal oxides (Song and Kang, 2000), semiconducting (Song and Kim, 2000) and magnetic materials (Pillai et al., 1995).

CO_2 and CO hydrogenation with catalysts prepared by both microemulsion and impregnation methods have been studied by, among others, Abrevaya and Targos (1987), Kishida et al. (1996) and Hanaoka et al. (2000). The catalysts prepared by microemulsions often showed a higher activity than the impregnation counterpart.

2.8.1 The microemulsion system

Microemulsions are thermodynamically stable, optically isotropic systems consisting of a surfactant and/or a co-surfactant phase, an oil phase, and an aqueous phase. At macroscopic scale, a microemulsion looks like a homogeneous solution but at molecular scale, it appears to be heterogeneous. The structure of a microemulsion,

at a given temperature, is determined by its composition. In the monophasic domain, either on the water rich or the oil rich side of the phase diagram (Figure 2.10), the microemulsions consists of uniform and spherical droplets dispersed in the continuous medium. At high water concentration, the microemulsion consists of small oil droplets in a continuous aqueous phase (oil-in-water microemulsion or normal micelle). With increasing oil concentration, a bicontinuous phase without any clearly defined shape is formed. At high oil concentration, the bicontinuous phase is transformed into small water droplets in a continuous oil phase (water-in-oil micro-emulsion or reverse micelle). A two-phase system exists outside the areas corresponding to microemulsion solutions described above. The presence of water is necessary to form large surfactant aggregates (Pileni, 1993).

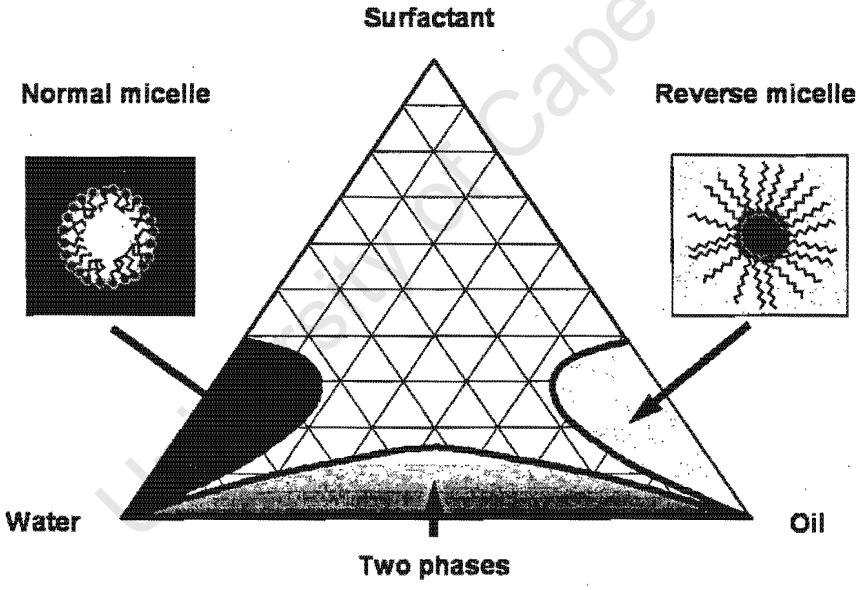

Figure 2.10: Schematic phase diagram of surfactant-oil-water system

The characteristic properties of microemulsions include: spontaneous formation, optically clear appearance, large interfacial area, low interfacial tension and solubilization capacity for both water- and oil-soluble compounds. It should be pointed out that the system is temperature sensitive, particularly in the case of non-ionic surfactants. Increasing the temperature will destroy the oil droplets while the water

droplets will be destroyed by a temperature decrease (Eriksson et al., 2004). Therefore, it is of practical importance in the case of nanocrystallite preparation that microemulsion preparations are done at constant temperature.

2.8.2 Preparation of nanosized crystallites using the water-in-oil microemulsion technique

Water-in-oil microemulsions provide particularly favourable reaction conditions for the preparation of monodispersed crystallites. The water-in-oil microemulsion system is an isotropic dispersion of the aqueous phase in the continuous oil phase (Figure 2.11) (Boutonnet et al., 1982; Stenius et al., 1984). In this technique, synthesis of nanosized crystallites is based on the principle of confining the precipitation or reduction of precursors in the tiny aqueous droplets of this water-in-oil microemulsion (Pileni, 1993). When a soluble metal salt is incorporated in the aqueous phase of the microemulsion, it will reside in the aqueous micro-droplets surrounded by oil. Precipitation can be carried out when droplets containing the metal solution and the precipitating or reducing agent solution collide with each other. Each of these droplets will thus become a nanosized reactor for forming nanosized solid crystallites and the size of the "reactors" will ultimately determine the resulting crystallite size. A decrease in the water to surfactant ratio is expected to yield smaller droplets and thus the resulting metal crystallites after precipitation is expected to become smaller.

The reverse micelle structure provides a reaction template in the appropriate size range, and size control is achieved by regulating the nucleation and growth process (Sjöbolm et al., 1996; Song and Kim, 2000). In fact, it is the dynamics of micellar dispersions that make microemulsions so appropriate for this application. The droplets are subject to Brownian motion and collide continuously, leading to the formation of short-lived dimers (see Figure 2.12) and to the exchange of the aque-

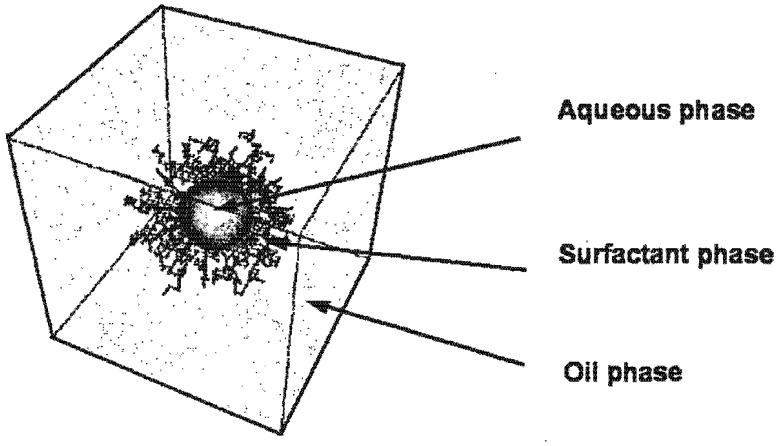

Figure 2.11: Water-in-Oil microemulsion system

ous contents of the micelles (Pillai et al., 1995; Eriksson et al., 2004; Capek, 2004). This dynamic process ensures a homogeneous repartition of the reactants among the aqueous droplets and thus the formation of very monodispersed crystallites (Eastoe et al., 1991). However, the size of the crystallites obtained remains in most cases directly related to the size of the water pool (Pileni, 1989).

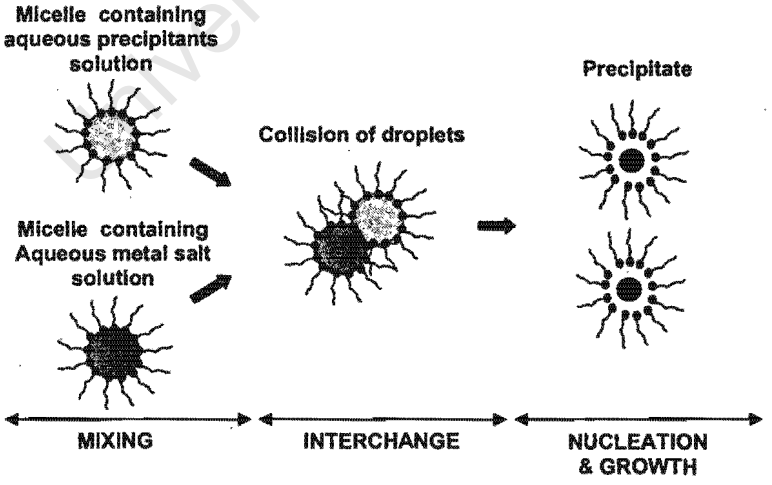

Figure 2.12: A schematic diagram of the proposed mechanism during precipitation using two microemulsion systems (Pileni, 1989; Lopez-Quintela and Rivas, 1993; Eriksson et al., 2004)

Parameters influencing the crystallite size and crystallite size distribution are the reaction time, the chemical nature of the precursors and the constituents of the micelle system and their composition as well as subsequent drying or calcination conditions (Boutonnet et al., 1982; de Gennes and Taupin, 1982; Stenius et al., 1984; Boutonnet et al., 1987; Pileni, 1989, 1993; Pillai et al., 1995; Song and Kang, 2000; Song and Kim, 2000). Many of these process variables have been optimised in previous studies (Boutonnet et al., 1982; Stenius et al., 1984; Boutonnet et al., 1987; Pileni, 1989) to yield high purity nanosized crystallites. Only little research has been done in preparing supported catalysts using the microemulsion technique. One approach is to form the support in situ, via coprecipitation from its precursor material (e.g. Kishida et al. (1996); Hayashi et al. (2002)). Another approach is to add a solid support material during the preparation (Stenius et al., 1984; Abrevaya and Targos, 1987; Abrevaya, 1990; Eriksson et al., 2004)

The reverse micelle technique is a simple technique which does not require any special equipment. Nevertheless, this technique has its own challenges that need to be tackled before its commercialisation. One hurdle is in the recovery and recycling of the liquid phase and the other is to increase the amount of catalyst prepared from a single microemulsion.

2.8.3 Choice of surfactant

Generally, surfactants can be classified according to the types of head groups namely ionic, nonionic and amphoteric (Figure 2.13). The polar head of surfactant will always orientate itself towards the polar phase in the microemulsion, for instance, the water phase in a reverse micelle system. The most commonly used commercial surfactants that have been employed to prepare microemulsion systems are sodium bis(2-ethylhexyl) sulfosuccinate (AOT), sodium dodecyl sulphate (SDS) and cetyl trimethyl ammonium bromide (CTAB). However, most of these surfactants are hazardous chemical substances and can bring negative effect to the catalyst as they may

introduce components such as sodium and sulphur to the resulting catalyst, which may act as catalyst poisons if not removed effectively. As an alternative, nonionic surfactants can be used. Often co-surfactants (such as primary alcohols) are added to modify the rigidity of the micelle core, thus allowing for modification of transport processes through the core (Stenius et al., 1984; Boutonnet et al., 1987; Abrevaya and Targos, 1987; Pileni, 1989).

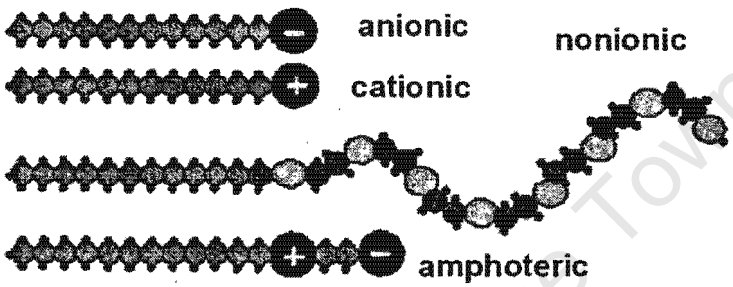

Figure 2.13: Classification of surfactants

Chapter 3

Scope of this work

Fischer-Tropsch synthesis is regarded as a surface polymerisation reaction catalysed by transition metals, in particular Ni, Co, Fe and Ru. These catalytically active metals are present as small crystallites in Fischer-Tropsch catalyst. Control of size of a metal crystallite on a support might be very important in developing a catalyst, which meets the activity, stability and selectivity requirements of a particular catalytic process. Whereas the highest mass specific catalyst activity is to be expected when small metal crystallites are employed, small crystallites of cobalt have been claimed to be inactive due to oxidation. A similar behaviour might be expected for iron-based catalysts where the active phases are believed to be iron and iron carbides. During Fischer-Tropsch synthesis, high H_2O and CO_2 partial pressures may cause the transformation of the active small metallic and/or iron carbide crystallites to the supposedly inactive oxides. The exact crystal size, at which iron would transform under Fischer-Tropsch reaction conditions, is not yet known. Furthermore, the selectivity of Fischer-Tropsch synthesis has been suggested to be structure sensitive, or dependent on crystallite size regardless of possible transformation processes. Consequently, in order to investigate the effect of crystallite size on activity and selectivity in Fischer-Tropsch synthesis, catalysts with known narrow metal crystallite size distributions are required. Traditionally, supported Fischer-Tropsch catalysts

have been prepared via the conventional methods which can result in well-dispersed nanometer sized crystallites but control of size was not achieved. This makes the interpretation of crystallite size dependent behaviour of the catalyst impossible. Thus, the application of the microemulsion technique to prepare a number of supported iron catalysts is proposed. The experimental approach in this work entails: investigation of a suitable microemulsion system, preparation of unsupported iron oxide crystallites and characterisation thereof, preparation of supported catalysts with different crystallite sizes and characterisation thereof and finally Fischer-Tropsch testing of these model catalysts.

Chapter 4

Experimental Methods

4.1 Preparation of water-in-oil microemulsion

Iron oxide crystallites with different sizes were prepared using water-in-oil microemulsions and a precipitation technique. The study was subdivided into firstly characterisation of a suitable water-in-oil microemulsion system, secondly preparation of nanosized oxidic iron crystallites with controlled crystallite size and thirdly preparation of supported catalyst using the same microemulsion systems but selected with regard to their composition. The water-in-oil microemulsion system, water/Berol 050[1] (Akzo Nobel)/n-hexane (HPLC grade, Aldrich Chemical Company), shown on the ternary diagram in Figure 4.1 was used in this work and previously by other researchers Abrevaya and Targos (1987). For this ternary system, stable and optically transparent microemulsions were only obtained in the region depicted. Phase separation or cloudy solution was noticeable outside these limits.

This stability region was obtained by titrating mixtures of Berol 050 and n-hexane with water. The titrated samples were investigated visually. The formation of clear, homogeneous and transparent solution, after stirring the mixture vigorously, was

[1]Berol 050 is a nonionic surfactant, the chemical name being: Pentaethyleneglycoldodecylether

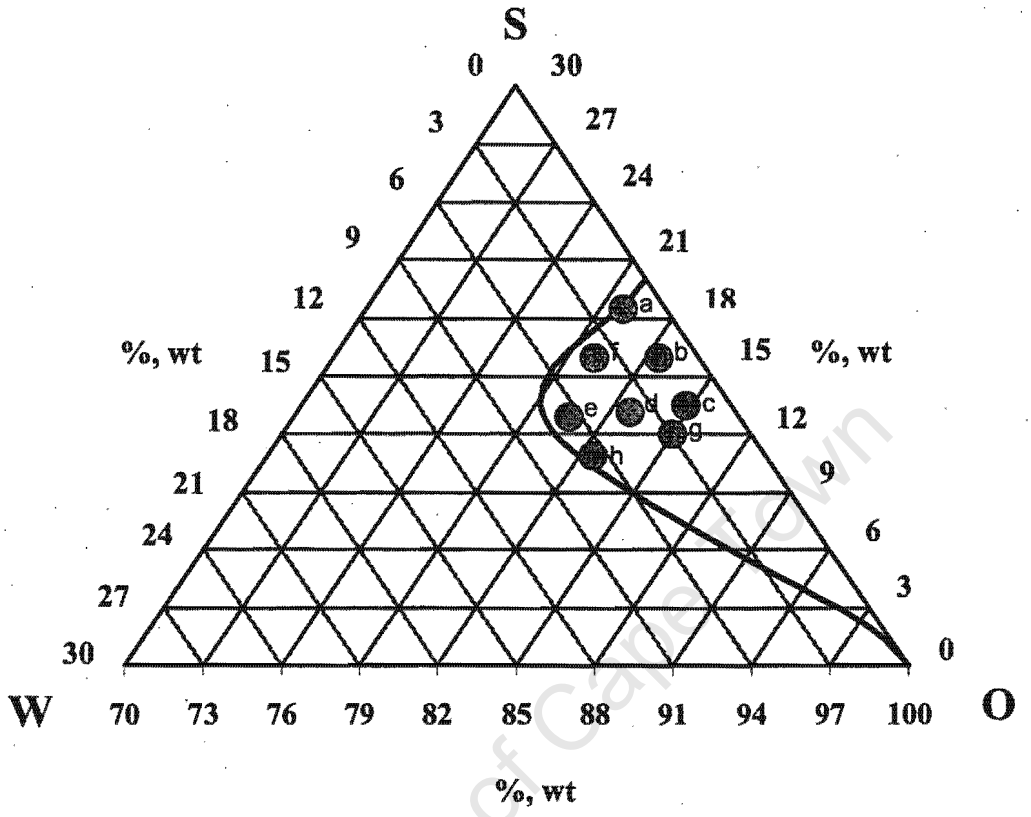

Figure 4.1: Ternary diagram showing the stability region from which microemulsions were prepared (**W**: water, **O**: oil (n-Hexane), **S**: surfactant). Sample codes indicating amounts of water and surfactant in grams, m_{oil} = 250 g: a 5:40, b 5:48, c 5:58, d 12:40, e 20:40, f 13:50, g 9:35, h 20:33

considered as belonging to the microemulsion regime. In contrast, phase separation or a cloudy solution was considered to be outside the stability region. All the titration measurements were carried out at 25 °C in a thermostatic bath. Specifications of the eight experiments conducted for preparation of nanosized crystallites are also shown in Figure 4.1. The sample codes were constructed from the amount of aqueous phase and surfactant phase present by weight, for instance, 5:40 stands for 5 g aqueous phase and 40 g surfactant phase. In all cases the amount of oil phase (n-hexane) was kept constant at 250 g. In experiments a, b and c, the amount of water was kept constant while the amount of surfactant phase was being varied.

In experiments c, d and e, the amount of water present was changed while that of the surfactant phase was kept constant. The other 3 experiments, f, g and h were taken randomly but strategically close to experiments a - d to ascertain the effect of water-to-surfactant ratio.

4.2 Precipitation of Fe^{3+} ions in water-in-oil microemulsions

In this study iron oxide crystallites were prepared in microemulsions via precipitation from iron (III) nitrate solutions using ammonium carbonate as a precipitant. For this, microemulsions were prepared in duplicate by firstly mixing specific volumes of Berol 050 with n-hexane. After equilibration for 24 hours at room temperature, a white residue that formed was filtered off. Thereafter, appropriate volumes of an aqueous solution of ferric nitrate ($Fe(NO_3)_3.9H_2O$, 99%, Sigma-Aldrich Inc.) and an aqueous solution of ammonium carbonate ($(NH_4)_2CO_3$, 30-33% as NH_3, Fluka) were added to each of the duplicate microemulsions respectively. The total amount of oil phase and the salt concentrations were kept constant throughout all experiments conducted. A 4:1 molar ratio of $[(NH_4)_2CO_3]$:$[Fe^{3+}]$ was used to ensure the complete precipitation of the 0.5 M iron nitrate solution.

The two combined microemulsions were then mixed in a 2 *l* glass beaker using an overhead stirrer under constant stirring speed of 800 rpm for 3 hours (Figure 4.2). Due to collision and coalescence of the droplets, the reactants come in contact with each other, react and form precipitate. The precipitate remains confined to the interior of the microemulsion droplets until they were separated from the liquid phase by flocculating with acetone and thereafter washed with acetone several times to remove the surfactant. This was followed by drying at room temperature (for 3 hours), then at 120 °C for 24 hours and finally calcination at 300 °C for 3 hours in a fixed bed reactor under flowing air (flowrate: 60 ml(NTP)/min/g; heating rate:

10 °C/min). The success of these preparation attempts was mainly monitored using Transmission Electron Microscopy for determining size distribution and shape of the crystallites. During calcination the iron present in the form of hydroxides or oxyhydroxides is transformed into iron oxides.

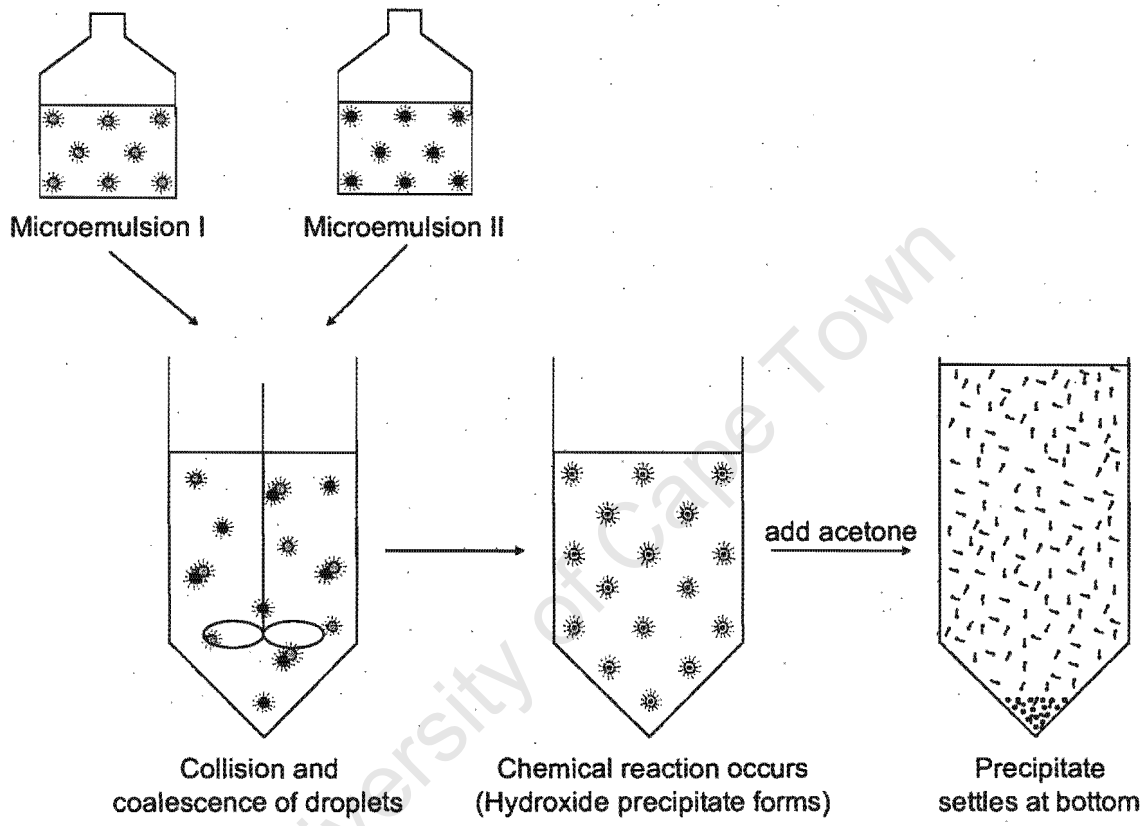

Figure 4.2: Schematic representation of synthesis of iron nanocrystallites via precipitation in microemulsion using two microemulsions

4.3 Characterisation of water-in-oil microemulsions

An estimation of the sizes of reverse micelles consisting of water/Berol 050/n-hexane and crystallites formed therein were conducted based on viscosity and UV absorbance of the microemulsion solution. These techniques have been used by Hanaoka et al. (2001); Ingelsten et al. (2001); Kinugasa et al. (2002); Caponetti

et al. (2003); Khiew et al. (2003); Hota et al. (2004) to characterise a number of different microemulsion systems.

Viscosity measurements were done on all eight microemulsions using a Brookfield DV-1+ viscometer connected to a S00 spindle at 25 °C under constant stirring speed of 100 rpm for 5 minutes. This technique was also used to characterise the microemulsions after a precipitation had been conducted in order to ascertain any size changes of micelles.

UV-Vis absorption spectra of just-prepared iron nanocrystallites, via precipitation in microemulsion system, were recorded on a Biochrom Ultrospec 2100 *pro* spectrophotometer in the wavelength range 350-600 nm using a 10 mm quartz cell. Microemulsions containing only n-hexane, surfactant and water were used as reference samples and absorption data for the other samples were corrected accordingly.

4.4 Catalyst preparation

Two series of supported catalysts of varying metal crystallite sizes were prepared by the water-in-oil microemulsion technique using an activated carbon support (Riedel-de Haën; BET surface area: 1244 m^2/g; BET average pore diameter: 20 Å) and γ-alumina (Puralox SCCa 5-150, Sasol, Germany; BET surface area: 162 m^2/g; BET average pore diameter: 115 Å). Results of BET characterisation of these supports are shown in Appendix B. Preparation of the active catalyst precursor was accomplished by mixing of two microemulsions as described above. The only additional step is the addition of the support (carbon or alumina) to the microemulsion before the precipitate was separated from the liquid phase by flocculating with acetone. An iron loading of 10 wt% was anticipated. Thereafter, the sample was slowly dried in a rotar vapour at 40 °C and 400 mbar for 1 hour, then 250 mbar until the sample appeared dry. The catalyst precursors were then loaded with potassium via incipient wetness impregnation with an aqueous solution of potassium nitrate (KNO_3, 99%,

univAR, Saarchem). It was aimed at a potassium loading of 5 g K per 100 g Fe, a typical level of potassium loading in Fischer-Tropsch catalysts (Dry, 1981, 2004b). The slurry was again allowed to slowly dry in a rotar vapour at 75 °C and 250 mbar for 30 min, then at 200 mbar for 1 hour, 150 mbar for another 1 hour and then 75 mbar until dryness. Subsequently, the sample was calcined under flowing argon, 60 ml(NTP)/min/g, in a fluidized reactor at 350 °C for 16 hours (heating rate: 10 °C/min). Here, argon was used instead of air to prevent combustion of activated carbon.

4.5 Charaterisation of nanocrystallites and catalysts

4.5.1 Transmission Electron Microscopy, TEM

The size and shape of the dried unsupported samples was determined using a JEM200CX (JEOL, JAPAN) Transmission Electron Microscope (TEM) operated at 200 kV. Iron oxide powder samples were ultrasonically suspended in methanol and a drop of each sample was transferred onto a carbon coated copper grid. The copper grid is then covered with formvar[2], support film for TEM grids, to prevent crystallites from falling off the copper grid and contamination of the condenser. The samples were allowed to dry in air at room temperature before analysis.

Supported samples were analysed using a LEO 912 (Leo, now Zeiss, GERMANY) Transmission Electron Microscope operating at 120 kV. The samples were placed in a small plastic vial which was then filled with liquid resin. This was left to solidify in an oven at 60 °C for 48 hrs. Thereafter, the samples were cut into very thin slices, 60 nm thick using an Ultramicrotome LEICA UltracutS (Leica,

[2]otherwise known as polyvinyl formal

AUSTRIA) cutting machine. The samples were transfered onto copper grids for viewing under the microscope. Measurements of crystallite size were done manually on TEM micrographs using an image analysis tool called ImageJ[3].

The mean volume diameter of a crystallite distribution, $\bar{d}_{c,v-TEM}$ was calculated using Equation 4.1 for comparison with results from other techniques such as XRD which are sensitive to the volume of crystallites (Bergeret and Gallezot, 1997).

$$\bar{d}_{c,v-TEM} = \frac{\sum n_i d_{c,l-TEM}^4}{\sum n_i d_{c,l-TEM}^3} \tag{4.1}$$

with $d_{c,l-TEM}$ the number or length based crystallite diameter as directly obtained from TEM micrographs. To obtain statistically relevant information of crystallite size distribution, and average crystallite size, a minimum of $n = 200$ crystallites was measured per sample.

4.5.2 Scanning Electron Microscopy and Energy Dispersive X-Ray analysis, EDX

A scanning electron microscope (LEO S444 SEM, La:Ka, UK) equipped with a Four Quadrant Back Scatter Detector and an energy dispersive Fissons Kevex X-ray spectrometer (EDXA) with sigma analysis software was used to investigate the macroscopic distribution of iron oxide crystallites on the support and to determine the actual amount of iron on the catalyst. For quantification of the latter, samples of known iron concentration were used as standards.

Sample preparation involved sprinkling dry powder of the sample on an aluminium stub coated with glue containing graphite. Here, graphite is used to conduct electrons thereby preventing charge build up. The samples were then coated with carbon which does not interfere with the elemental analysis.

[3]A public domain Java image processing program inspired by National Institute of Mental Health

4.5.3 Brunauer-Emmett-Teller method, BET

The specific surface areas and pore size distributions of the structural supports, alumina and activated carbon, were determined via N_2 adsorption/desorption according to the BET method (see Appendix B) using a Micromeritrics ASAP 2000 analyzer (Micromeritrics Instruments Corp., USA). BET surface area analysis was also applied on the unsupported oxidic crystallite samples for estimation of the average crystallite size assuming spherical geometry and that the crystallites were present as Fe_2O_3 after calcination of the precipitate in air (see also section 4.2).

$$\overline{d}_{c-BET} = \frac{6}{\rho_{Fe_2O_3}.S_g} \tag{4.2}$$

$\overline{d}_{c-BET}$ is the average crystallite diameter, S_g is the surface area per gram of iron oxide present during BET analysis and $\rho_{Fe_2O_3}$ is the density of Fe_2O_3 (5.25 g/cm^3). This size, $\overline{d}_{c-BET}$, is equivalent to the volume-weighted average.

4.5.4 X-Ray Diffraction spectroscopy, XRD

Analyses of crystalline phases in crystallite and catalyst samples as well as average crystallite sizes were determined by means of X-ray analysis. X-ray diffraction measurements were done on a Phillips X-ray diffractometer with Cu-Kα radiation of wavelength 1.540 Å at 40 kV and 25 mA. The scan range was $5° < 2\theta < 75°$. All diffraction patterns were recorded in the step-scan mode with a step size of 0.05 degrees and a scan rate of 0.5 deg/min. Diffraction peaks of crystalline phases were compared with those of standard compounds reported in the JCPDS[4] data file. The average crystallite sizes, $\overline{d}_{c-XRD}$ were calculated from the peak width at half-height

[4] Joint Committee for Powder Diffraction Standards

using the Debye-Scherrer equation:

$$\overline{d}_{c-XRD} = \frac{k\lambda}{\beta cos\theta} \tag{4.3}$$

λ is the X-ray wavelength, k is the shape factor (k = 0.9), θ is the diffraction angle in degree and β is the line broadening of FWHM[5] in radian. It important to note that the size $\overline{d}_{c-XRD}$ obtained at this particular β has no clear physical meaning (Bergeret and Gallezot, 1997). However, in this work it will be considered as a volume-weighted average size.

4.5.5 Temperature-Programmed Reduction, TPR

The reduction behaviour of unsupported and supported samples was investigated by means of temperature programmed hydrogen reduction. Temperature programmed reduction was carried out in a U-type quartz reactor on a Micromeritics AutoChem2910 (Micromeritics Instrument Corp., USA). Typically, iron oxide powders (≈30 mg) and supported catalysts (≈120 mg) were treated under a 5.6% H_2/Ar gas flow at a flow rate of 50 ml(NTP)/min, from 30 to 1000 °C with a constant heating rate of 10 °C/min. For supported catalysts, before each TPR run, the samples were dried again with argon at 300 °C for 16 hrs (heating rate: 10 °C/min). This was done in order to simulate the pre-treatment conditions applied in Fischer-Tropsch reaction work. These experiments were done to check the reduction behaviour of the samples.

The instrument was also used to determine the degree of reduction of a catalyst as present after hydrogen pretreatment prior a Fischer-Tropsch experiment. For this the catalyst samples were exposed to *in situ* Fischer-Tropsch synthesis pre-treatment conditions i.e., heating to 350 °C for 16 hrs under flowing pure hydrogen (heating rate: 1 °C/min) and thereafter reduction in 5.6% H_2/Ar gas flow ramping

[5]Full Width at Half Maximum intensity

from room temperature up to 1000 °C. From the hydrogen consumption of the reduction of the pre-reduced samples and the known amount of Fe_2O_3 present in a sample degrees of reduction could be determined. The consumption of H_2 was measured using a thermal conductivity detector which was calibrated at regular intervals using samples with known reduction behaviour (e.g. Ag_2O, NiO). The samples were heated with a regulated furnace and the temperature was measured by a thermocouple placed 2 mm above the sample.

4.6 Fischer-Tropsch synthesis experiments

4.6.1 Experimental setup

The physical setup of the equipment for Fischer-Tropsch synthesis experiments is shown schematically in Figure 4.3. It consists of a U-tube micro fixed bed reactor, E-5. Gases are supplied from cylinders (Air Products, H_2 5.0, CO 3.7, Ar 5.0, N_2 5.0) and fed via mass flow controllers (Brooks 5850S, Brooks Instruments, The Netherlands). During operation, the synthesis gas is fed to the system via mass flow controllers F-1 and F-2, a 4-way-valve, 4WV is used to change from flow from bypass to the reactor. A pressure controlled argon stream was fed after the reactor to maintain and control the total pressure in the system. A N_2/cyclohexane mixture (0.15 % cyclohexane in N_2), used as an internal standard for sample analysis, was fed to the system via mass flow controller F-3 directly to the product line at atmospheric pressure just before the product ampoule sampler, E-7 (see also section 4.6.4). Liquid products in Fischer-Tropsch experiments, if formed, are collected in a wax trap, E-6, which can be bypassed if no formation of liquid products are expected. The temperature of the wax trap is normally set 10 °C below the temperature at which the Fischer-Tropsch experiment is conducted, in order to ensure efficient wax collection. The temperature of all other lines after the reactor are kept

at temperatures 10 °C higher than the reaction temperature.

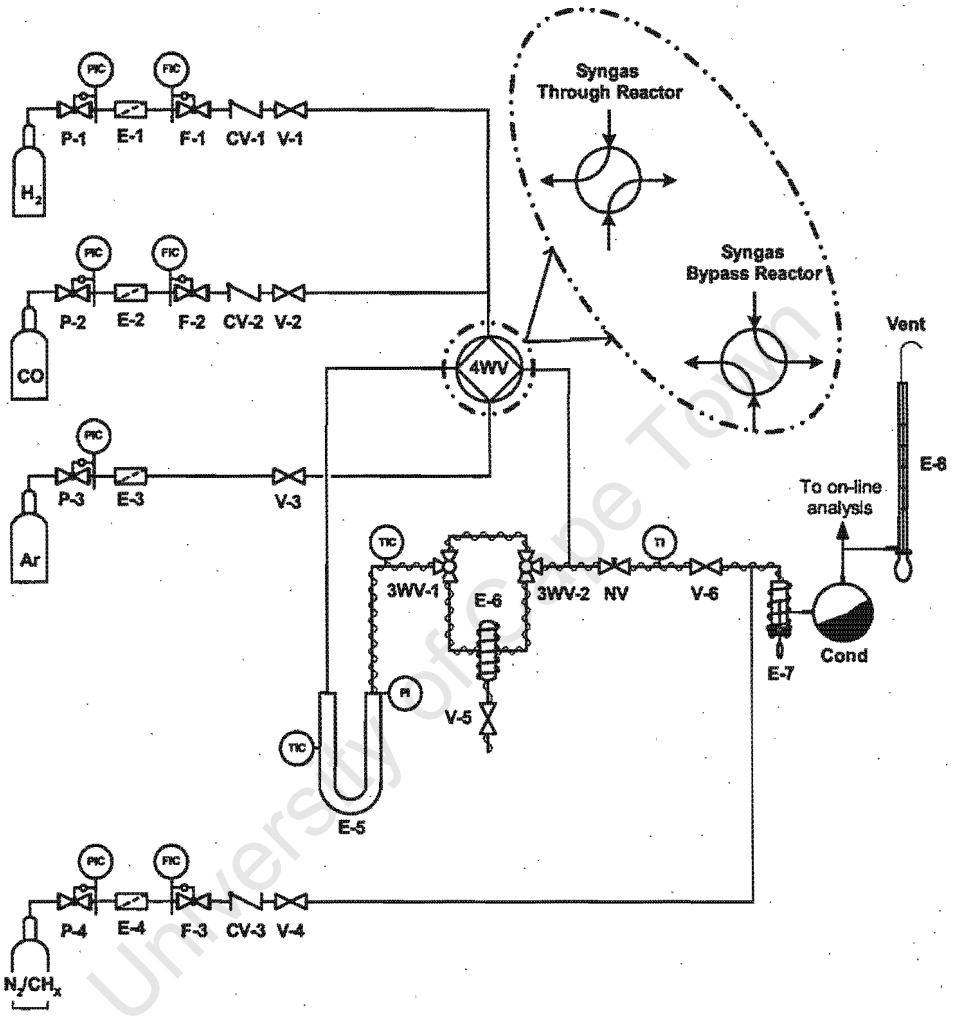

Figure 4.3: Experimental setup for Fischer-Tropsch synthesis. P-1 - 4: Pressure regulators; E-1 - 4: Line filters; E-5: Reactor; E-6: Wax trap; E-7: Ampoule sampler; E-8: Bubble flowmeter; Cond: Condenser; CV-1 - 3: Check valves; V-1 - 6: One way valves; 3WV-1 - 2: Three way valves; 4WV: Four way valve; NV: Needle valve; PIC: Pressure indicator and control; TIC: Temperature indicator and control; FIC: Flow indicator and control; PI: Pressure indicator; TI: Temperature indicator

4.6.2 Reactor and catalyst packing

The reactor used was a U-tube fixed bed reactor made from stainless steel (O.D. 1/4", I.D. 3 mm). The catalyst diluted with silicon carbide (Aldrich) was packed inside the reactor and both ends were tightly plugged with glass wool so as to prevent the catalyst bed from moving during an experiment and during pressurizing and pressure releasing of the system. The reactor was then placed in a temperature controlled electric furnace comprising an aluminium block housing. A thermocouple was placed in an axial thermowell outside the reactor centrally between the limbs of the U-tube (and in contact with the reactor wall) for the purpose of monitoring and controlling temperature.

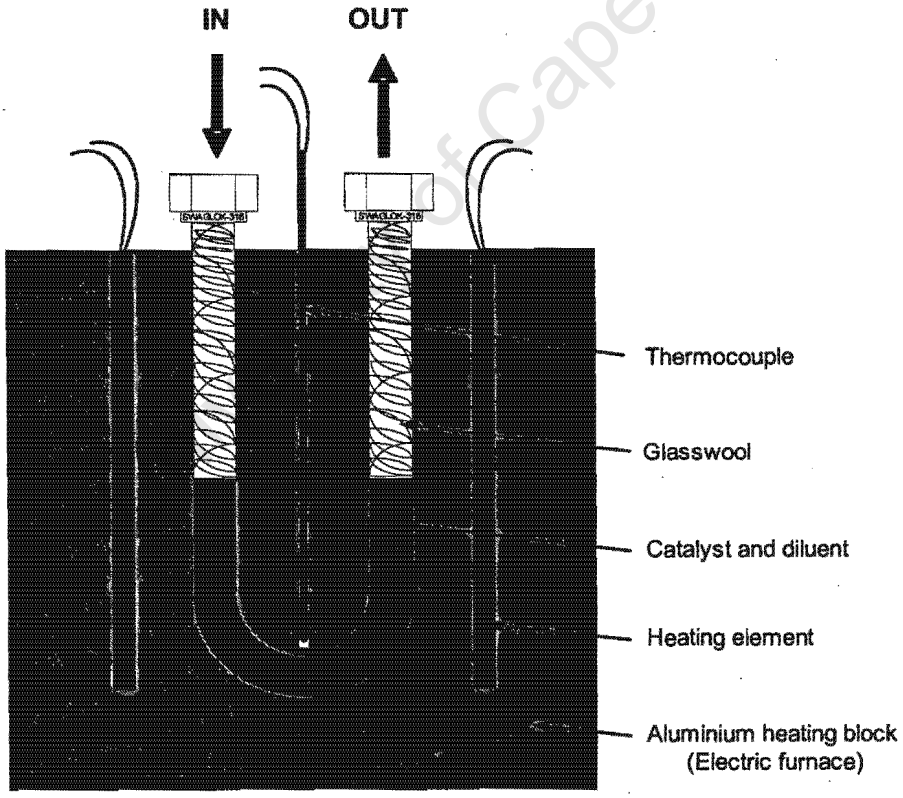

Figure 4.4: Configuration of the U-tube reactor

Prior to the conduction of FTS experiments, the temperature profile of the packed

bed was determined under typical reaction conditions of temperature and flow rate. For these experiments an external thermocouple was positioned at different points in the full length of the packed bed so as to determine a complete bed temperature profile. The axial temperature profile was measured and found to be within +/-0.1 °C of the average bed temperature over a bed length of ca. 10 cm. This became the length from which the total volume of the catalyst and diluent required to fill the isothermal space was estimated as being ca. 1.5 cm^3. The catalyst dilution with SiC, which has a fairly high thermal conductivity, served to lower the amount of heat released per catalyst bed volume. The particle size of the diluent (200-250 μm) and the catalyst (100-150 μm) was chosen small enough to allow for ideal plug flow behaviour with negligible wall effects as $\frac{ID_{reactor}}{d_p} > 10$ (Ertl et al., 1997), yet large enough to ensure that pressure drop across the bed was smaller than 0.1 bar at the reaction conditions applied. Furthermore with catalyst particles smaller than around 300 μm no hampering effect due to intra particle diffusion of the reactants are to be expected (Claeys, 1997; Claeys and Schulz, 2004).

0.5 g catalyst plus 0.45 g SiC were used in the series with the carbon supported catalysts and 0.2 g catalyst plus 1.2 g SiC in the series with the alumina supported model catalysts. In the latter series a lower catalyst loading was chosen to allow for experiments at higher space velocities or lower conversion respectively. To avoid segregation of catalyst and diluent during loading of the reactor, the mixtures were wettened with small amounts of de-ionised water, which was later driven off in an argon flow at elevated temperature (110 °C). Special precaution was taken to make sure that the catalyst bed is placed equidistant from the top of both limbs, i.e. positioned in the isothermal zone of the reactor (Figure 4.4). The inertness of silicon carbide and the reactor during an experiment was tested in a blank experiment. After Fischer-Tropsch synthesis, the catalysts were passivated in flowing CO_2 at room temperature for one hour, the spent catalyst was then split into two when unpacking the reactor. Selected samples of spent catalysts at the inlet side of the reactor, where a more reducing atmosphere existed, and the spent catalyst at the reactor

outlet, that was exposed to a more oxidising environment during Fischer-Tropsch experiments due to the presence of water and carbon dioxide, were characterized separately. This justifies the use of a U-shaped reactor.

4.6.3 Experimental procedure for synthesis runs

All catalyst samples were activated in-situ prior to reaction at atmospheric pressures via calcination in argon followed by reduction in pure hydrogen (flow rate of both gases: 30 ml(NTP)/min). In both treatment steps the same temperature programme was used entailing heating at a heating rate of 1 °C/min from room temperature to 350 °C, which was kept for 16 hours. After activation the reactor was switched to bypass (Figure 4.3 insert) and the catalyst bed temperature reduced to the reaction temperature, 270 °C. While the catalyst bed was cooling under argon flow, the synthesis gas, CO and H_2 flows were set at 20 ml(NTP)/min and 40 ml(NTP)/min respectively and the reference gas flow at 20 ml(NTP)/min. The system was then pressurised up to 30 bar (absolute) via a pressure controlled argon stream and adjusting the needle valve to allow a total flow of 100 ml(NTP)/min (argon and all other gases combined). Correct and stable flow rates were confirmed by chromatographic on line analysis of synthesis gas (CO and H_2) relative to the reference gas (N_2) over several consecutive bypass analyses. After this, the system is switched from bypass to flow through the reactor (Figure 4.3 insert). This point defines the start of the experiment. Progress of the reaction is then followed by regular sampling of a combination of on-line (TCD) and off-line (FID, ampoules) analytical techniques (see section 4.7.1).

4.6.4 Sampling procedure

The total composition of the combined stream of product and reference gas was sampled in their vapour state using heated glass ampoules as prescribed by Schulz and

Nehren (1986). In this technique, the capillary end of an evacuated glass ampoule is inserted, through the septum of a sampling device, into the effluent stream. The capillary is broken in the sampling device, so drawing a total vapour phase sample into the ampoule after which the capillary is partially withdrawn and sealed with a butane flame. This is illustrated in Figure 4.5. These ampoules are later crushed within an ampoule breaking device (for diagram see Appendix C) so releasing the sample contents into an off-line chromatograph for analysis of organic compounds. Inorganic gases and methane were analysed by means of on-line gas chromatography. The experimental set-up is specifically designed to study fast initial changes of catalyst activity and selectivity of synthesis gas conversion.

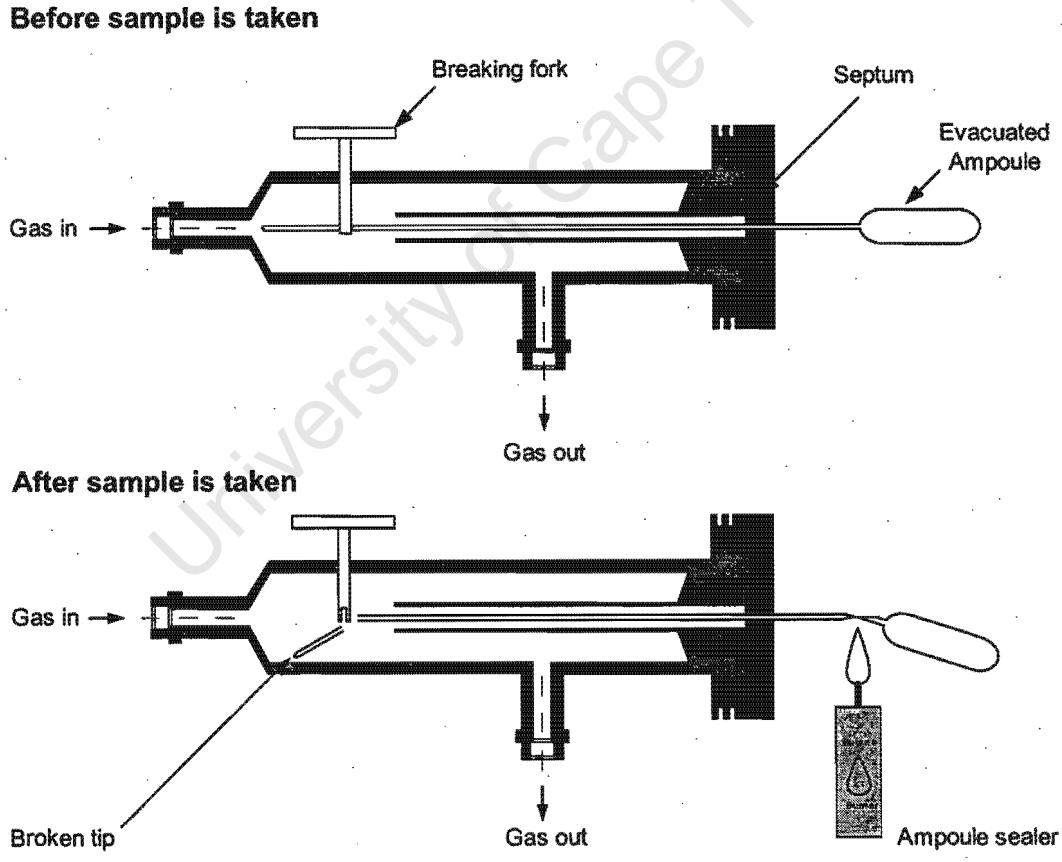

Figure 4.5: Ampoule sampling procedural setup

4.7 Product Analysis

4.7.1 Gas chromatographic analysis

Nitrogen was used as an internal standard for the on-line analysis where H_2, N_2, CO, CH_4 and CO_2 were analysed using a GC (Varian 3700) equipped with thermal conductivity detector (TCD). Cyclohexane, CH_x, which is not a product of Fischer-Tropsch synthesis at the conditions applied, was used as an internal standard for the off-line analysis of organic compounds using a temperature programmed gas chromatograph (Varian 3400) equipped with a flame ionisation detector (FID). Conditions of the two gas chromatographic analyses are given in Table 4.1 and a typical FID chromatogram is shown in Figure 4.6. Relative errors (repeatability of these analysis techniques) are typically ±3 % for TCD analyses and ±1 % for FID analyses. The internal standards which were accurately fed to the product stream were used for calculation of flow rates of inorganic and organic components and subsequently conversions, yields and selectivities.

The TCD setup was calibrated on a monthly basis using calibration gas mixtures with known composition. The peak areas: A_i, obtained from the TCD analysis were then used to calculate the relative calibration factors normalised for nitrogen, f_{TCD} for each species (Equation 4.4).

$$\left(\frac{n_i}{n_{N_2}}\right) = f_{TCD,i}\left(\frac{A_i}{A_{N_2}}\right) \tag{4.4}$$

Typical calibrations were: $f_{TCD,H_2} = 0.083 \pm 0.02$; $f_{TCD,CO} = 1.045 \pm 0.031$; $f_{TCD,CO_2} = 0.969 \pm 0.029$; $f_{TCD,CH_4} = 0.290 \pm 0.09$.

The response of a FID detector is strictly carbon specific, however oxygen containing components give a weaker response. In order to account for this, theoretical mass specific response factors have been used following an incremental approach suggested by Kaiser (1969). Here the response of all carbon atoms which are not bonded to

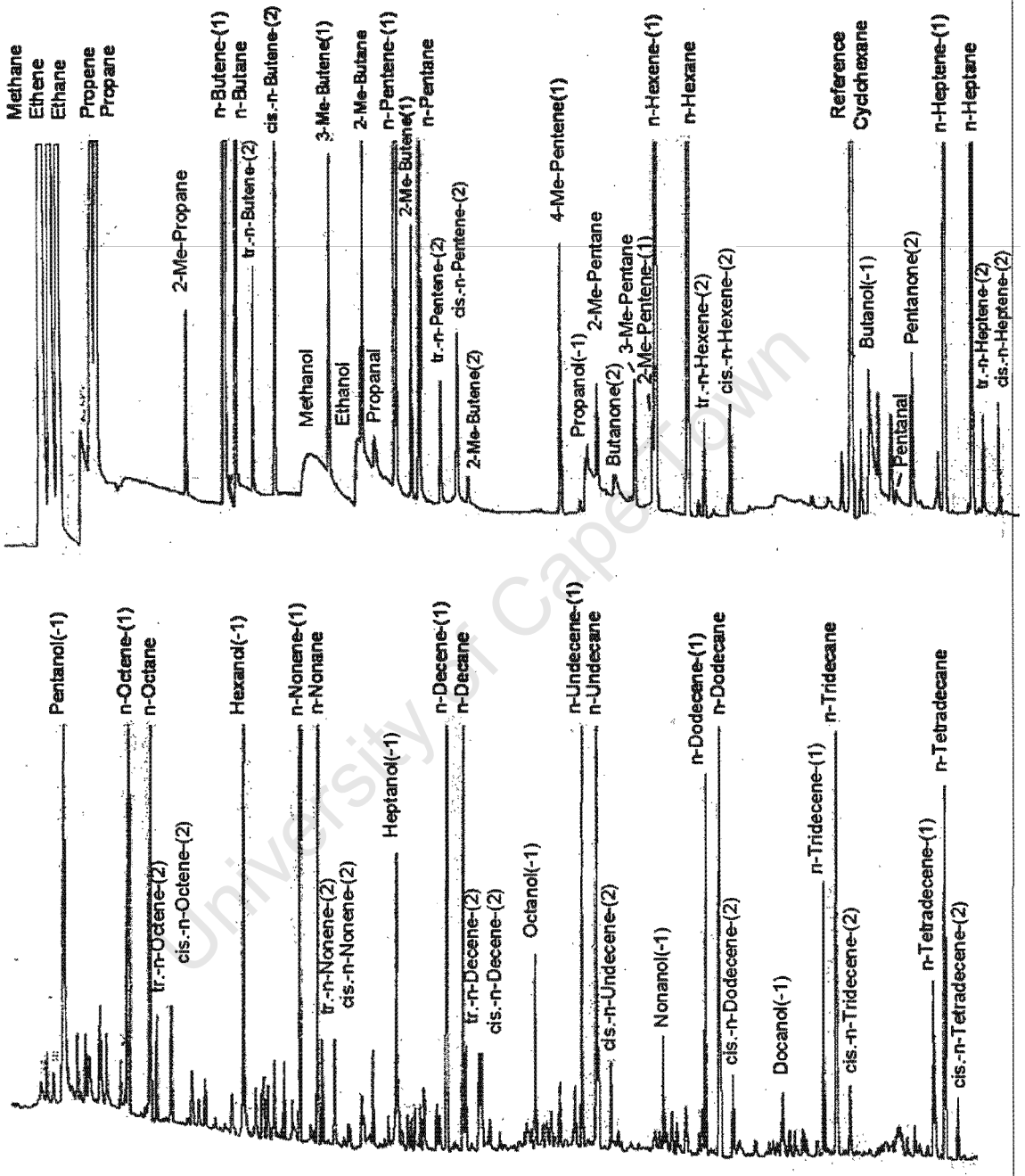

Figure 4.6: A typical chromatogram obtained from an FID analysis (only major peaks are labeled here)

Table 4.1: Conditions for gas chromatographic analyses

Gas chromatograph	**Varian 3700 (on line)**
Detector	four filament thermal conductivity detector (TCD) $T_{detector}$ = 200 °C, $T_{filament}$ = 250 °C
Column type	packed, stainless steel, 3 m x 2.1 mm
Stationary phase	CarbosieveII, 80-100 mesh (Supelco)
Carrier gas	argon
Flow rate	30 ml(NTP)/min
Analysis temperature	170 °C (isothermal)
Gas chromatograph	**Varian 3400 (off line)** (adapted to ampoule technique)
Detector	flame ionisation detector (FID), T = 250 °C
Column	RTx-1 (Restek) fused silica capillary column, 60 m x 0.25 mm stationary phase: 0.5 μm dimethyl siloxane (crosslinked)
Carrier gas	hydrogen
Introduction gas	nitrogen
Column head pressure	2.9 bar (absolute)
Injector	split injector, T = 250 °C split ratio 1:20 to 1:200 (depending on sample)
Temperature programme	-60 °C, 3 min, isothermal at 15 °C/min to -35 °C, 0 min isothermal at 10 °C/min to -5 °C, 2 min isothermal at 2.5 °C/min to 25 °C, 0 min isothermal at 5 °C/min to 250 °C, 10 min isothermal
Temperature (Ampoule breaker device)	250 °C

an oxygen atom is 1, the response of carbon atoms with a single bond to an oxygen atom is 0.55 and those carbon atoms with C=O double bonds are considered to give no response. The resulting factor for a component is then calculated using equation 4.5

$$f_i = \frac{N_C}{N_{C(\text{no O})} + 0.55 N_{C(O)}} \tag{4.5}$$

where N_C is the total number of carbon atoms in a molecule, $N_{C(\text{no O})}$ is the number of carbon atoms not connected to oxygen and $N_{C(O)}$ is the number of carbon atoms connected to one oxygen atom with a single bond.

4.7.2 Data work-up

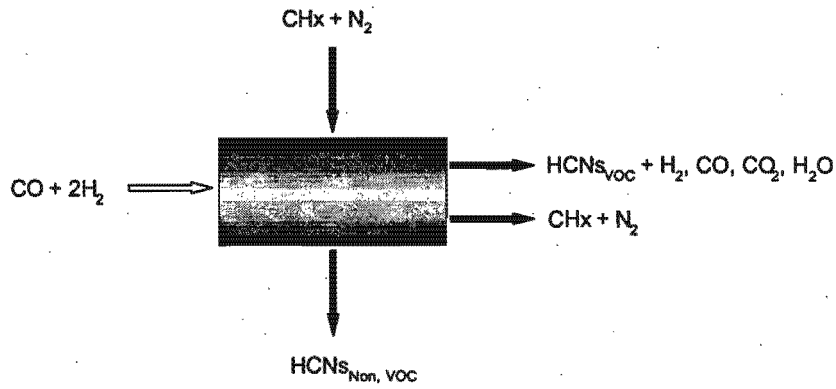

Figure 4.7: Ingoing and outgoing reactant, product and reference components required for mass balance around Fischer-Tropsch reactor (voc: volatile organic compounds; HCNs: hydrocarbons; CHx: cyclohexane)

Before Fischer-Tropsch reaction, the reactants, CO and H_2 are bypassing the reactor and samples are analysed. This will then represent the amount of reactants fed into the reactor. During Fischer-Tropsch synthesis, TCD and ampoule samples are taken and analysed whereupon peak areas for each species present are obtained and used to calculate the molar flow rate of the respective species. The molar flow rates of inorganic compounds and methane, $\dot{n}_i$, obtained from TCD analysis are given by:

$$\dot{n}_i = f_{TCD,i}\left(\frac{A_i}{A_{N_2}}\right)\dot{n}_{N_2} \tag{4.6}$$

with

$$\dot{n}_{N_2} = \frac{x_{N_2}.\dot{V}_{ref}\,(NTP)}{\widetilde{V}_A} \tag{4.7}$$

where x_{N_2} is the molar concentration of nitrogen in reference gas; $\dot{V}_{ref}(NTP)$ is the volumetric reference gas flow rate; $\widetilde{V}_A$ is the Avogadro volume. The molar flow rate of an organic compound, $\dot{n}_i$, can be derived from results of FID analyses as follows:

$$\dot{n}_i = \frac{N_{CHx}}{N_i}\frac{f_i.A_i}{f_{CHx}.A_{CHx}}.\dot{n}_{CHx} \tag{4.8}$$

with N_{CHx}, the carbon number of cyclohexane and $\dot{n}_{CHx}$ the molar flow rate of the

reference compound, cyclohexane, equalling:

$$\dot{n}_{CHx} = \frac{x_{CHx}.\dot{V}_{ref}\,(NTP)}{\tilde{V}_A} \tag{4.9}$$

The molar flow rates of individual products on a carbon basis can be expressed as:

$$\dot{n}_{i,c} = N_{CHx}\frac{f_i.A_i}{f_{CHx}.A_{CHx}}.\dot{n}_{CHx} \tag{4.10}$$

Conversion of a reactant can be calculated as being:

$$X_i = 1 - \frac{(\dot{n}_i)_{out}}{(\dot{n}_i)_{in}} \tag{4.11}$$

the yield, $Y_{i,c}$ and selectivity, $S_{i,c}$ of a product on carbon basis is:

$$Y_{i,c} = \frac{\dot{n}_{i,out}}{\dot{n}_{CO,in}} \tag{4.12}$$

$$S_{i,c} = \frac{Y_{i,c}}{X_{CO}} \tag{4.13}$$

Alternatively a selectivity / carbon content within the fraction of components which are found in ampoule samples or which are volatile at reaction conditions respectively can be defined:

$$S_{i,c,voc} = \frac{\dot{n}_{i,c}}{\sum \dot{n}_{i,c,voc}} \tag{4.14}$$

A specific Fischer-Tropsch rate as normalised for the initial metal surface are a (S_{Fe}) exposed equals:

$$r_{FT} = \frac{(\dot{n}_{CO,in} - \dot{n}_{CO,out} - \dot{n}_{CO_2,out})}{S_{Fe}} \tag{4.15}$$

Furthermore the partial pressure of a reactant or a product at the reactor exit can be calculated as follows:

$$p_{i,out} = x_{i,out}.P_{total} \tag{4.16}$$

with P_{total} the total reaction pressure and $x_{i,out}$ the molar concentration of a com-

ponent i at the reactor exit:

$$x_{i,out} = \frac{\dot{n}_{i,out}}{(\dot{n}_{CO,out} + \dot{n}_{H_2,out} + \dot{n}_{CO_2,out} + \dot{n}_{H_2O,out} + \sum \dot{n}_{i,voc})} \tag{4.17}$$

the molar flow rate of exiting water can be derived from an oxygen balance:

$$\dot{n}_{H_2O,out} = \dot{n}_{CO,in} - \dot{n}_{CO,out} - 2\dot{n}_{CO_2,out} - \sum \dot{n}_{i,ox-voc} \tag{4.18}$$

with $\dot{n}_{i,ox-voc}$: molar flow of oxygen containing volatile products.

Chapter 5

Results and Discussion

5.1 Water-in-oil microemulsions

For the microemulsion system used in this study (water, Berol 050, n-hexane), stable and optically transparent water-in-oil microemulsions were possible only in the region depicted in Figure 4.1. Phase separation or cloudy solution was noticeable outside these limits. The stability region observed is in good accordance with previous work conducted on the same microemulsion system by Stenius et al. (1984) and Boutonnet et al. (1982). Abrevaya and Targos (1987) who also conducted research on this system reported that the maximum amount of water and surfactant required to form a clear stable microemulsion at 23 °C should be 5 wt% and 15 wt% respectively, whereas the minimum amount of the oil phase should be 80 wt%. It should also be pointed out that the system used in this study is strongly sensitive to temperature. A fluffy white substance was for example obtained when temperatures dropped below 20 °C. Therefore the temperature of the microemulsions were accurately controlled and kept constant at 25 °C during the precipitations conducted.

5.1.1 Precipitation in microemulsions

The precipitation of crystallites used in this study involves mixing of two microemulsions, one containing the precursor (iron (III) nitrate) and the other containing the precipitating agent (ammonium carbonate) in aqueous solutions. Prior to the precipitation experiments using the microemulsions, the precipitation behaviour of iron (III) nitrate in the presence of ammonium carbonate was studied to characterise the changes of pH and colour of the precipitate observed during slow dropwise addition of the precipitant (2.5 ml/min) to 200 ml of iron (III) nitrate solution under stirring (800 rpm). The change of the pH value in the iron nitrate solution or suspension respectively for a precipitation of a 0.54 M iron (III) nitrate solution using 1.5 M ammonium solution at 25 °C is shown in Figure 5.1.

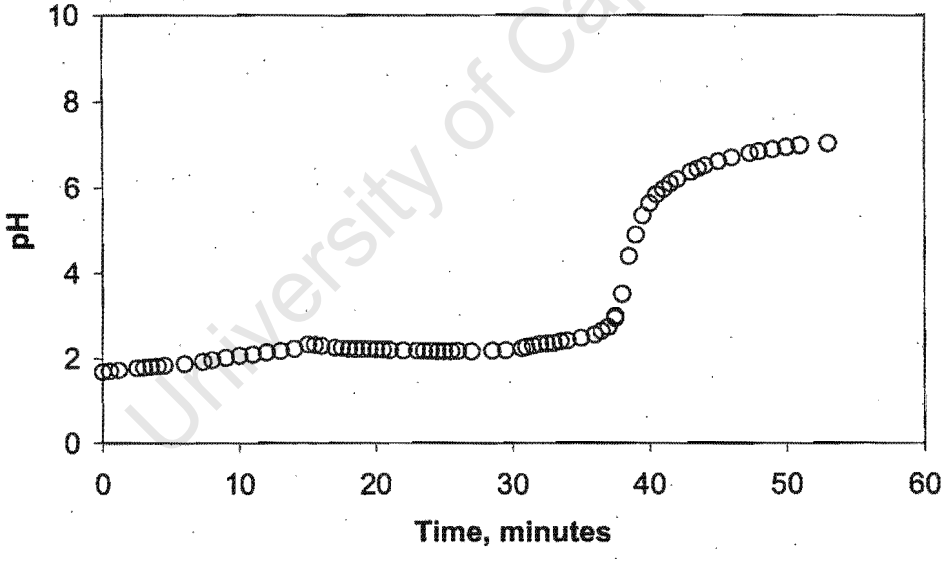

Figure 5.1: pH value variation of 0.54 M iron (III) nitrate solution (200 ml) during precipitation with 1.5 M ammonium carbonate solution (slow addition: 2.5 ml/min) at 25 °C.

The temporal change of the pH value showed a gradual initial increase of the pH value, followed by a small decrease which coincided with a change in colour from orange to red without formation of precipitate. This only occurred at pH values

larger than 3. After this, the pH rapidily rose until saturation was attained above pH=7 and completion of the precipitation with brick-red precipitate formed. The precipitation from iron (III) solutions using ammonium carbonate occurs stepwise:

$$[Fe(H_2O)_6]^{3+}_{aq} \longrightarrow [Fe(H_2O)_5OH]^{2+}_{aq} \longrightarrow [Fe(H_2O)_4(OH)_2]^{+}_{aq} \longrightarrow [Fe(H_2O)_3(OH)_3]_S$$

and the formation of iron (III) hydroxide is the final product. CO_2[1] is being formed in this reaction, the overall reaction being:

$$2[Fe(H_2O)_6]^{3+}_{aq} + 3CO^{2-}_{3,aq} \longrightarrow 2[Fe(H_2O)_3(OH)_3]_s + 3CO_{2,g} + 3H_2O_l \qquad (5.1)$$

Note that the above described method was also used in attempts to prepare nano-sized iron oxide crystallites. For this, the precipitate separated from the slurry, repeatedly washed with hot de-ionised water, dried (100 °C) and calcined (300 °C) in air. The resulting crystallites were oval shaped and had average sizes of around 7 nm with a spread comparable to that obtained with the reverse micelle method described in this thesis. However, variation of precipitation conditions did not lead to controlled shifts of the average crystallite sizes which is why the above method was abandoned. Precipitation in microemulsions differs from that described above in that reactants only mix via interchange between micelles (see Figure 5.2).

In microemulsions, precipitation of Fe^{3+} ions via diffusion of $(NH_4)_2\,CO_3$ through the continuous oil phase is rather unlikely (Pileni, 1989; Pillai et al., 1995; Ingelsten et al., 2001; Eriksson et al., 2004). Temporary fusion of droplets seem to be a prerequisite for the reaction to proceed. Figure 5.2 represents a schematic diagram of the proposed mechanism during precipitation in microemulsions. The mechanism is supported by views of other researchers (Lopez-Quintela and Rivas, 1993; Song and Kim, 1999, 2000; Agrell et al., 2001). Microemulsion systems are thought to be dynamic in the sense that during crystallite formation a constant random collision

[1]Note that there is subtle difference in the reactions of iron ions with carbonate ions depending whether the metal ion carries a 2+ or 3+ charge. The 3+ ions are sufficiently acidic to react with carbonate ions to release carbon dioxide gas and produce a precipitate of the metal hydroxide, whereas iron carbonate precipitates are formed from iron (II) solutions (Marion et al., 2003).

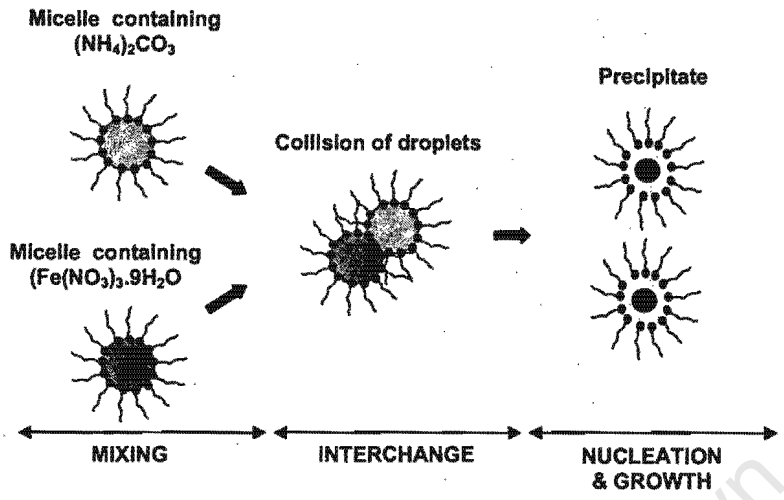

Figure 5.2: A schematic diagram of the proposed mechanism during crystallite formation (Pileni, 1989; Lopez-Quintela and Rivas, 1993; Eriksson et al., 2004)

of the droplets takes place after mixing the two microemulsions resulting in the interchange of the reactants. This interchange is believed to be fast, to such an extent that it is thought to already occur during the mixing stage (Lopez-Quintela and Rivas, 1993). Since precipitation is taking place in the nanosized domains, the size of the crystallites formed depends on the size of the water droplet and the material exchange rate between the micelles. This material exchange rate depends on the rate of droplet fusion events, which are likely governed by the type of surfactant that form the oil-water interface and the rigidity of the oil-water interface. The latter is believed to be lower in large reverse micelles (Pileni, 1989), therefore, possibly accounting for the apparently faster precipitation observed in this study at high water-to-surfactant weight ratios (see below).

In all precipitations conducted with the microemulsions of different compositions (but fixed reactant concentrations) a colour change from orange to brick-red was observed. Furthermore, in all cases, the suspensions were stable and optically transparent even after precipitation. This change in colour was fairly rapid (5-10 min) in microemulsions which had high water-to-surfactant weight ratios (large micelles), whereas in microemulsions with the lowest water-to-surfactant weight ratio (small

micelles) only after 50-60 minutes no more color change could be detected most likely indicating the rate of this reaction in the microemulsion depends on size of the reverse micelles.

5.1.2 Characterisation of microemulsions

All the eight microemulsions prepared for this study were characterized using their UV-vis light absorption behaviour and their viscosity properties.

5.1.2.1 UV-vis absorption

UV-vis absorption spectra were recorded on the iron nitrate containing microemulsions and on the microemulsions 3 hours after precipitation via addition of the corresponding ammonium carbonate containing microemulsion. The absorbance of the light yellowish iron nitrate microemulsions was too low to allow for recording reliable spectra; strong absorption over a wide range of wavelengths occurred on the microemulsions containing the brick-red precipitates (see Figure 5.3 for UV-vis spectra). No distinct band spectra were observed in the wavelength range investigated. Absorbance generally increases as the total amount of water or reactant solution respectively increases from 5 g to 20 g as would be expected from the Lambert-Beer law[2].

Quantitative information on the size of the absorbing crystallites can be derived from the threshold wavelength, λ_s (Eastoe et al., 1991; Caponetti et al., 2003), which can for example be obtained from analysis of UV-vis spectra using the following equation:

$$\left(\frac{A}{\lambda}\right)^2 = K\left(\frac{1}{\lambda} - \frac{1}{\lambda_s}\right) \tag{5.2}$$

[2] $A=\varepsilon bc$, where A is absorbance, ε is the molar absorbtivity (L/mol/cm), b is the path length of the sample (cm) and c is the concentration of the compound in solution (mol/L)

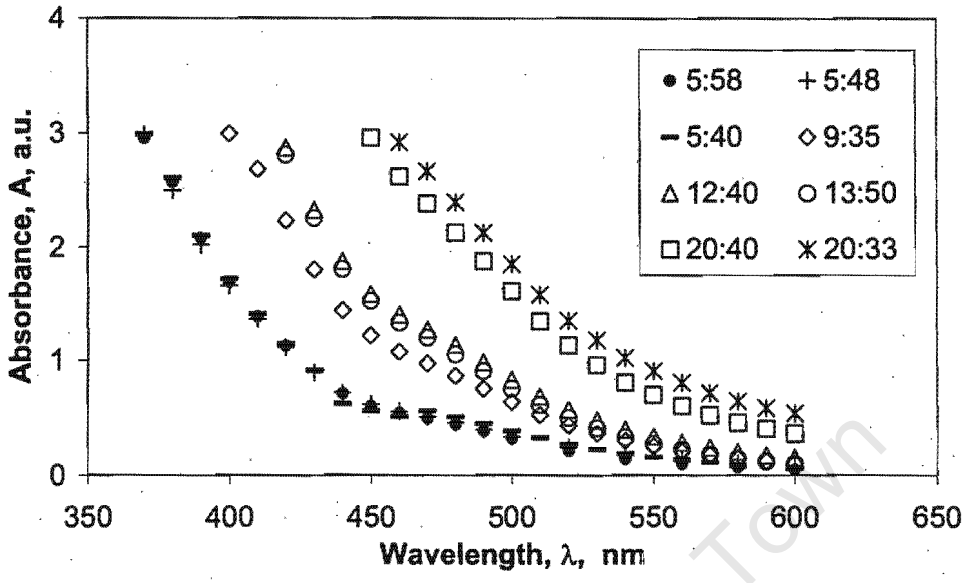

Figure 5.3: UV-vis absorption spectrum of "$Fe(OH)_3$" precipitate prepared from microemulsions with different compositions (sample code indicating amounts of water and surfactant in grams, m_{oil} = 250 g)

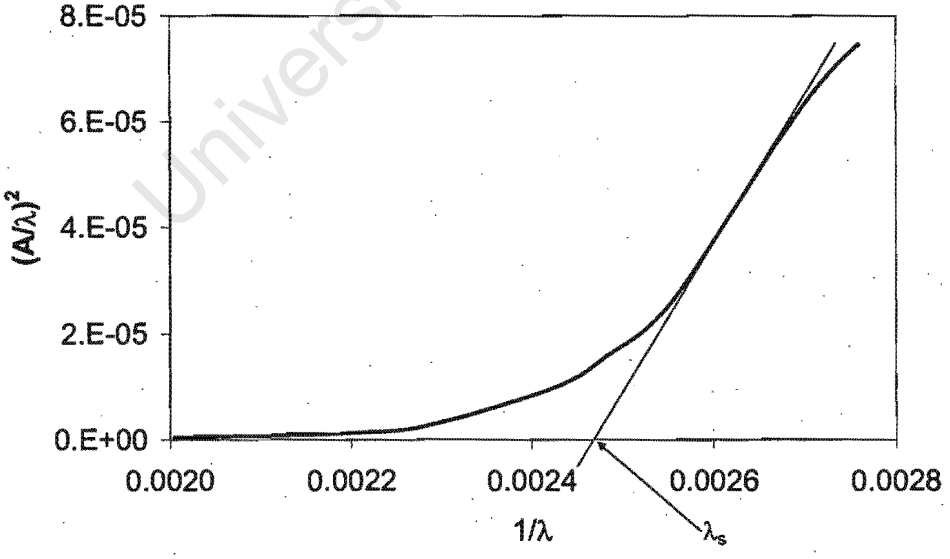

Figure 5.4: Method to obtain λ_s from typical $(A/\lambda)^2$ vs $1/\lambda$ plot

where A, λ, λ_s and K are absorbance, wavelength, threshold wavelength and an empirical constant respectively. Plotting $(A/\lambda)^2$ vs $1/\lambda$ from each spectrum, the λ_s value was obtained from the intercept on the x-axis of the tangent drawn through the inflection point; an example of this procedure is shown in Figure 5.4 for the sample with the code 9:35. The resulting threshold wavelengths (see Table 5.1) increase approximately linearly with increasing water-to-surfactant weight ratio. This increase of λ_s corresponds to an increase of the crystallite size of the precipitate ("$Fe(OH)_3$") formed in the microemulsions.

Table 5.1: Threshold wavelength (λ_s) of "$Fe(OH)_3$" precipitate prepared from microemulsions with different composition (Sample codes indicating amounts of water and surfactant in grams, m_{oil} = 250 g; ω_{wt}, water to surfactant weight ratio)

Sample Code	ω_{wt} g/g	λ_s nm
5:58	0.086	405
5:48	0.104	407
5:40	0.125	417
9:35	0.257	442
13:50	0.260	446
12:40	0.300	448
20:40	0.500	515
20:33	0.606	526

5.1.2.2 Viscosity

The viscosity of a suspension is related to the volume fraction of suspended particles (Ferguson and Kemblowski, 1991; Barnes et al., 1989). Assuming dilute dispersed suspensions (less than 10 % volume fraction) in Newtonian liquids, the work done by Einstein 1906-1911 showed that the presence of particles increased the viscosity of a liquid as a simple function of their volume fraction according to the formula (Barnes et al., 1989; Ferguson and Kemblowski, 1991):

Einstein : $\frac{\eta - \eta_o}{\eta_o} = 2.5\phi$

where ϕ is the volume fraction of the suspended particles (i.e. dispersed micelles in solution), η is the viscosity of the suspension (in this case the microemulsion solution) and η_o is the viscosity of the suspending medium (n-hexane in this case). However, Einstein's theory neglects the effects of crystallite interactions. These were accounted for analytically by Batchelor in 1977 who introduced a modified equation (Barnes et al., 1989; Ferguson and Kemblowski, 1991):

Batchelor : $\frac{\eta-\eta_o}{\eta_o} = 2.5\phi + 6.2\phi^2$

A number of experimental determinations of the coefficient of ϕ^2 have been made and work done by Cheng and Schachman in 1955 (Kinugasa et al., 2002) produced the following equation:

Chen & Schachman : $\frac{\eta-\eta_o}{\eta_o} = 2.5\phi + 14.1\phi^2$

For a microemulsion system, assuming that micelles are dispersed spherical particles and the aggregation number, n_{ag}[3], is constant, the waterpool size, r_w, can be estimated from the following derived equation (see Appendix E for derivation):

$$r_{wp} = \left(\frac{V_w}{V_T}\right)^{\frac{1}{3}} \left(\frac{t_s}{\phi^{\frac{1}{3}} - \left(\frac{V_w}{V_T}\right)^{\frac{1}{3}}}\right) \tag{5.3}$$

where V_w is the volume of water present, V_T is the total volume of the solution and t_s is the thickness of surfactant layer corresponding to the length of the surfactant molecule[4]. It is noteworthy that Equation 5.3 was derived starting from the definition of the volume fraction of the dispersed spheres in solution (Kinugasa et al., 2002)

$$\phi = N_A V_{rm} C_{rm} = \frac{N_A V_{rm} C_s}{n_{ag}} \tag{5.4}$$

where V_{rm} is the volume of a reverse micelle, C_{rm} is the concentration of reverse micelles, C_s is the concentration of the surfactant and N_A is the Avogadro's constant.

[3]The average number of surfactant molecules that make up a single micelle

[4]$t_s(\text{Å}) = 1.5 + 1.265N_C$ (Tanford, 1972) where N_C is the number of carbon atoms in the chain.

Table 5.2 shows the viscosities of microemulsions before (Fe^{3+} solution) and after precipitation ("$Fe(OH)_3$" solution) and the calculated volume fractions based on the three viscosity correlation equations. Note that there is no significant difference in viscosities of the microemulsions before and after precipitation clearly indicating that upon mixing of the two microemulsions the micelle size does not change significantly.

Table 5.2: Viscosity (η) of microemulsion systems before and after precipitation and respective volume fraction of dispersed spheres in the precipitated suspension (Sample codes indicating amounts of water and surfactant in grams, m_{oil} = 250 g; ω_{wt}, water to surfactant weight ratio)

Sample Code	ω_{wt} g/g	Fe^{3+} η, cp	$Fe(OH)_3$ η, cp	ϕ_{Cheng} -	$\phi_{Batchelor}$ -	$\phi_{Einstein}$ -
5:58	0.086	0.90	0.88	0.093	0.111	0.142
5:48	0.104	0.85	0.85	0.084	0.099	0.123
5:40	0.125	0.82	0.82	0.074	0.086	0.105
9:35	0.257	0.82	0.82	0.074	0.086	0.105
13:50	0.260	0.88	0.88	0.093	0.111	0.141
12:40	0.300	0.85	0.85	0.084	0.099	0.123
20:40	0.500	0.88	0.89	0.096	0.115	0.148
20:33	0.606	0.86	0.85	0.084	0.099	0.123

The waterpool size was then obtained from the calculated volume fraction ϕ, using equation 5.3. The results are plotted in Figure 5.5 together with micelle sizes obtained from Equation 5.5. Equation 5.5 was idealistically derived from the definition of water-to-surfactant weight ratio, ω_{wt} (see Appendix E for its derivation). However, like Einstein's equation, this equation does not include particle-particle interactions and is independent of viscosity of the solution.

$$r_{wp} = \frac{t_s}{\left(\frac{\rho_w + \omega_{wt}\rho_s}{\omega_{wt}\rho_s}\right)^{\frac{1}{3}} - 1} \tag{5.5}$$

where ρ_w is the density of water and ρ_s is the density of the surfactant.

Qualitatively, Figure 5.5 shows that there is a linear relationship between the water

pool size and water-to-surfactant weight ratio. Quantitatively, it is also interesting to note that just by increasing the water-to-surfactant weight ratio in the range 0.1 to 0.6 g/g the water pool size is increased approximately 5-fold from *ca.* 5 nm to ca. 25 nm. The water-to-surfactant weight ratio is therefore an important parameter to vary if a wide range of water pool sizes is required. It is also worth noting that the equation derived in this work and Einstein's correlation equation, both of which do not take particle-particle interactions into account, seem to underestimate the water pool size formed compared to other correlation equations which include particle interaction. Nevertheless, the micelle sizes obtained in this work and Einstein's coincided and also confirmed the linear relationship of micelle size versus water-to-surfactant weight ratio.

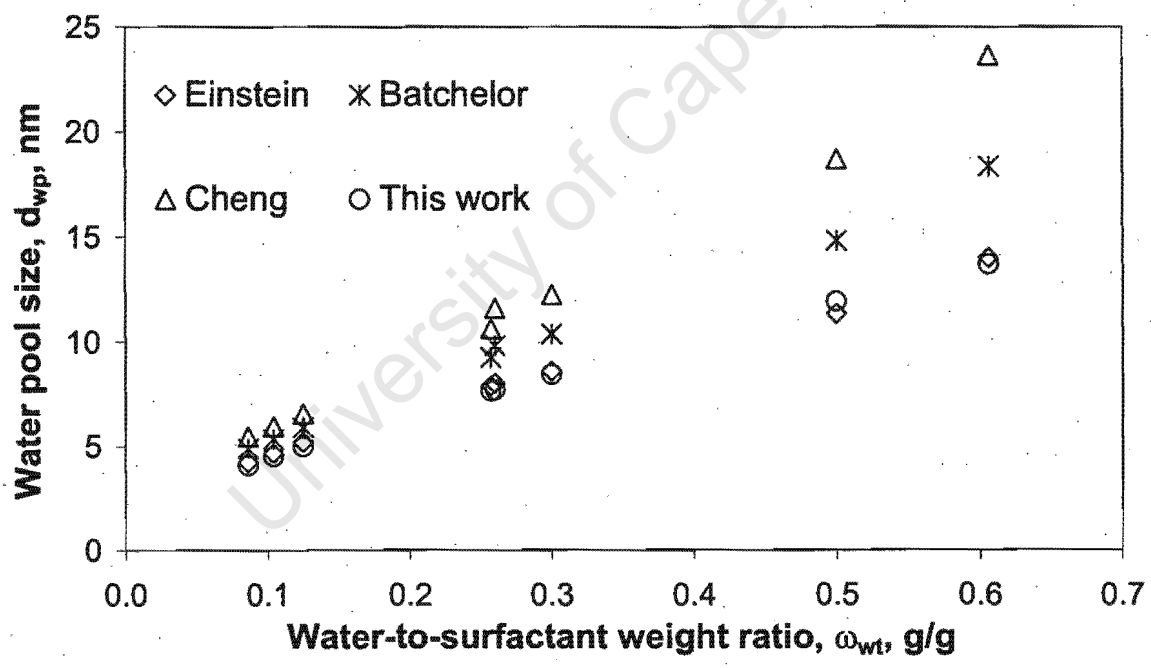

Figure 5.5: Water pool size, d_{wp}, as estimated by viscosity measurements and correlation equations

Previous studies on a number of microemulsion systems including water/PE4LE[5]/n-hexane (Hall et al., 1998), water/PEGDE[6]/hexadecane (Stenius et al., 1984), water/

[5]polyoxyethylene-4-laurylether
[6]pentaethyleneglycoldodecylether ("Berol")

CTAB[7]/hexanol (Nagy et al., 1983) also reported linear dependency of micelle size with water-to-surfactant weight ratio. This is thought to be resulting from the fact that for a fixed amount of surfactant, the interfacial area which can be stabilised by the surfactant is fixed. For that reason, new water pools cannot be formed if the water-to-surfactant weight ratio is increased and therefore the water pools must swell to accommodate the extra water added to the system (Hall et al., 1998). Presumably, when the amount of aqueous and oil phases is fixed, an increase in the amount of surfactant, within the stability region, will increase the number of droplets and consequently the size of water droplets will decrease. At the same metal salt concentration, a decrease in water droplet size causes the number of metal ions per droplet to decrease as well.

Varying the oil phase will most likely affect the micelle interaction by changing the diffusivity of a micelle droplet thereby affecting the rate of droplet collision. Assuming that the micelle size ($d_{rm} = 2(t_s + r_{wp})$) obtained from viscosity measurements is the hydrodynamic diameter of the suspended micelle droplets, one can estimate the diffusion constant of each of the microemulsion systems using the Stokes-Einstein relation (Atkins, 1990).

$$D_o = \frac{k_B T}{3\pi\eta d_{rm}} \tag{5.6}$$

where k_B is Boltzmann's constant, T is temperature, η is the viscosity of the solvent (n-hexane) and d_H is the size of the water pool plus the layer of surfactant molecules which surrounds the water pool. Since Stoke-Einstein's relation is strictly applicable at finite dilution, the experimentally determined diffusion constant needs to be compensated for particle-particle interaction (Hou et al., 1988; Ingelsten et al., 2001).

$$D = D_o(1 + \alpha\phi) \tag{5.7}$$

where α is the diffusional viral coefficient and ϕ is the volume fraction of the dispersed phase. Based on Hou et al. (1988), α has been estimated to equal 0.4. Since

[7]cetyltrimethylammonium bromide

Cheng & Schachman's correlation equation is based on experimental data, the sizes obtained using this equation were used to estimate the diffusion constant (see Table 5.3). The higher the diffusion constant, the longer the diffusion path and therefore, the less the interaction effect between micelles will be.

Table 5.3: Estimated diffusion constant (D) for the microemulsion systems prepared in this study (Sample codes indicating amounts of water and surfactant in grams, m_{oil} = 250 g; ω_{wt}, water to surfactant weight ratio; d_{rm}, reverse micelle size)

Sample Code	ω_{wt} g/g	d_{rm} nm	D(x10^{-10}) cm^2/s
5:58	0.086	11.3	6.14
5:48	0.104	11.8	5.87
5:40	0.125	12.4	5.56
9:35	0.257	16.5	4.20
13:50	0.260	17.5	3.99
12:40	0.300	18.1	3.84
20:40	0.500	24.6	2.84
20:33	0.606	29.5	2.35

5.1.3 Summary of characterisation of microemulsions

The difference in the UV-vis absorption of microemulsions after precipitation clearly indicates that the change in absorbance resulted from $Fe(OH)_3$ precipitates with different crystallite sizes. Viscosity studies showed that upon mixing the two microemulsions, the micelle sizes before and after precipitation did not change significantly. Generally, in both cases, a characteristic linear relationship between the micelle size and water-to-surfactant weight ratio is observed.

5.2 Characterisation of unsupported crystallites

5.2.1 TEM analysis of unsupported crystallites

Based on precipitation chemistry, the resulting precipitate is an iron hydroxide, $Fe(OH)_3$. The iron oxide powder obtained after drying (120 °C) and calcining (300 °C) in air was characterized to ascertain the size and distribution of crystallites, their morphology, crystal phases present and their reduction behaviour.

Figure 5.6 shows the TEM micrographs of the obtained crystallites and the corresponding histograms revealing the size distribution of nanocrystallites, which were measured directly from the TEM images ($d_{c,l}$), are depicted in Figure 5.7. It is apparent that the resulting nanostructured powders prepared by the water-in-oil microemulsion method show uniform crystallites with mostly spherical morphology. This suggests that crystallite growth within the reverse micelles is spatially constrained by the intrinsic size and shape of the reverse micelle. Based on TEM results, it was possible to synthesise eight different sizes within a wide range of 2 to 16 nm by adjusting the composition of the microemulsions. It can be observed from Figure 5.7 that with an increase in water-to-surfactant weight ratio, which corresponds to an increase of the micelle size (see previous section), the average crystallite size becomes larger and the size distribution of the crystallites is widened. The crystallite size distributions were narrow with standard deviations between 15 % and 22 % when expressed as a percentage of the mean crystallite size (see also Table 5.5).

5.2.2 XRD analysis of unsupported crystallites

The size of the crystallites were also determined from XRD characterisation, the XRD patterns are shown in Figure 5.8. With decreasing water-to-surfactant weight ratio peak broadening was observed indicating that the crystallite size becomes

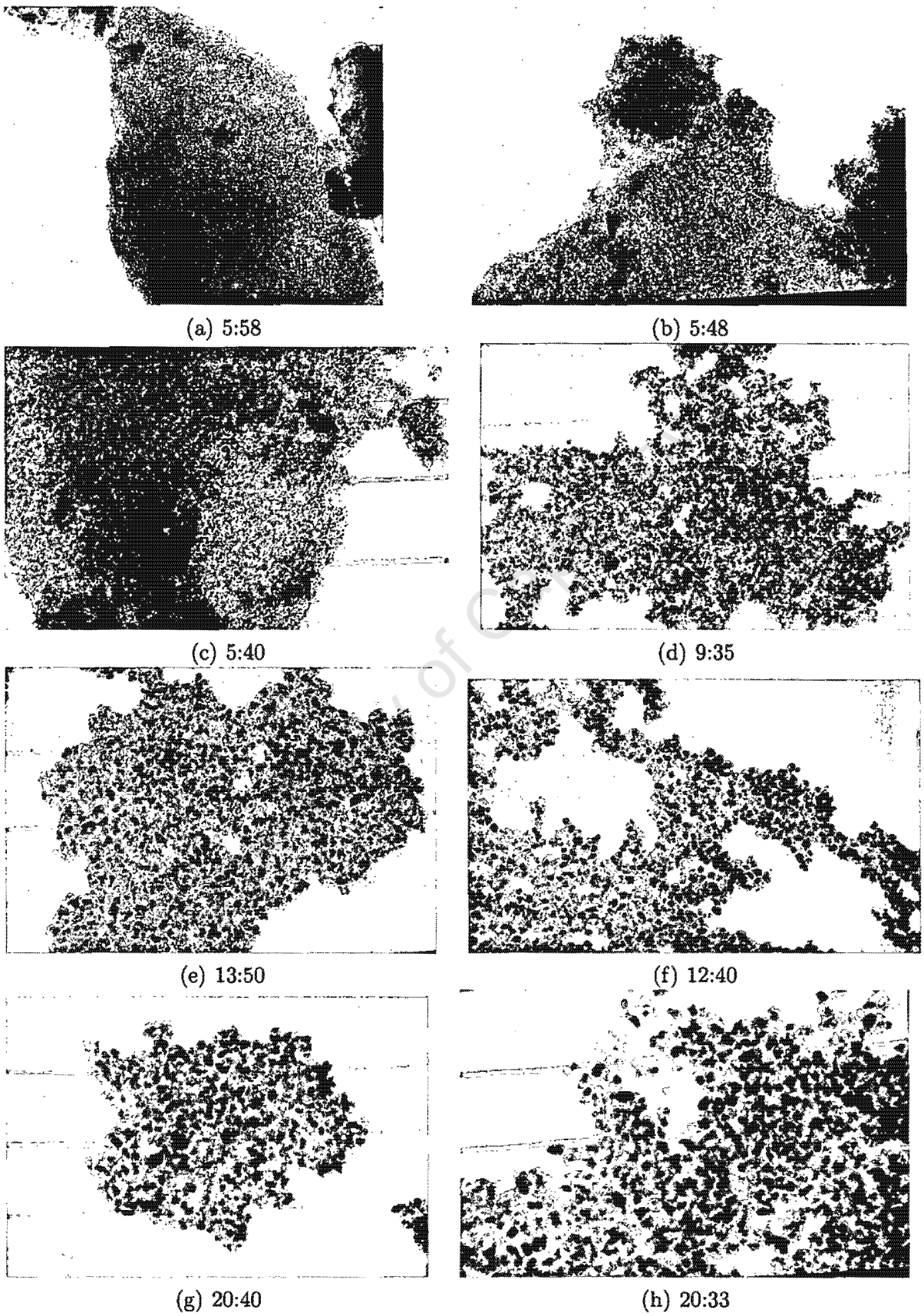

(a) 5:58 (b) 5:48

(c) 5:40 (d) 9:35

(e) 13:50 (f) 12:40

(g) 20:40 (h) 20:33

Figure 5.6: TEM micrographs of unsupported iron oxide crystallites prepared in microemulsions of different composition (sample codes indicating amounts of water and surfactant in grams, m_{oil} = 250 g). (Scale: 1 mm represents 20 nm)

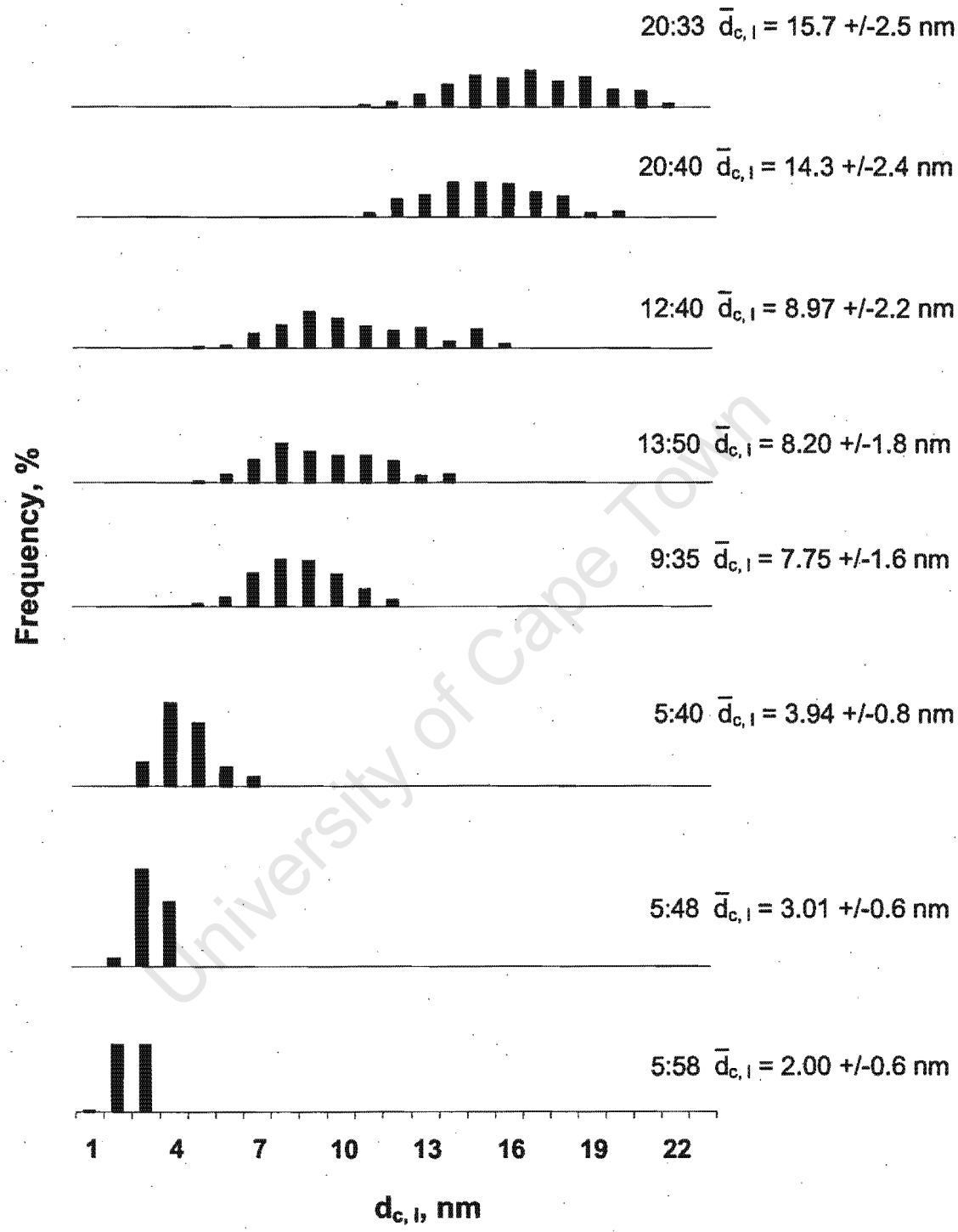

Figure 5.7: Crystallite size distributions of unsupported iron oxide powders prepared in microemulsions of different composition as determined by means of TEM analysis (sample codes indicating amounts of water and surfactant in grams, m_{oil} = 250 g)

smaller. With samples 5:48 (not shown) and 5:58, almost no peaks could be seen, meaning the crystals are very small. When comparing the XRD patterns with literature reference patterns (see also Figure 5.8), it can be seen that samples with the large crystallites (13:50, 12:40, 20:40 and 20:33) mainly consist of hematite, Fe_2O_3, whereas in samples with small crystallites (5:40, 5:48, 5:58 and 9:35) increasing amounts of magnetite, Fe_3O_4, were found. It should be noted that maghemite, $\gamma - Fe_2O_3$, has an XRD pattern identical to that of Fe_3O_4, however, temperature programmed reduction of the crystallites of different sizes indeed suggest the presence of magnetite particularly in small crystallites.

The presence of Fe_3O_4 is somewhat unexpected seeing that the material was calcined in air at 300 °C. It is however known that surfaces of hematite are usually found covered with a layer of magnetite (Catlow et al., 1997). It might be speculated that as the fraction of surface atoms becomes larger in small crystallites the relative amount of magnetite might increase correspondingly. The crystallite size was estimated using the Debye-Scherrer equation on the sharp peaks corresponding to a 110 plane ($2\theta = 35.6°$) of synthesised hematite, for large crystallites and a 311 plane ($2\theta = 35.4°$) of synthesised magnetite, for small crystallites. Results are listed in Figure 5.8.

The average crystallite diameters were also estimated using results from BET analyses, assuming spherical crystallite shape and the density of Fe_2O_3 ($\rho = 5.27$ g/cm^3), which is almost identical to the density of Fe_3O_4 ($\rho = 5.18$ g/cm^3). The average volume-based diameters of the unsupported crystallites obtained with the three methods, TEM, XRD and BET are plotted in Figure 5.9 as function of water-to-surfactant weight ratio. Note that the length based distribution as directly obtained from TEM evaluation have been converted into volume based ones to allow for direct comparison with the results obtained with the other techniques (All data are summarised in Table 5.5). It can be seen that the data obtained with the three methods are in good agreement. Furthermore, a strict linear dependency of the

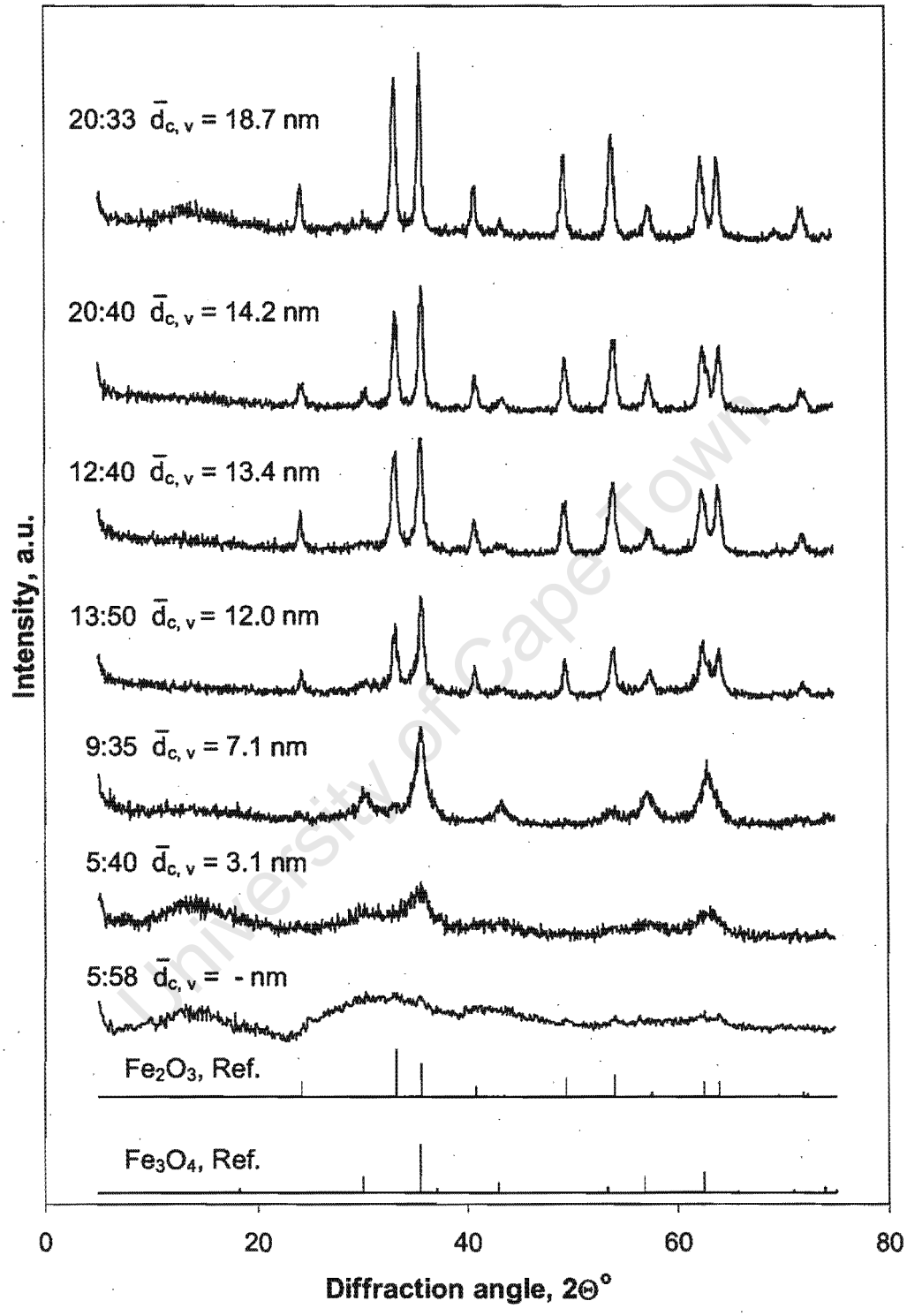

Figure 5.8: X-ray diffraction patterns of unsupported iron oxide prepared in microemulsions of different composition (sample codes indicating amounts of water and surfactant in grams, m_{oil} = 250 g). Also shown are reference patterns of hematite (Fe_2O_3) and magnetite (Fe_3O_4)

average crystallite diameter with increasing water-to-surfactant weight ratios is observed therefore rendering this ratio a simple and important design parameter for crystallite preparations using reverse micelles.

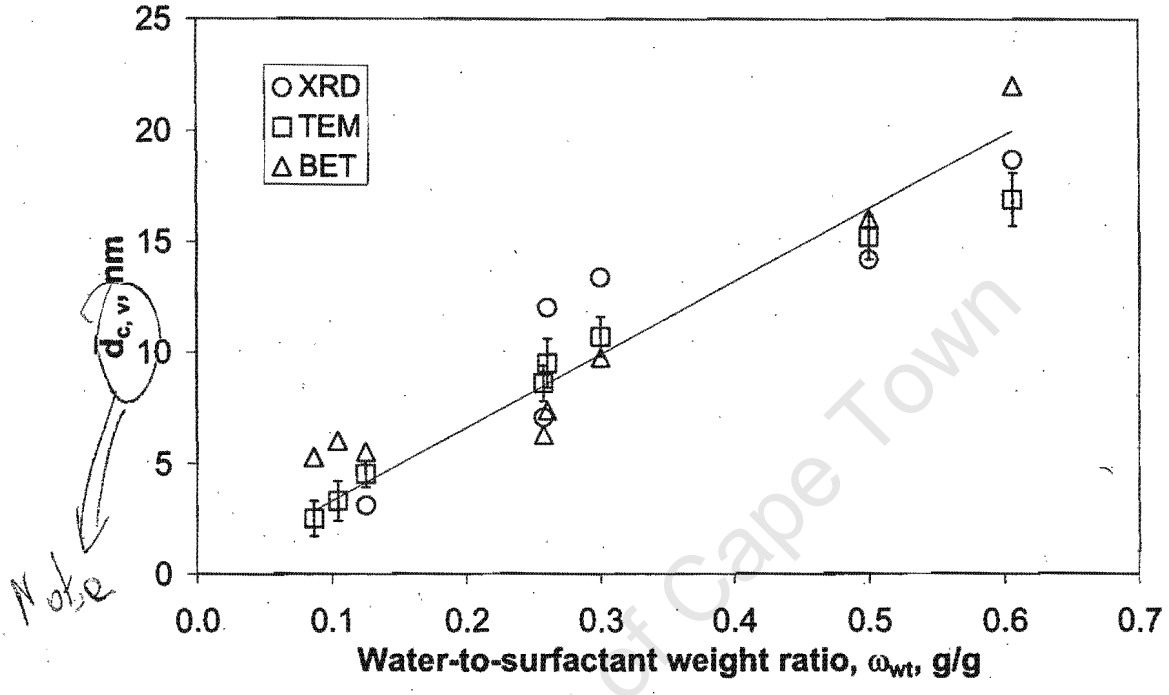

Figure 5.9: Effect of water-to-surfactant weight ratio on mean volume based diameters of unsupported iron oxide crystallites as characterized by means of TEM, XRD and BET

This linear dependency with crystallite diameters formed from microemulsions was also reported by *inter alia* Nagy et al. (1983), Pileni (1989), Schwuger et al. (1995) and Limin et al. (1996), and it is obviously due to the linear dependency of the corresponding droplets in the microemulsion before precipitation (see previous section). It can be assumed that each micelle acts as a microreactor, its size and amount of iron ions determining the size of the resulting crystallites. Generally, the "shell" of large water droplets in microemulsions is less rigid (Pileni, 1989) therefore allowing a more facile exchange of material among micelles. This might even include exchange of nuclei and crystallites thus leading to their agglomeration or flocculation, therefore resulting in wider crystallite size distribution in crystallites prepared from microemulsions with high water to surfactant ratios (Schwuger et al., 1995; Limin

et al., 1996), as also observed in this study.

It should be noted that the exchange of nuclei or crystallites is only to be expected in microemulsion systems, which allow for temporary coalescence of micelles to form transient dimers (Pileni, 1989; Lopez-Quintela and Rivas, 1993; Eriksson et al., 2004) (see Figure 5.2). In any case, the fast exchange of reactants between larger droplets will lead to higher reaction rates (Caponetti et al., 2003) and therefore a faster completion of the crystallite growth process. This effect is counteracted by slower diffusivity of large micelles in the microemulsion (see section 5.1.2.2). However, judged from the colour changes (yellow-orange to brick-red) during precipitation using the different microemulsions in this work, precipitation in the large droplets occurred much faster (5-10 min) than that in the smaller droplets (50-60 min), indeed suggesting that the effective exchange of material/reactants is much faster in the larger droplets.

5.2.3 Reduction behaviour of unsupported crystallites

The iron oxide crystallites were further characterised by means of temperature programmed reduction in a hydrogen/argon mixture. The recorded hydrogen consumption obtained on the eight samples is shown in Figure 5.10. All curves show two peaks, indicative of the two step reduction of hematite, Fe_2O_3 to magnetite, Fe_3O_4 (Kock et al., 1985; Iglesia et al., 1993; Raje et al., 1998; Lin et al., 2003) and magnetite to metallic iron.

$$3Fe_2O_3 + H_2 \longrightarrow 2Fe_3O_4 + H_2O \tag{5.8}$$

$$2Fe_3O_4 + 8H_2 \longrightarrow 6Fe + 8H_2O \tag{5.9}$$

The broadness of the second peak indicates the transformation of Fe_3O_4 to Fe to be a relatively slow process (Bukur et al., 1995; Jin and Datye, 2000). According to

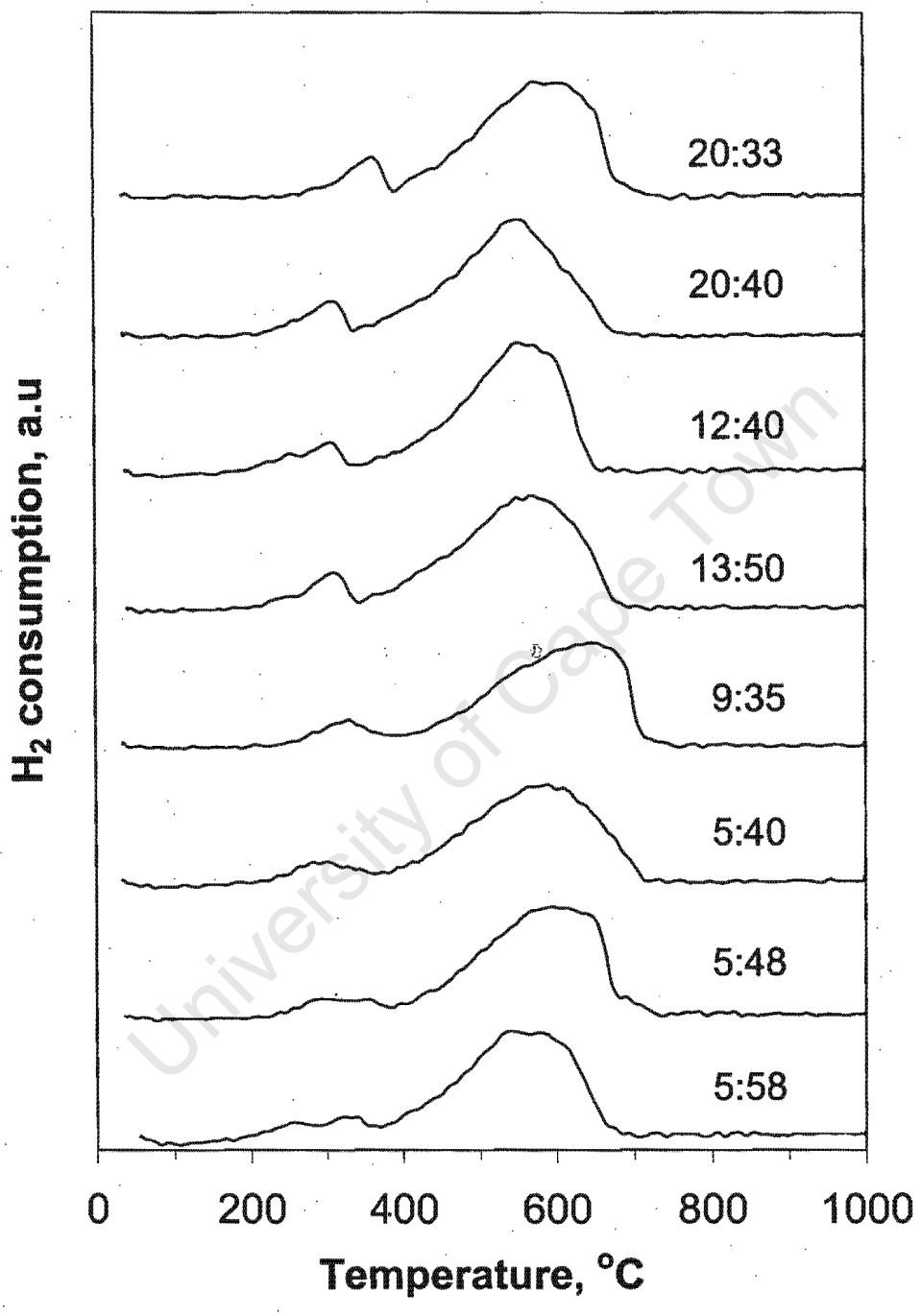

Figure 5.10: TPR patterns of unsupported iron oxide crystallites prepared in microemulsions of different composition (sample codes indicating amounts of water and surfactant in grams, m_{oil} = 250 g)

the above equations $\frac{1}{9}$ or 11 % of the hydrogen required for complete reduction of Fe_2O_3 to Fe, is needed for the first reduction step from Fe_2O_3 to form Fe_3O_4. It is evident from the TPR spectra that complete reduction was obtained in all samples. The percentage of the area of the first peak can therefore give an indication of the composition (ratio Fe_2O_3/Fe_3O_4) of the iron oxide crystallites. The relative peak area of the first peak decreases with decreasing crystallite size, therefore suggesting a lower content of Fe_2O_3 in these samples (see Table 5.4). These results of this estimate are in qualitative agreement with the above reported XRD results.

Table 5.4: Area percentage of first peak in TPR spectra and estimated phase composition of unsupported iron oxide crystallites prepared in microemulsions of different composition (sample codes indicating amounts of water and surfactant in grams, m_{oil} = 250 g)

Sample Code	ω_{wt} g/g	$\bar{d}_{c,l}$ – TEM nm	$A_{1^{st}peak}$ %	Fe_2O_3 – content[a] mol%
5:58	0.086	2.0	3.8	34.5
5:48	0.104	3.0	4.7	42.7
5:40	0.125	3.9	4.8	43.6
9:35	0.257	7.7	8.0	72.2
13:50	0.260	8.2	8.9	80.9
12:40	0.300	9.0	8.8	80.0
20:40	0.500	14.3	9.2	83.6
20:33	0.606	15.7	9.3	84.5

[a]rest: mol% Fe_3O_4

From the TPR curves it can also be observed that the temperature required to reduce the crystallites is not dependent on their size as the peak positions are always found at the same temperatures, namely ca. 300-350 °C for the low temperature peak and ca. 550-600 °C for the high temperature peak.

5.2.4 Summary of characterisation results and conclusions

In conclusion, the applied microemulsion precipitation technique has resulted in uniform iron oxide crystallites, the average size of which can be adjusted accordingly over a range between 2 - 16 nm via the water to surfactant ratio in the microemulsion (see Table 5.5). It should be noted that systematic studies dealing with preparation of iron oxide crystallites of size range from microemulsions are according to the author of this thesis not available in literature. The size range of the prepared crystallites, although they were not present as single crystal phases, was considered ideally suited for the anticipated Fischer-Tropsch reaction work. The results of the preparation of these crystallites deposited on supports is given in the following chapter.

Table 5.5: Unsupported iron oxide crystallites prepared in microemulsions of different composition (sample codes indicating amounts of water and surfactant in grams, m_{oil} = 250 g). Average crystallite sizes obtained by means of different characterisation techniques

Sample	ω_{wt}	XRD	BET	TEM	
Code	g/g	$\overline{d}_{c,v}$, nm	$\overline{d}_c$, nm	$\overline{d}_{c,l} \pm\sigma^a$, nm	$\overline{d}_{c,v} \pm\sigma$, nm
5:58	0.086	-	5.3	2.0 ± 0.57	2.5 ± 0.69
5:48	0.104	-	6.0	3.0 ± 0.61	3.3 ± 0.69
5:40	0.125	3.1	5.5	3.9 ± 0.86	4.5 ± 1.04
9:35	0.257	7.1	6.3	7.7 ± 1.62	8.6 ± 1.78
13:50	0.260	12.0	7.4	8.2 ± 1.83	9.5 ± 2.24
12:40	0.300	13.4	9.8	9.0 ± 2.23	10.7 ± 2.76
20:40	0.500	14.2	16.0	14.3 ± 2.36	15.2 ± 2.19
20:33	0.606	18.7	22.0	15.7 ± 2.54	16.9 ± 2.74

[a]Standard deviation : $\sigma = \sqrt{\frac{1}{n}\sum_{i=1}^{n}(d_i - \overline{d})^2}$; $\overline{d}$ is mean diameter; n is number crystallites measured

5.3 Catalyst characterisation

The microemulsion systems with the sample codes 5:58, 5:48, 5:40, 9:35, 13:50, 20:40 and 20:33 were chosen to prepare supported catalysts for the evaluation of influence of crystallite size (for details on the preparation see Section 4.4). The sample codes of the supported and potassium promoted catalysts were constructed from the average number or length based crystallite sizes as determined by TEM of reduced catalyst samples. As an example A03 stands for 3 nm sized crystallites supported on alumina; C16 stands for 16 nm sized crystallites supported on activated carbon. In this section the term 'fresh catalyst' refers to a sample of the catalyst in its oxidised state as obtained after catalyst preparation including calcining steps and the term 'reduced catalyst' stands for catalysts that have undergone a reductive hydrogen pretreatment in an external glass tube fluidised bed reactor at conditions identical to the pretreatment conditions applied in-situ prior to runs in the fixed bed Fischer-Tropsch reactor (30 ml(NTP)/min flow of hydrogen at 350 °C for 16 hrs). Thereafter the samples were passivated in flowing CO_2 at 25 °C for 1 hr. This process is commonly used to inertise reduced samples, which would otherwise reoxidise rapidly upon exposure to air. It is believed that a thin protective oxide layer is formed around the reduced crystallites, without affecting the crystallite morphology/size. The characterisation of reduced catalysts was considered crucial as they allow to ascertain the phases present after reduction and determine the exact metal crystallite size just before any catalytic test experiments. This was also done to check for any changes in crystallite size that might have been induced by pretreatment of the catalyst.

The iron content in the fresh catalysts were determined using SEM-EDX analysis. The results of these analysis showed iron loadings between only 3-5 wt% which are much lower than the anticipated 10 wt% (for analysis results see Table 5.7). It is believed that some iron was lost during the removal of the surfactant in the washing steps applied, particularly during preparation of small crystallites. In addition

to that some of the iron crystallites could be seen stuck on the glassware during the drying steps in the rotar vapour. The contacting of the freshly precipitated crystallites therefore seemed not to be fully efficient.

5.3.1 TEM analysis of supported crystallites

TEM micrographs of both fresh and reduced catalysts are shown in Figure 5.11 and 5.12 respectively. It can be seen that the crystallites are mainly found on the support material. Generally a more homogeneous distribution of crystallites was found on alumina supported samples especially in samples bearing small crystallites. This could be due to the pore structure of these supports. The carbon support has average pore sizes of about 2 nm (see Appendix B for BET analysis) which is too small to accommodate crystallites used in this study.

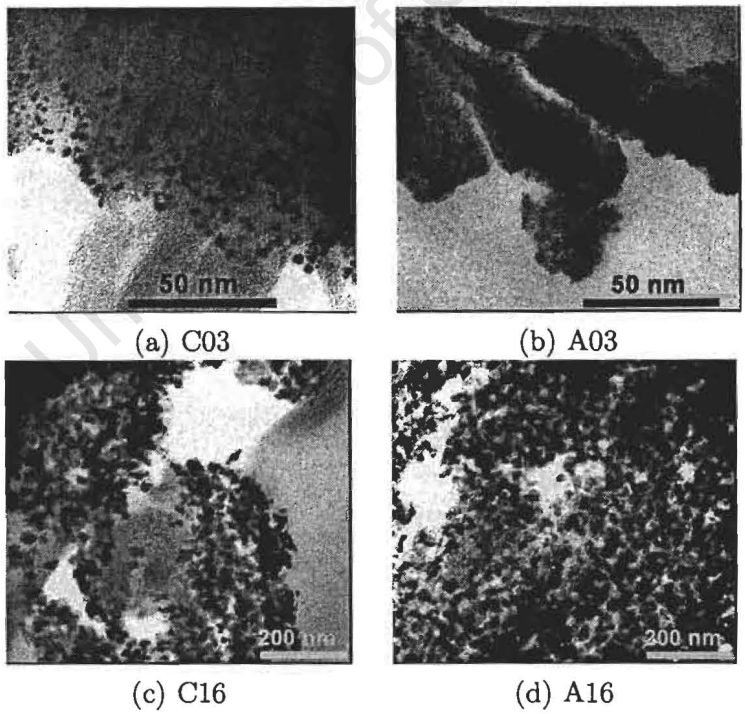

(a) C03 (b) A03

(c) C16 (d) A16

Figure 5.11: TEM micrographs of fresh supported catalysts; *left*: carbon supported catalysts, *right*: alumina supported catalysts (Note that crystallite size in sample code refers to size of reduced crystallites)

Thus, for the carbon series, all crystallites were located on the external surface of the support. The alumina support has an average pore size of 12 nm, big enough to accommodate the smaller crystallites hence these are evenly distributed on the support. Clusters of crystallites could be seen on some TEM micrographs. This was noticed mostly with carbon supported catalysts and was less pronounced on the alumina supported samples. SEM-EDX analysis confirms that some of the crystallites were not attached to the support material (see Appendix D), suggesting that the method of contacting the precipitate present in the reverse micelles with the support should still be improved in future work.

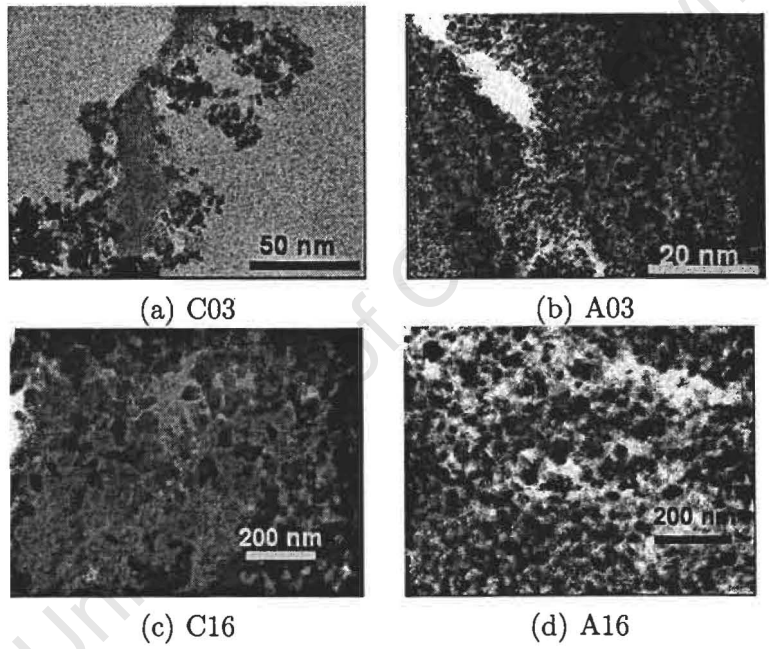

(a) C03 (b) A03

(c) C16 (d) A16

Figure 5.12: TEM micrographs of reduced supported catalysts; *left*: carbon supported catalysts, *right*: alumina supported catalysts

TEM analysis of the reduced and passivated catalysts show that although even more crystallites were present in clusters, the crystallite sizes remain largely unaffected by the reduction procedure therefore showing that no severe sintering processes occurred. Figure 5.13 shows the size distribution of the crystallites on fresh and reduced catalysts obtained from evaluating the TEM micrographs. Average crystallite sizes and standard deviations of the distributions obtained are listed in Table

5.6. It is interesting to note that - although following identical preparation procedures (except from the step of support addition) in the microemulsions - somewhat larger crystallites were found in the fresh supported catalysts of both series when comparing with the corresponding unsupported crystallites. It is not believed that the additional step of support addition should be the reason for this as it should not have any effect on the size of the precipitate formed in the reverse micelles since this process should have come to completion long before the addition.

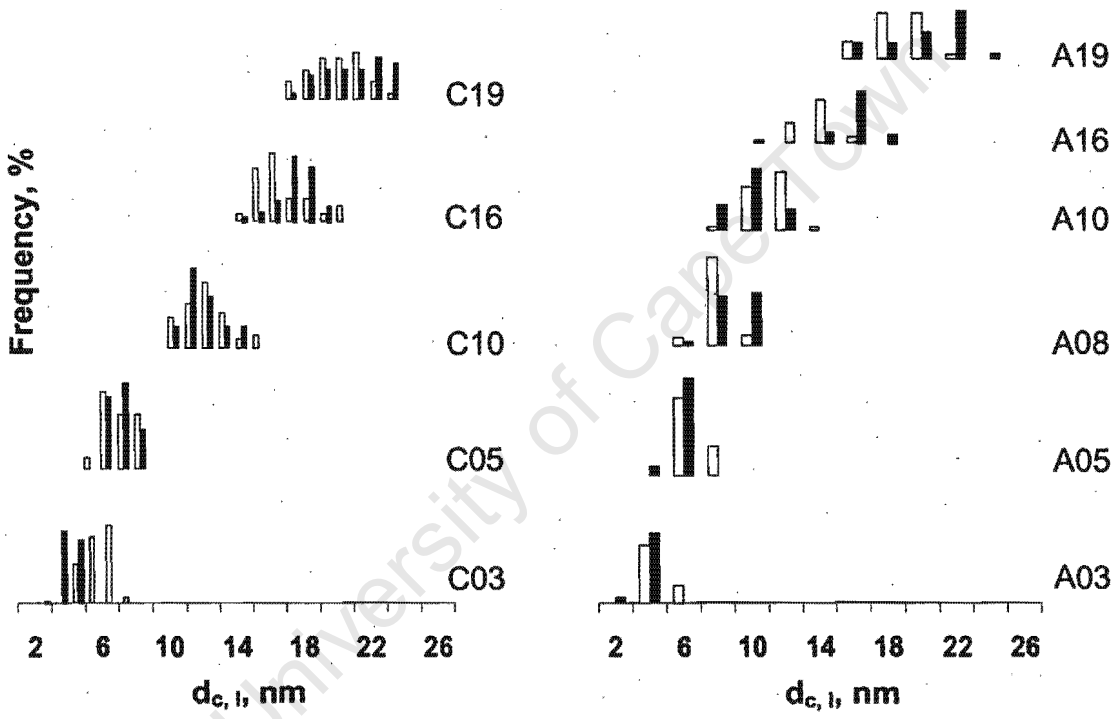

Figure 5.13: Crystallite size distributions ($d_{c,l-TEM}$) of fresh (open bars) and reduced (closed bars) supported catalyst as determined by means of TEM analysis; *left*: carbon supported catalysts; *right*: alumina supported catalysts

The pronounced size trend, increase with increasing water-to-surfactant ratio, however still remains in the catalysts of both samples and more importantly crystallite sizes and distributions did not change much upon the reductive pretreatment. This indicates that severe sintering during reduction did not occur. Ideally, reduced crystallites were expected to be smaller than those in fresh catalysts due to change

in density according to the equation: $d_{Fe} = 0.77 d_{Fe_2O_3}$. The slightly larger sizes obtained can possibly be explained by sintering of small crystallites to thermodynamically more stable sizes. Note that the Hüttig temperature of metallic iron (269 °C) has indeed been exceeded during the catalyst pretreatment, so that some mobility of surface atoms in particular those in small crystallites can occur.

Table 5.6: A summary of TEM characterisation results of supported catalysts

Sample Code	Fresh catalyst $\overline{d}_{c,l} \pm \sigma$, nm	Reduced catalyst $\overline{d}_{c,l} \pm \sigma$, nm
C03	5.7 ± 0.7	3.0 ± 0.5
C05	6.3 ± 0.9	5.3 ± 0.5
C10	11.5 ± 1.3	10.2 ± 0.8
C16	14.9 ± 1.9	15.6 ± 1.2
C19	19.1 ± 2.5	19.2 ± 1.9
A03	3.7 ± 0.5	3.0 ± 0.6
A05	4.7 ± 0.5	5.0 ± 0.5
A08	7.3 ± 0.9	7.9 ± 1.1
A10	10.0 ± 1.0	9.0 ± 1.5
A16	14.5 ± 1.3	15.9 ± 0.9
A19	17.5 ± 1.4	19.2 ± 2.3

5.3.2 XRD analysis of supported crystallites

The TEM-derived crystallite size trends are consistent with peak broadening shown by XRD patterns (see Figure 5.14). Note that XRD analysis was only done on reduced samples. From the TEM micrographs of these samples, many of the crystallites are not seen as single crystals but instead are seen as what appear to be polycrystalline aggregates. XRD patterns of reduced catalyst (Figure 5.14) however confirm crystallite sizes obtained from TEM analyses and therefore the assumption that aggregates were present and not large crystallites.

The XRD patterns of both series (Figure 5.14) showed strong intensity peaks at 44.7° and 65° indicative of a metallic α-iron phase. However, at 35.4° and 62.5°

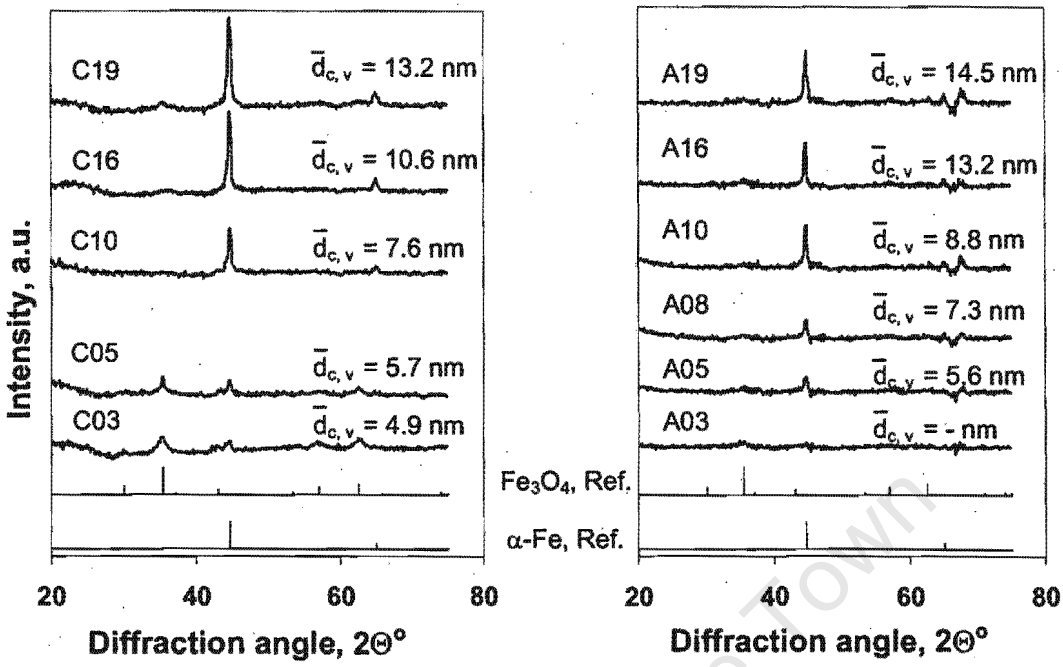

Figure 5.14: X-ray diffraction patterns of reduced supported catalysts; *left*: carbon supported catalysts; *right*: alumina supported catalysts (Note that spectra have been corrected for background due to support)

on most samples, there are peaks which correspond to Fe_3O_4 phase which might be taken as an indication that the degree of reduction for these samples cannot be assumed 100%. Alternatively, the Fe_3O_4 phase might have formed during the passivation procedure. The average sizes of α-iron crystallites determined from the XRD scans using the Debye-Scherrer equation are listed in Figure 5.14 and Table 5.7.

5.3.3 Reduction behaviour and degree of reduction of supported crystallites

The reduction behaviour of the supported catalysts (Figure 5.15) was characterised by means of TPR analysis. TPR profiles of carbon supported crystallites of different size are generally hampered by gasification of the support material under the influence of hydrogen. Whereas a major peak was observed at around 600 °C, comparable

to the reduction of unsupported crystallites (see section 5.2.3), the low temperature peak could not be seen clearly. The big reduction peak in sample A19, with the largest crystallites of the alumina series, is also found in the temperature range 550-600 °C, and all catalysts of this series show the presence of low temperature peaks. However, in this series there was a slight shift of the major reduction peak towards lower reduction temperatures with decreasing crystallite size. Furthermore, a broad high temperature peak could be seen increasing in intensity with decreasing crystallite size possibly indicating strong metal-support interaction. These high temperature peaks have for example also been observed by Ren-Yuan et al. (1987) in temperature programmed reduction of impregnated alumina supported iron catalysts and they have been attributed to the formation of difficult to reduce iron aluminates ($FeAl_2O_4$ and $FeAlO_3$) as evidenced by Mössbauer spectroscopy.

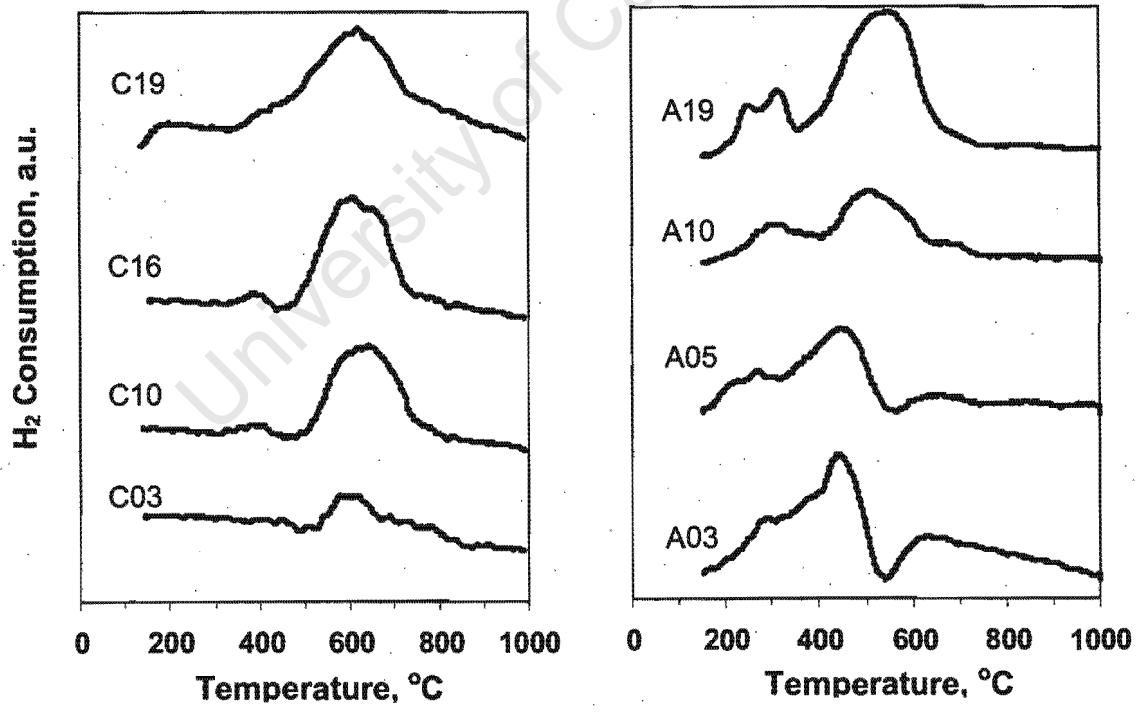

Figure 5.15: TPR patterns of supported catalysts; *left*: carbon supported catalysts; *right*: alumina supported catalysts

It can therefore be expected that the degree of reduction of the alumina supported catalysts with the small crystallites would be lower after the hydrogen pretreatment as applied prior to Fischer-Tropsch experiments (i.e. reduction in pure hydrogen at 350°C for 16 hrs). To determine the degree of reduction of the catalysts of the alumina series samples, TPR analysis of the samples, which had been pre-reduced in the TPR set up at conditions identical to the pretreatment conditions applied in synthesis runs, were conducted. The hydrogen consumption obtained in these experiments were then used to calculate the degrees of reduction. The so obtained degree of reduction varied between 67 % to 85 % and was indeed lower in the samples with small crystallites (see Table 5.7). This method could not be applied on the carbon supported material (see above) and the degree of reduction of these catalysts could therefore not be determined. Based on the similarity of the position of the major reduction peaks in the carbon series and assuming very weak or no interaction of the metal with this support material, the same degrees of reduction as obtained with catalyst A19, i.e. 85 %, was assumed for all samples of the carbon series for the interpretation of data in this thesis.

5.3.4 Further characterisation of the supported catalysts

Attempts to measure the metal surface area in reduced catalysts via H_2 and CO chemisorption (Micromeritics ASAP2000, Micromeritics Instruments, USA) were not successful as linear increases in gas uptake with increasing pressure were observed indicating weak adsorption, which does not allow the determination of metal surface area. Specific metal surface areas per gram of catalyst were therefore determined from the degree of reduction, the actual iron loading and the average crystallite sizes obtained from TEM analysis of reduced model catalysts (for results see Table 5.7).

The effective removal of the surfactant from the catalyst before an experimental run is of crucial importance as the surfactant, if not removed efficiently, might hinder access of active catalytic sites and therefore impact on measured catalyst activities.

Although much effort was undertaken to remove the surfactant during the precipitation steps via excessive and repetitive washing steps with acetone, and subsequent calcination, it was not clear whether surfactant or decomposition products thereof were still present on the catalyst. For this reason ampoule samples of the "product" gas during the reductive in-situ pretreatment before a Fischer-Tropsch reaction were taken and analysed for volatile organic matter that would be released during such a treatment. At initial stages of the reduction at 350 °C indeed small amounts of unidentified organic products were found, after 16 hrs of reduction at this temperature however, no such products could be detected anymore which is why it was assumed that no carbonaceous material was present on the freshly reduced crystallites of the catalysts.

5.3.5 Summary of characterisation results of supported catalysts and conclusions

Although the homogeneity of crystallites as distributed over the support material used could still be improved, and a large loss of iron occurred with the preparation technique applied, a series of well defined supported model catalysts with different crystallite sizes have been prepared successfully. Table 5.7 summaries characterisation results of the supported catalysts. The morphology of the crystallites on these catalysts, compared to the corresponding oxidic and unsupported crystallites, remains largely unchanged upon reductive pretreatment. The freshly reduced catalysts, the properties of which are now well known, are therefore ideally suited for the anticipated Fischer-Tropsch experiments. The average crystallite sizes obtained from TEM analysis of reduced catalysts was used for interpretations of possible size effects obtained in the initial stages of a Fischer-Tropsch experiment.

Table 5.7: A summary of characterisation results of supported catalysts used for activity studies

Sample Code	Fe loading[a]	XRD[b]	TEM[c]		Red.[d]	$S_{g,Fe}$[e]
	wt%	$\overline{d}_{c,v}$, nm	$\overline{d}_{c,l} \pm \sigma$, nm	$\overline{d}_{c,v} \pm \sigma$, nm	%	m^2/g
C03	2.9	4.9	3.0 ± 0.5	3.1 ± 0.5	85[f]	6.272
C05	2.8	5.7	5.3 ± 0.5	5.5 ± 0.7	85	3.428
C10	4.5	7.6	9.8 ± 0.8	10.1 ± 1.1	85	2.966
C16	4.6	10.6	15.6 ± 1.2	16.0 ± 1.2	85	1.913
C19	4.7	13.2	19.2 ± 1.9	19.6 ± 1.9	85	1.602
A03	4.6	-	3.0 ± 0.6	3.3 ± 0.7	69	8.164
A05	4.7	5.6	5.0 ± 0.5	5.1 ± 0.5	67	4.736
A08	4.9	7.3	7.9 ± 1.1	8.2 ± 1.1	72	3.409
A10	5.2	8.8	9.0 ± 1.5	9.7 ± 1.6	75	3.308
A16	5.3	13.2	15.9 ± 0.9	16.0 ± 0.9	84	2.137
A19	5.6	14.5	19.2 ± 2.3	19.9 ± 2.3	85	1.892

[a]as determined by SEM-EDX analysis
[b]referring to reduced catalyst
[c]referring to reduced catalyst
[d]degree of reduction
[e]specific metal surface area per gram of catalyst, determined using actual iron loading, crystallite size from TEM analysis ($\overline{d}_{c,l}$) and degree of reduction
[f]estimated (see section 5.3.3)

5.4 Development of Fischer-Tropsch activity

The catalytic performance for both carbon and alumina supported catalysts were tested in a fixed bed reactor with 0.5 g of catalyst of the carbon series loaded and 0.2 g of catalyst of the alumina series loaded. Prior to Fischer-Tropsch synthesis runs catalysts were activated following the same reduction as previously listed (in hydrogen at 350 °C for 16 hrs). All tests were run for 5 days (except catalyst C10) at a reaction temperature of 270 °C, a total pressure of 30 bar(a) and constant synthesis gas flow with a hydrogen to carbon monoxide ratio of 2.0. Some of the reported data for specific reaction times are listed in Tables F.1-F.4 in Appendix F. Note that catalyst sample A14 was not tested in Fischer-Tropsch experiments.

The catalyst activity as expressed as CO conversion was monitored as a function of time on stream. Steady state CO conversion was between 40 % and 60 % for the carbon series (Figure 5.16 (top)). Lower conversion was found with the alumina supported catalysts, steady state CO conversions below 15 % (Figure 5.16 (bottom)), due to the smaller amount of catalyst loaded.

Generally, over the crystallite size range investigated, catalyst deactivation was observed with time on stream, some of the carbon supported catalysts even showed a temporary increase of activity which might be due to changes in catalyst composition and morphology under the influence of the reactants CO and H_2 and products H_2O and CO_2, a behaviour of iron catalysts previously also described by Schulz et al. (1999) and Pichler (1952). If iron crystallites show the same activity regardless of crystallite size then the catalysts with small crystallites (highest metal surface area) would show the highest CO conversion at least in the initial stages before the catalysts undergo any phase changes. It can clearly be seen from Figure 5.16 that this was not the case indicative of influence of crystallite size on the Fischer-Tropsch activity.

In order to distinguish between the effect of changing metal area loaded and the

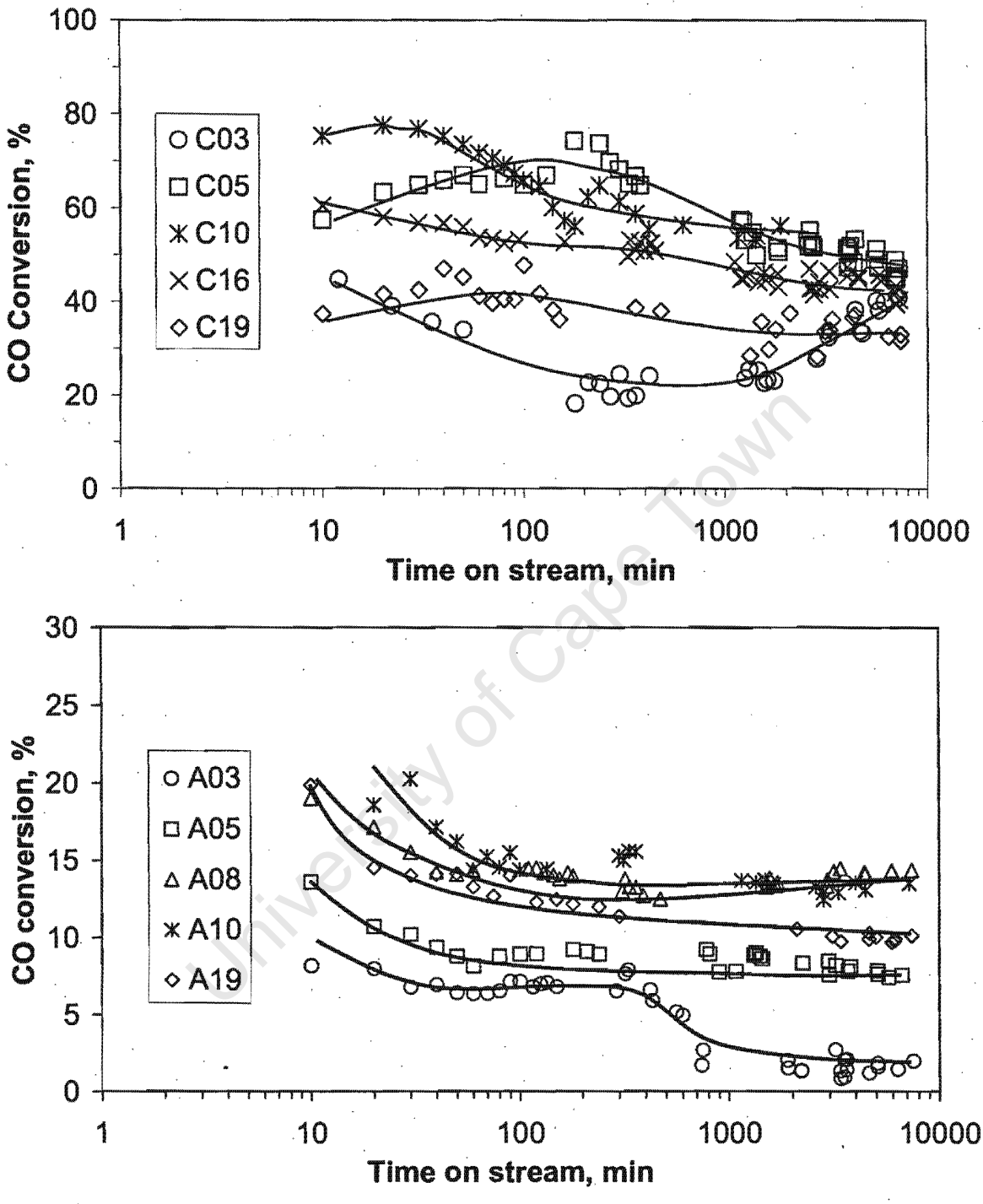

Figure 5.16: Changes in CO conversion in the Fischer-Tropsch synthesis as a function of time on stream for Fe/C (*top*) and Fe/Al_3O_3 (*bottom*) catalysts with different crystallite sizes prepared via precipitation in water-in-oil microemulsions

specific effect of crystallite size the integral rate of formation of Fischer-Tropsch products (i.e. excluding the CO which is consumed for the formation of CO_2) normalised for the amount of metal surface present after pre-treatment was plotted as function of time on stream (Figure 5.17)[8]. The actual metal surface area ($S_{g,Fe}$) was estimated based on the TEM measurements of reduced and passivated catalyst samples taking the degree of reduction as well as actual metal loading into consideration (see Table 5.7). Note that the degree of reduction of the catalysts of the carbon series are estimated values (see section 5.3.3). This metal area specific integral rate is equivalent to a turnover frequency and should be independent of crystallite size. However, on both the carbon and alumina series, one can clearly observe that catalysts with small crystallites showed lower metal area specific integral Fischer-Tropsch activities than catalysts with large crystallites (Figure 5.17).

A plot of the initial integral Fischer-Tropsch rate versus crystallite size should be most representative of the exact crystallite size present just before the reaction as determined by TEM of reduced and passivated catalysts. Average initial activity (30-100 min average) shown in Figure 5.18 confirms that small crystallites were indeed less active, whereas crystallites larger than around 7 nm seem to have the same specific activity. This finding still holds true if one assumes that small crystallites of the carbon series could, contrary to the assumption made earlier, had 3 fold lower degree of reduction than larger crystallites (i.e. 30 % opposed to 85 %). This trend was clearly obtained with both series of catalysts tested, the alumina supported catalyst displaying a somewhat lower activity.

TEM analyses conducted on three spent samples of the alumina series (i.e. after five days time on stream) indicate severe sintering as much larger crystallites were found particularly in the water rich exit zone of the catalyst bed (Figure 5.19). Some sintering due to mobility of surface atoms can indeed be expected seeing that the reaction temperature (270 °C) coincides with the Hüttig temperature for iron (269

[8]Note that this rate is to be considered a nominal rate as the crystallite size and therefore the initial surface area might change during the Fischer-Tropsch experiment

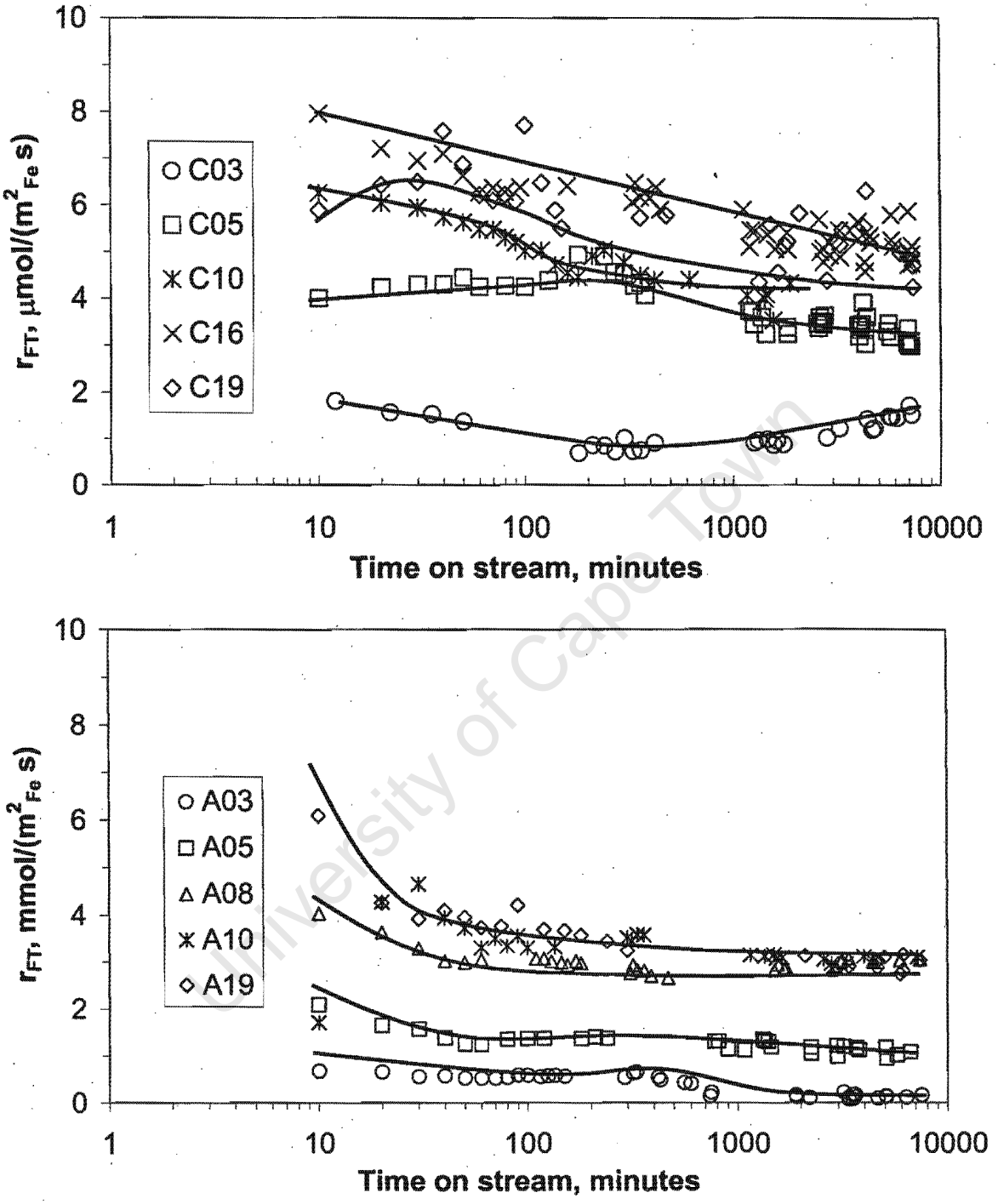

Figure 5.17: Metal area specific integral formation rate of Fischer-Tropsch products, r_{FT}, as a function of time on stream for Fe/C (*top*) and Fe/Al_3O_3 (*bottom*) catalysts with different crystallite sizes prepared via precipitation in water-in-oil microemulsions

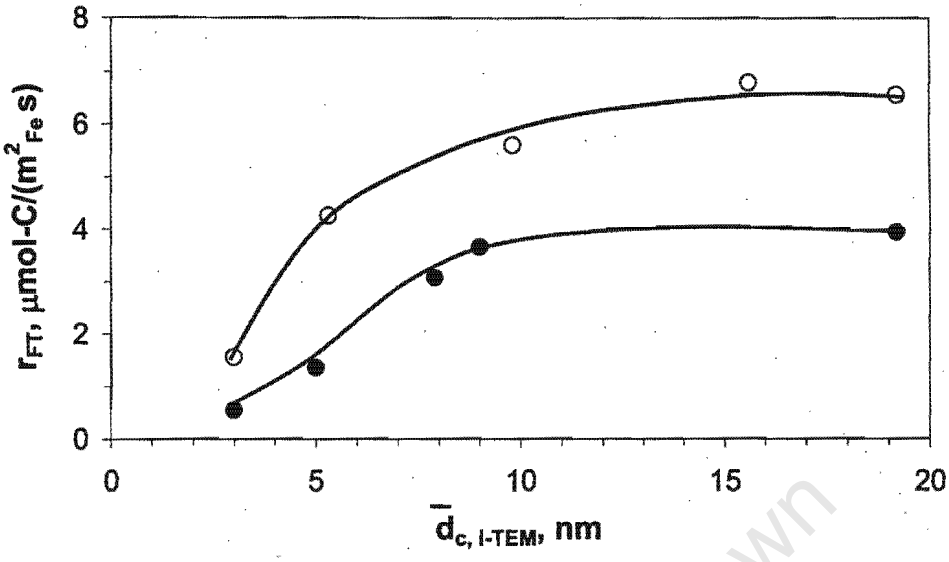

Figure 5.18: Average initial (30-100 min) metal area specific formation rate of Fischer-Tropsch product versus average iron crystallite size ($\bar{d}_{c,l-TEM}$) in reduced catalysts for Fe/C (○) and Fe/Al_2O_3 (●) catalysts prepared via precipitation in water-in-oil microemulsions.

°C). It should be noted that due to the very small amount of spent catalyst samples no XRD analyses could be conducted to confirm the crystallite sizes determined by TEM analysis. It is suspected that some of the "crystallites" evaluated might in fact be clusters of smaller entities. It is however highly unlikely that sintering and corresponding loss in surface area plays a role in the very initial stages of the experiments.

Oxidation of crystallites in Fischer-Tropsch catalysts under reaction conditions can account for loss in activity as the metal oxides are generally considered to be inactive or at least less reactive (Mansker et al., 1999; Bian et al., 2002; Li et al., 2002). Magnetite is often found in working and spent iron catalysts. The fresh catalyst used in this work mainly contained α-iron prior to exposure to synthesis gas at reaction conditions. Both, the formation of magnetite and iron carbides (e.g. Fe_3C) from iron are thermodynamically feasible at Fischer-Tropsch reaction conditions

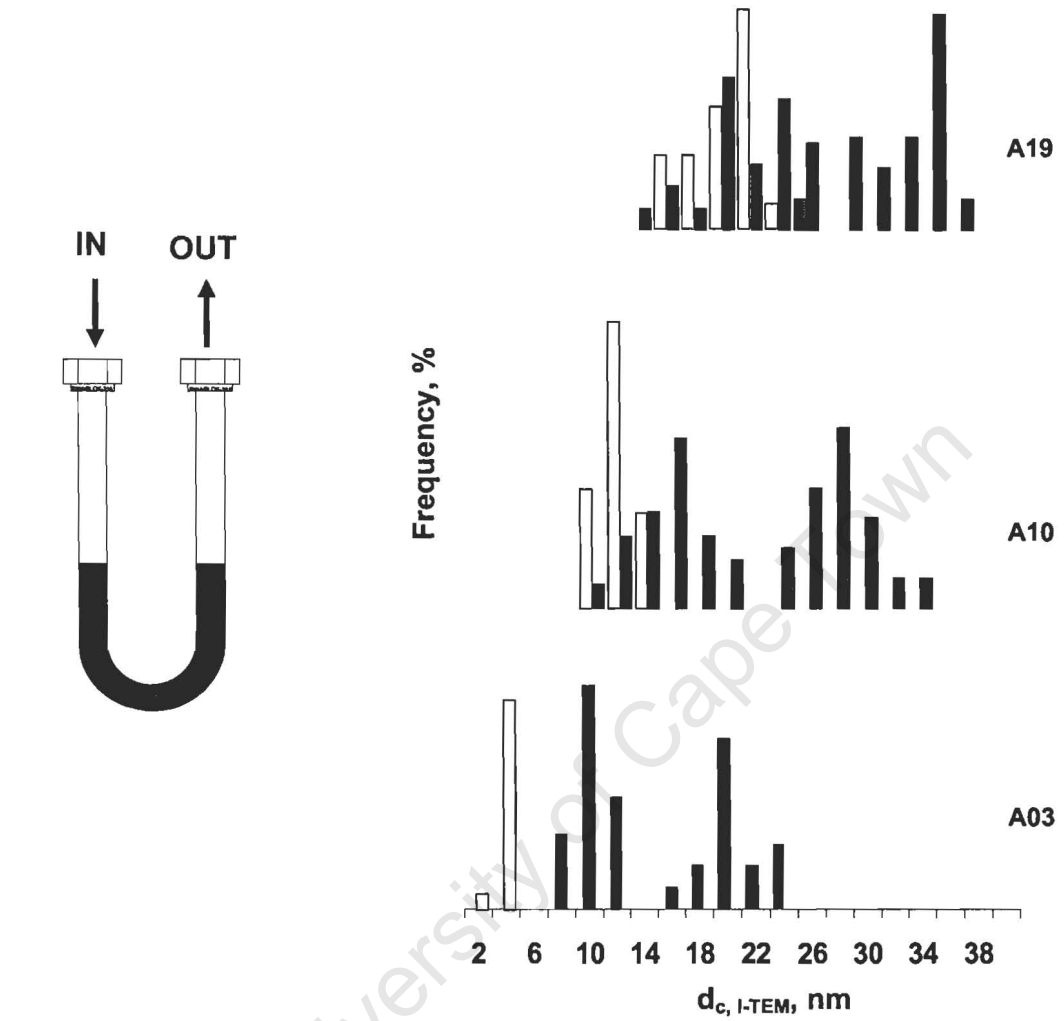

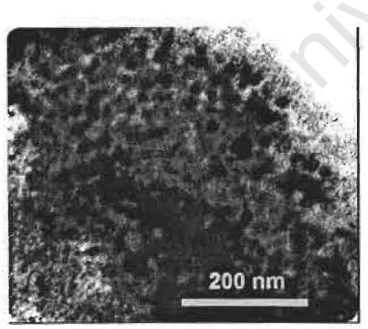

(c) A03-outlet

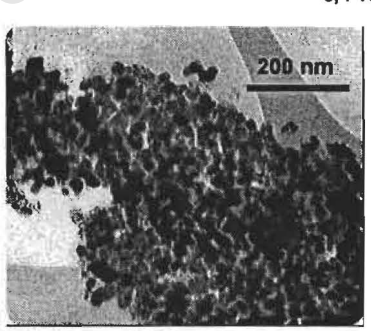

(d) A10-outlet

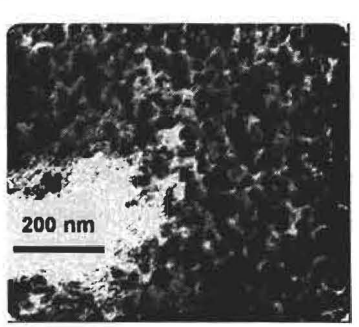

(e) A19-outlet

Figure 5.19: Crystallite size distribution of fresh (open bars) and spent catalysts of alumina series (inlet: black bars, outlet: grey bars) after 5 days time on stream and corresponding TEM micrographs of spent catalysts from the outlet side.

(Anderson, 1984):

$$3Fe + 4H_2O \rightleftharpoons Fe_3O_4 + 4H_2 \qquad K_p(270°C) = 31 \tag{5.10}$$

$$3Fe + 2CO \rightleftharpoons Fe_3C + CO_2 \qquad K_p(270°C) = 1.1x10^7 \text{ bar}^{-1} \tag{5.11}$$

Of these two reactions the formation of iron carbides seems to be thermodynamically and kinetically favoured seeing that the formation of magnetite requires product water, whereas the CO which is required to form carbides, is already present in the synthesis gas. It might therefore be assumed that initially iron carbides formed rapidly, while largely maintaining the crystallite size of the α-iron crystallites they originated from. A further transformation of the carbide phase under the influence of products of the synthesis could proceed via the following reactions:

$$Fe_3C + 5H_2O \rightleftharpoons Fe_3O_4 + 5H_2 + CO \qquad K_{PI,eq}(270°C) = 85 \text{ bar} \tag{5.12}$$

$$Fe_3C + 4H_2O + CO_2 \rightleftharpoons Fe_3O_4 + 4H_2 + 2CO \qquad K_{PII,eq}(270°C) = 1.4 \text{ bar} \tag{5.13}$$

(Calculated using data from Lide and Kehiaian (1994)). Thermodynamically, the oxidation of bulk Fe_3C yielding Fe_3O_4 at 270 °C is only feasible if the actual K_p values are smaller than the equilibrium constants:

$$\frac{p_{CO}p_{H_2}^5}{p_{H_2O}^5} < K_{PI,eq}(270°C) = 85 \text{ bar}$$

$$\frac{p_{CO}^2p_{H_2}^4}{p_{CO_2}p_{H_2O}^4} < K_{PII,eq}(270°C) = 1.4 \text{ bar}$$

These conditions were however not obtained in the experiments even at the reactor outlet (see Table 5.8) implying that according to bulk thermodynamics the reoxidation of Fe_3C yielding Fe_3O_4 is not feasible under these conditions. Note that the same considerations would hold true for other possible iron carbides.

Due to their high surface energies, thermodynamically, the oxidation of nanosized iron carbide should be much more feasible than oxidation of bulk iron carbide in

Table 5.8: Actual equilibrium pressure constant, K_{PI} and K_{PII} (calculated using exit partial pressures listed in Table F.2 in Appendix F), after 60 min time on stream in Fischer-Tropsch experiments with Fe/C and Fe/Al_3O_3 catalysts prepared via precipitation in water-in-oil microemulsions

Sample Code	K_{PI}	K_{PII}
C03	$29x10^5$	$72x10^5$
C05	$14x10^2$	$11x10^2$
C10	$39x10^1$	$26x10^1$
C16	$12x10^3$	$90x10^2$
C19	$12x10^3$	$26x10^3$
A03	$38x10^7$	na[a]
A05	$76x10^7$	$50x10^8$
A08	$30x10^5$	na
A10	$70x10^5$	na
A19	$15x10^7$	$22x10^7$

[a]no CO_2 formation detected

analogy to the oxidation of nanosized cobalt crystallites under Fischer-Tropsch conditions (van Steen et al., 2005). This implies that when the crystallite size decreases, the equilibrium lines shift upwards in the graphs depicted in Figure 5.20 therefore increasing the transformation equilibrium constant at a given temperature.

Although not proving it, the above consideration supports the idea that formation of Fe_3O_4 from nanosized iron carbide might be the cause for lower activity of the small crystallites. Only an *in situ* characterisation of the working catalyst or e.g. XRD analyses of spent catalyst tested in the very short runs (<60 min) might clarify this finding. Oxidation of small cobalt crystallites (<5-6 nm) by product water has been stated to occur by Iglesia (1997) and a thermodynamic analysis support this possibility (van Steen et al., 2005). Although some experimental evidence seems to indicate that a reoxidation of very small cobalt crystallites can really occur (Hilmen et al., 1999; Jacobs et al., 2004) a definite experimental proof for this deactivation mechanism of cobalt is also still outstanding.

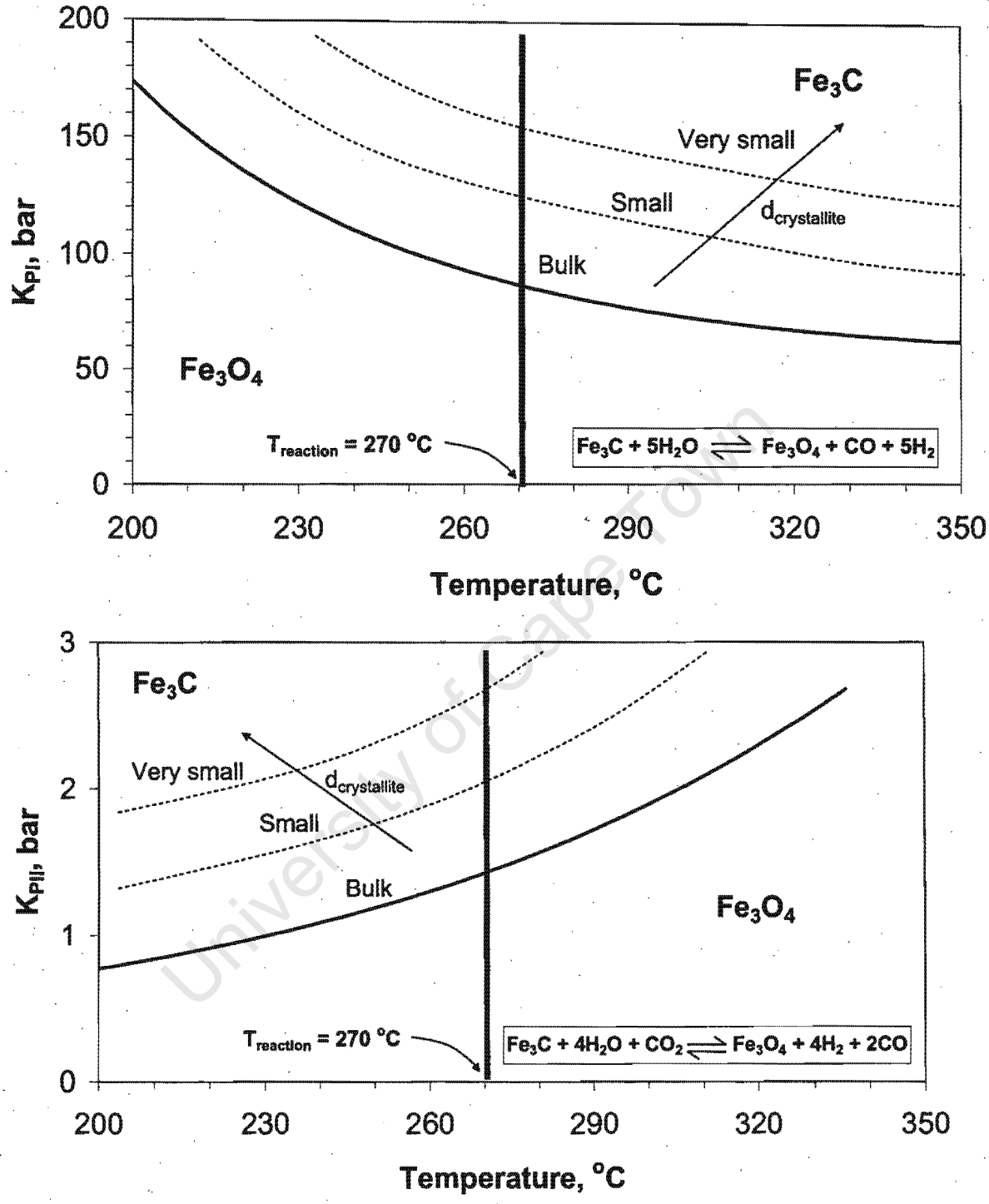

Figure 5.20: Possible effect of crystallite size on thermodynamics of iron carbide transformation to the oxide phase during Fischer-Tropsch synthesis

The catalyst activity of iron based Fischer-Tropsch catalysts can also be affected by alkali promotion. Typically an increase of up to 50 % in Fischer-Tropsch activity can be obtained upon optimal alkali promotion (Dry, 1981, 2004b). Equal amounts of potassium as chemical promotors were added to the model catalyst of this work. However, assuming ideal distribution of potassium on the support, the ratio of potassium per iron metal surface increases with increasing iron crystallite size. A slightly improved promoting effect could therefore be expected in the catalyst with the larger crystallites. This can however not account for the almost 10 fold difference of the activities obtained with the catalysts of varying crystallite sizes. On some alumina supported iron catalysts even a decrease of activity has been reported due to potassium promotion (Dry, 2004b), this might explain the lower activity of the catalysts of the alumina series in this study.

It has also been suggested that the rate of CO dissociation might depend on the crystallite structure or size and CO dissociation would only take place on two well separated sites to accommodate the separated carbon and oxygen atoms (Sachtler and Ichikawa, 1986; de Koster and van Santen, 1991; Ojeda et al., 2004; Phala, 2004). However, the overall rate of the Fischer-Tropsch reaction is governed by product desorption rather than CO dissociation (van Steen and Schulz, 1999). Assuming CO dissociation to be the rate determining step of Fischer-Tropsch synthesis would imply all other steps to be in equilibrium, the equilibrium composition of a Fischer-Tropsch product, however, would contain more than 99 C-% methane (Anderson, 1984). It is the specific inhibition of product desorption, which is so unique about Fischer-Tropsch synthesis and which makes chain growth possible (Schulz et al., 1995). The formation of Fischer-Tropsch product and the chain growth events, may however require certain arrangements of surface atoms and it is currently not known which these are.

Rainer et al. (1996) have reported preferred carbon build up on smaller crystallites of palladium when studying CO adsorption. This was explained by a higher sus-

ceptibility to carbon poisoning of low coordination edge/defect sites as present in small crystallites in high densities. Although this effect could explain the observed crystallite dependent activity trends, it is not clear if this observation is applicable in a hydrogen rich atmosphere as in Fischer-Tropsch synthesis.

The above experimental findings cannot be explained conclusively. Currently reoxidation of small nanosized iron carbides seem to be the most likely cause for the much lower activity of crystallites smaller than around 7-8 nm. In any case the finding is of utmost importance when aiming at maximum metal utilization in supported iron catalysts for Fischer-Tropsch synthesis.

5.5 Product formation

Detailed selected activity and selectivity results at selected times on stream (from initial to steady state times) for catalytic experiments conducted can be found in Appendix F. For easy and concurrent readability of this section, the reader is referred to Table F.2, a fold-out summary of selected results on the effect of crystallite size after 60 minutes time-on-stream which also includes some of the activity data. The data obtained at this reaction time are believed to be most representative for effects of crystallite size as at longer reaction times sintering might have occurred; reaction times much lower than 60 min do not allow for evaluation of a complete product spectrum.

Temporal changes of CO_2 selectivity are also reported as function of time on stream, as CO_2 was analysed using the on-line gas chromatograph. Product selectivity can be affected by many factors, and effects due to crystallite size might be masked by:

- conversion effects, as high conversion or resulting long residence time might favor consecutive reactions (note: this effect should be negligible in the test with the catalysts of the alumina series where conversion was below about 15

%);

- effects of potassium promotion; constant potassium to iron ratios were used in the catalysts, but the potassium per iron metal surface area effectively increases with increasing iron crystallite size, therefore possibly leading to enhanced promotion effects in catalysts with large crystallites.

5.5.1 CO_2 formation

CO_2 is a product which is always found in iron based Fischer-Tropsch synthesis. It is mainly formed via the water-gas shift reaction, in which product water reacts in a consecutive reaction with carbon monoxide to form CO_2 and hydrogen (see Equation 2.2 in literature review section). Some of it can also be formed via the Boudouard dispropotionation of CO. Figure 5.21 shows CO_2 selectivity obtained in the runs with carbon supported crystallites as function of time on stream.

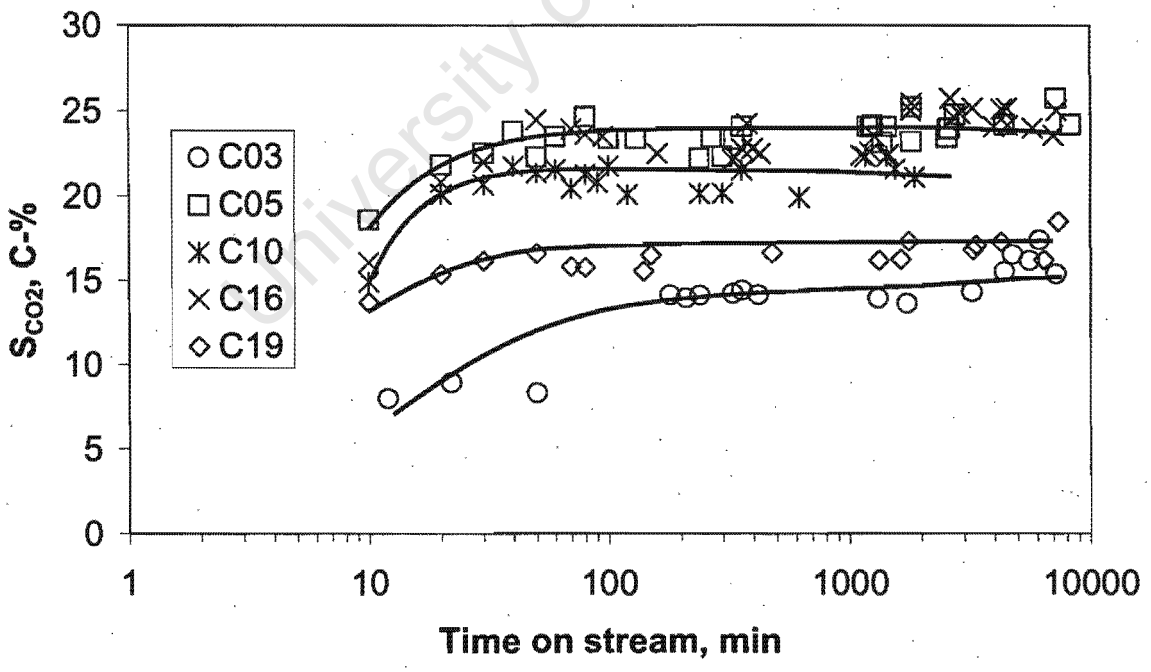

Figure 5.21: CO_2 selectivity as a function of time on stream for carbon supported catalysts with different crystallite size prepared via precipitation in water-in-oil microemulsions

The low conversion levels in the series with the alumina support (8 % to 15 %) did not allow for accurate analysis of secondarily formed CO_2 (TCD detection limit). In the carbon series almost no temporal changes of CO_2 selectivity were found, except for a slight initial increase in the first 100 minutes, a trend to be expected in a consecutive reaction. These changes may also be attributed to changes of catalyst phases and formation of the working catalyst (Schulz et al., 1990, 1999; Li et al., 2002; Claeys and Schulz, 2004). Water-gas-shift activity has by some researchers (Newsome, 1980; Lox and Froment, 1993; Rao et al., 1995; van der Laan, 1999) been attributed to the presence of magnetite, although it should be noted that magnetite is also used as part of water-gas-shift catalysts, however, only as a carrier without significant catalytic activity (Andreeva et al., 1996; Rhodes et al., 1995). Assuming a preferred oxidation of small crystallites at reaction conditions as hypothesised in this work, high CO_2 selectivity would be expected in the catalyst with the small crystallites. This was, however, not found. The low CO_2 selectivities found in the experiments with the smallest and the largest crystallites are believed to be due to the relatively low conversion levels in these two experiments, 18 % to 42 %, compared to 54 % to 65 % (initial conversion) in the other experiments of the series in the carbon series. Possible effects of potassium promotion in catalysts with large crystallites are not evident (potassium is known to increase CO_2 selectivity). In conclusion, there is no clear indication that crystallite size effects account for changes in CO_2 selectivity.

5.5.2 Formation of organic products

Selectivities reported below are product contents (in C-%) in the fraction of volatile organic compounds as directly obtained from FID analysis. Note that no visual formation of wax was observed in all experiments as chain growth probabilities were very low (i.e. below 60 %, see also section 5.5.2.2), more than 90 % (carbon basis) of the product are volatile and thus the reported selectivities are a good representation of the total product.

5.5.2.1 Methane formation

Methane is the thermodynamically most favoured product of Fischer-Tropsch synthesis (Anderson, 1984). It is formed via associative desorption of a methyl species and surface hydrogen.

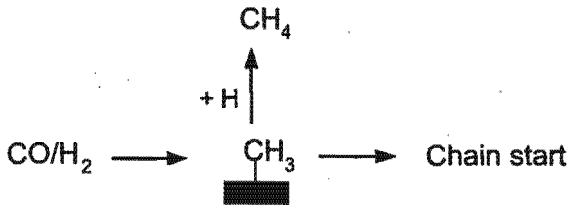

Alternatively the methyl species can act as a chain starter. The inhibition of methane formation is an essential feature of Fischer-Tropsch synthesis (Schulz, 2003). The methane selectivities obtained in the runs with the model catalysts at 60 min time on stream are shown in Figure 5.22. In both series a decline of methane selectivity with increasing crystallite size has been obtained. This can be explained by enhanced effects of potassium (increased potassium to metal surface area), which is known to suppress methane formation (Dry, 1981, 2004b), or it might be due to effects of crystallites size.

Increasing methane selectivities have been reported in CO hydrogenation for rhodium catalysts with decreasing crystallite size (Ojeda et al., 2004). This was attributed to structure sensitivity as in small crystallites the density of ensembles of rhodium atoms needed for chain growth would be lower than in large crystallites. In other words, methane formation might occur on sites different from chain growth sites (Schulz and Nehren, 1986; Schulz et al., 1995; Schulz, 2003) and these sites might be present in higher densities on small crystallites.

From an economic point of view methane selectivity in a Fischer-Tropsch process is to be kept as low as possible; in commercial processes methane selectivities of 4 C-% in low temperature Fischer-Tropsch synthesis and 8 C-% in high tempera-

ture Fischer-Tropsch synthesis are obtained (Dry, 2004a). The methane selectivities obtained in this work, in particular those of the catalysts of the carbon series, are fairly high due to non optimal promotion. However, the trends observed, if not solely due to effects of potassium promotion, would be of utmost importance for design of catalysts.

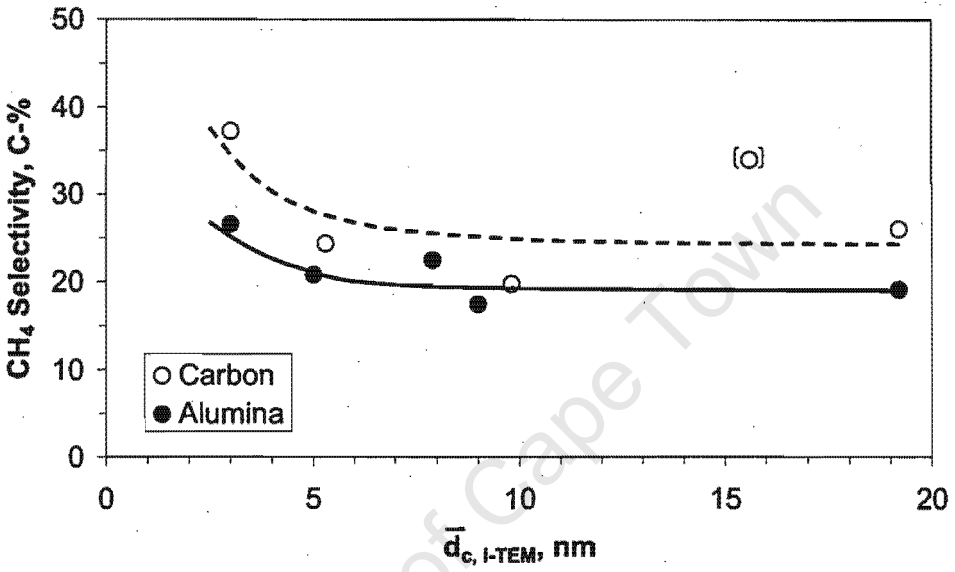

Figure 5.22: Methane selectivity in Fischer-Tropsch synthesis after 60 min time on stream as a function of average iron crystallite size (TEM) in reduced catalyst for Fe/C (○) and Fe/Al_2O_3 (●) catalysts prepared via precipitation in water-in-oil microemulsions

5.5.2.2 Chain growth

Inhibition of product desorption is the essential feature of Fischer-Tropsch synthesis (Schulz et al., 1995; Schulz, 2003) allowing for chain growth:

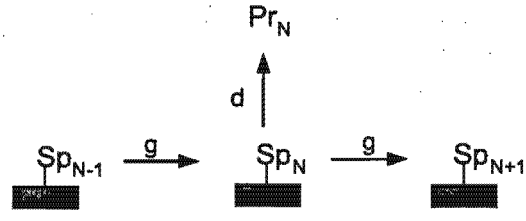

Assuming carbon number independence, the growth probability p_g of a growing chain can be derived from slopes of the so called Anderson-Schulz-Flory distributions (logarithmic plot of mole fractions of linear hydrocarbons versus carbon number):

$$\lg(x_N) = N\lg(p_g) + \lg\left(\frac{1-p_g}{p_g}\right) \tag{5.14}$$

The logarithmic molar product distributions of the linear product hydrocarbons versus carbon number obtained at 60 min time on stream for the two series conducted is shown in Figure 5.23.

All curves show often obtained deviations from ideal distributions with relatively high values at C_1, relatively low values at C_2 and a slight curvature with increasing carbon number. These deviations are generally attributed to secondary reactions of olefins (see also section 5.5.2.3). Chain growth probabilities were derived via linear regression from the linear part of the distribution in the carbon number range C_3 to C_7; these values are plotted in Figure 5.24 as function of iron crystallite size in the reduced catalysts.

The obtained chain growth probabilities in this carbon number range were very low, between 49 and 55 %. Note that higher growth probabilities of up to 70 % were found in the carbon number range C_{10} to C_{14} (see Table F.2 and Appendix F). With increasing crystallite size a slight increase of the chain growth probability is observed, the growth probabilities in the alumina series being somewhat larger than those in the carbon series. This observation is even more pronounced in the early stages of the synthesis experiments (see Table F.1 in Appendix F). This trend is to be expected opposite to that of methane formation (see previous section) and it can therefore be explained in the same manner, namely a possible direct effect of crystallite size due to higher density of ensembles of atoms promoting chain growth in larger crystallites and/or an effect of enhanced potassium promotion in large crystallites as potassium is known to promote chain growth in iron based Fischer-

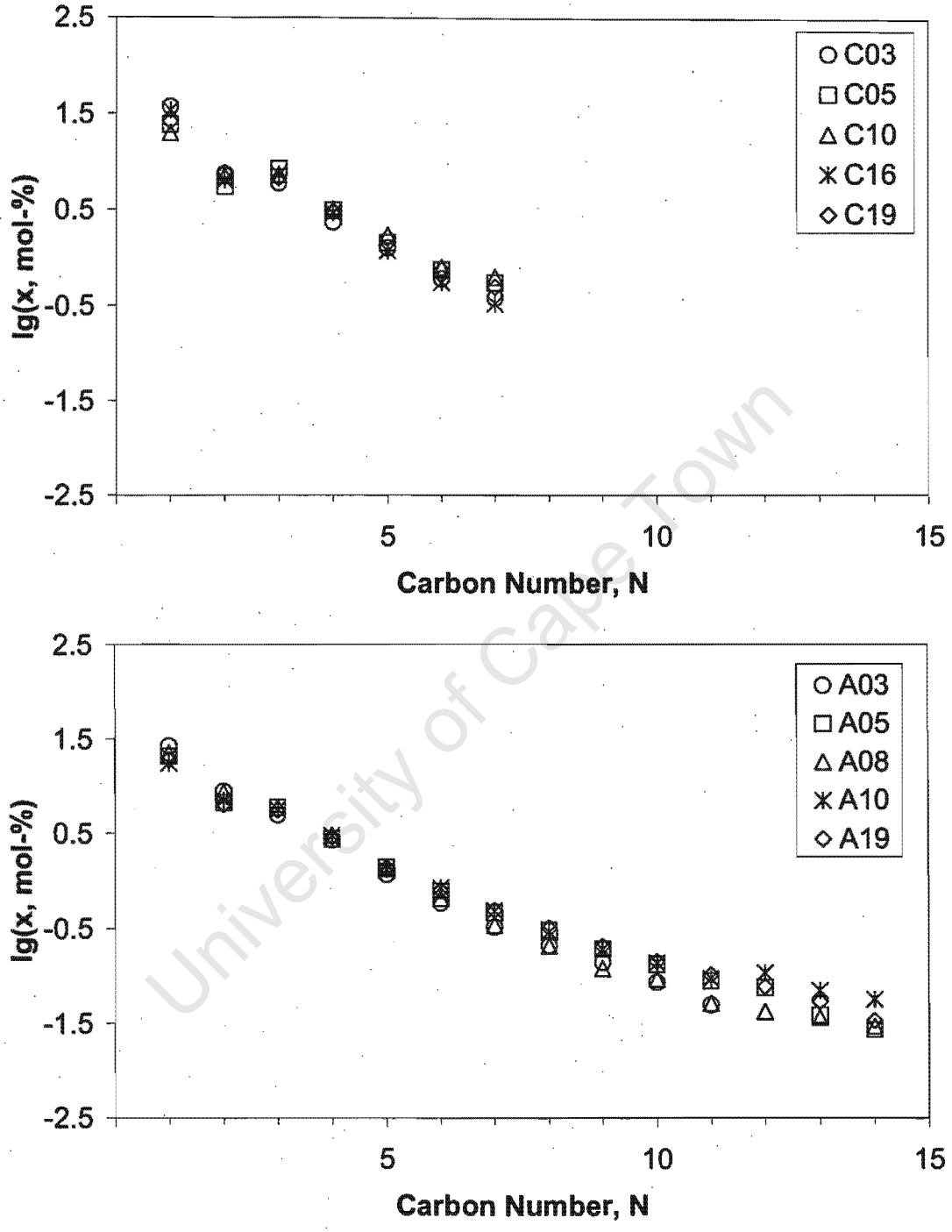

Figure 5.23: Logarithmic molar product distributions of linear hydrocarbons in Fischer-Tropsch synthesis after 60 min time on stream for catalysts Fe/C (*top*) and Fe/Al_2O_3 (*bottom*) with varied crystallite size prepared via precipitation in water-in-oil microemulsions

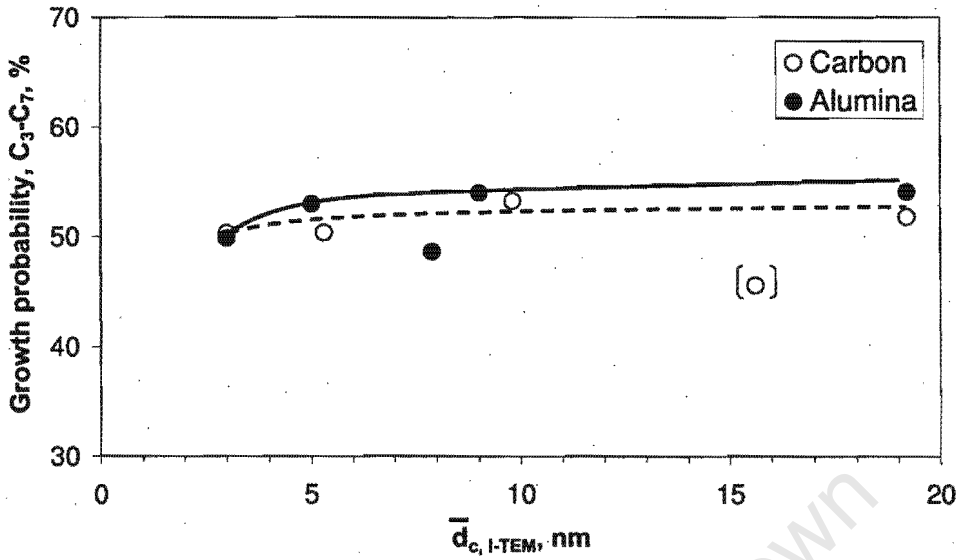

Figure 5.24: Chain growth probabilities (carbon number C_3 - C_7) in Fischer-Tropsch synthesis after 60 min time on stream as function of iron crystallite size (TEM) in reduced catalyst for Fe/C (○) and Fe/Al_2O_3 (●) catalysts prepared via precipitation in water-in-oil microemulsions

Tropsch synthesis (Dry, 1981, 2004b).

5.5.2.3 Olefin formation

Olefins are the main primary organic products of Fischer-Tropsch synthesis (Schulz, 1999). They are formed via dissociative desorption of growing surface alkyl species, alternately a paraffin can be formed via hydrogen addition to the alkyl species (see also Figure 2.6 in the literature review section). The latter reaction is strongly inhibited so that primarily up to 70-90 mol-% olefins are formed in each carbon number of the Fischer-Tropsch product (Schulz and Claeys, 1999). The step of olefin desorption is however reversible as olefins can readsorb and undergo secondary reactions, such as incorporation into growing chains and hydrogenation to the corresponding paraffin. Information on the extent of this secondary olefin conversion can be derived from diagrams showing the olefin content in the fraction of the corresponding linear hydrocarbons as function of carbon number; these plots are shown in Figure

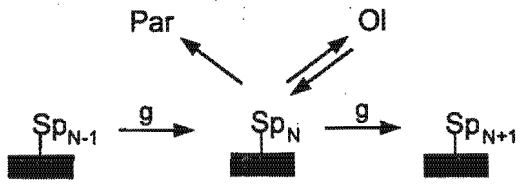

5.25 for the experiments conducted with the two series of model catalysts (60 min time on stream).

In case of primary selectivity, i.e. not affected by secondary reactions, horizontal lines at 70-90 mol-% would be expected. However, all curves show a pattern with relatively low values at C_2 and decreasing olefin contents with increasing carbon number from C_3/C_4 onwards, reflecting preferred secondary conversion of ethene and long chain olefins. Ethene has indeed been shown to be the most reactive olefin (Iglesia et al., 1993; Schulz and Claeys, 1999), and enhanced secondary conversion of long chain olefins has been attributed to effects of chain length dependent diffusivity (Iglesia et al., 1993) and solubility (Kuipers et al., 1995; Schulz and Claeys, 1999). No clear effects of crystallite size on secondary olefin hydrogenation and incorporation can be derived from Figure 5.25, as the data do not vary much within each series. Perhaps olefin contents increase slightly with increasing crystallite size in the alumina series.

It is however important to note that the olefin contents obtained in the series with the carbon supported catalysts are much lower than those obtained with the alumina supported catalysts. It is known that potassium promotion plays a crucial role in forcing back most secondary reactions so that a much more 'primary' product can be obtained in sufficiently potassium promoted iron catalyst (Claeys, 1997; Claeys and Schulz, 2004). The absence of potassium promotion generally leads to a very poor product quality with high methane selectivity, lower chain growth, low olefin contents, large amounts of olefins with internal double bonds and a higher degree of chain branching.

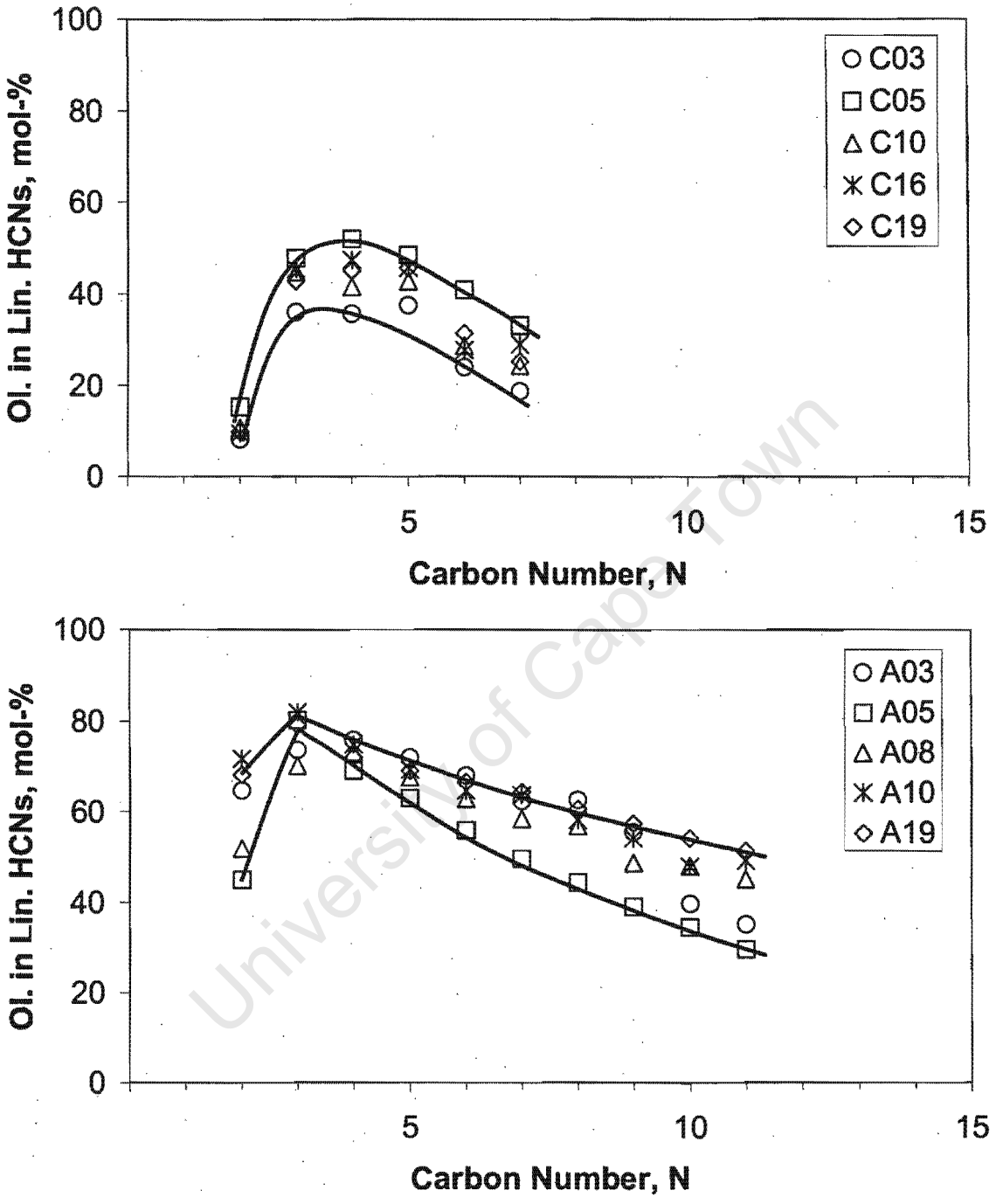

Figure 5.25: Molar content of olefins in corresponding fraction of linear hydrocarbons as function of carbon number in Fischer-Tropsch synthesis after 60 min time on stream for catalysts Fe/C (*top*) and Fe/Al_2O_3 (*bottom*) with varied crystallite size prepared via precipitation in water-in-oil microemulsions

A closer comparative look at chromatograms of the C_5 product fractions obtained on catalyst of the two series (see Figure 5.26) indeed shows how hugely different the composition of products of the two series is. Characteristic features of the composition of the C_5-fraction, which has been chosen as an example representing other carbon number fractions, are also given in Table F.2 in Appendix F; some of these characteristics will only be discussed in the following sections.

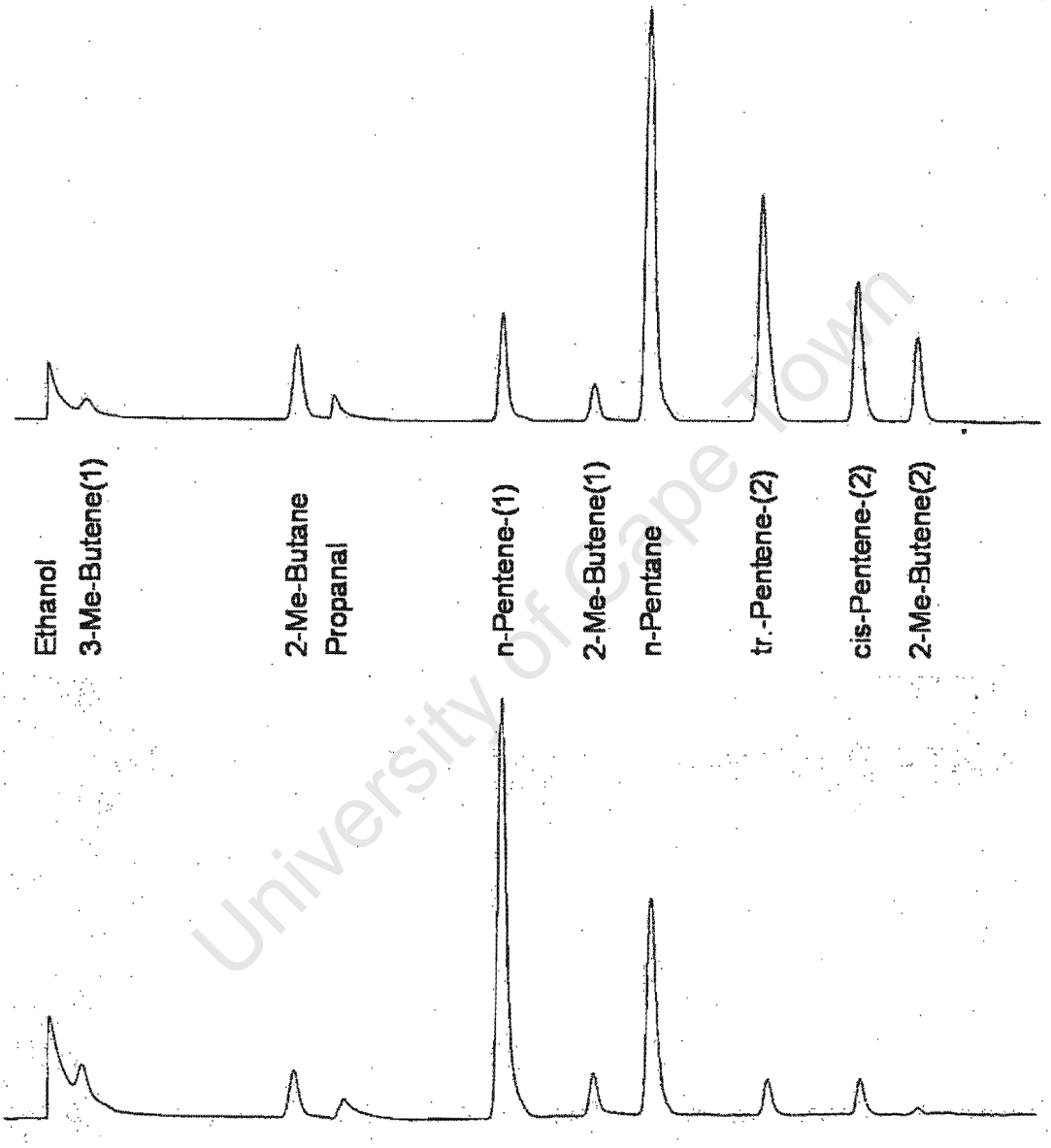

Figure 5.26: GC chromatograms of the C_5 product fraction in Fischer-Tropsch synthesis after 60 min time on stream for catalysts Fe/C (*top*) and Fe/Al_2O_3 (*bottom*) prepared via precipitation in water-in-oil microemulsions

Among the linear olefins within a carbon number fraction, very low contents of α-olefins were found in all catalysts of the carbon series. It is generally believed (Schulz and Claeys, 1999; Claeys and Schulz, 2004) that almost exclusively only α-olefins are formed primarily which can form olefins with internal double bonds after non terminal readsorption to the catalyst surface (see also Figure 2.6).

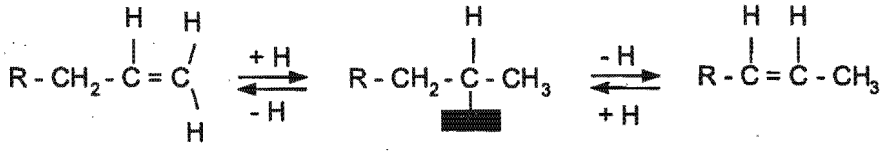

The extent of this secondary isomerisation can be judged from plots showing the α-olefins in the fraction of the linear olefins of the same carbon number as function of carbon number (see Figure 5.27).

The very low α-olefin content obtained in all experiments of the carbon series indicates excessive double bond shift isomerisation, which is characteristic for weakly to non alkali promoted iron catalysts (Claeys, 1997; Claeys and Schulz, 2004). This observation suggests that the potassium loaded to the catalyst in this series has no promoting effect, all effects observed in this series might therefore be a true reflection of effects due to different crystallite sizes, obviously keeping in mind possible effects of conversion on selectivity. The large difference of the promoting effects with the two different support materials used might be due to the much larger specific surface area of the carbon support (1243.9 m^2/g compared to 161.7 m^2/g). A large fraction of potassium will therefore be located too far away from iron crystallites therefore having almost no effects; it can also be suspected that potassium might preferably be located in the micropores (2 nm) of the carbon carrier, which are not populated with iron crystallites. No pronounced crystallite size effects on olefin isomerisation could be observed with the catalysts of the carbon series; slightly higher molar α-olefin contents were only found in the experiment A10 of the alumina supported catalyst.

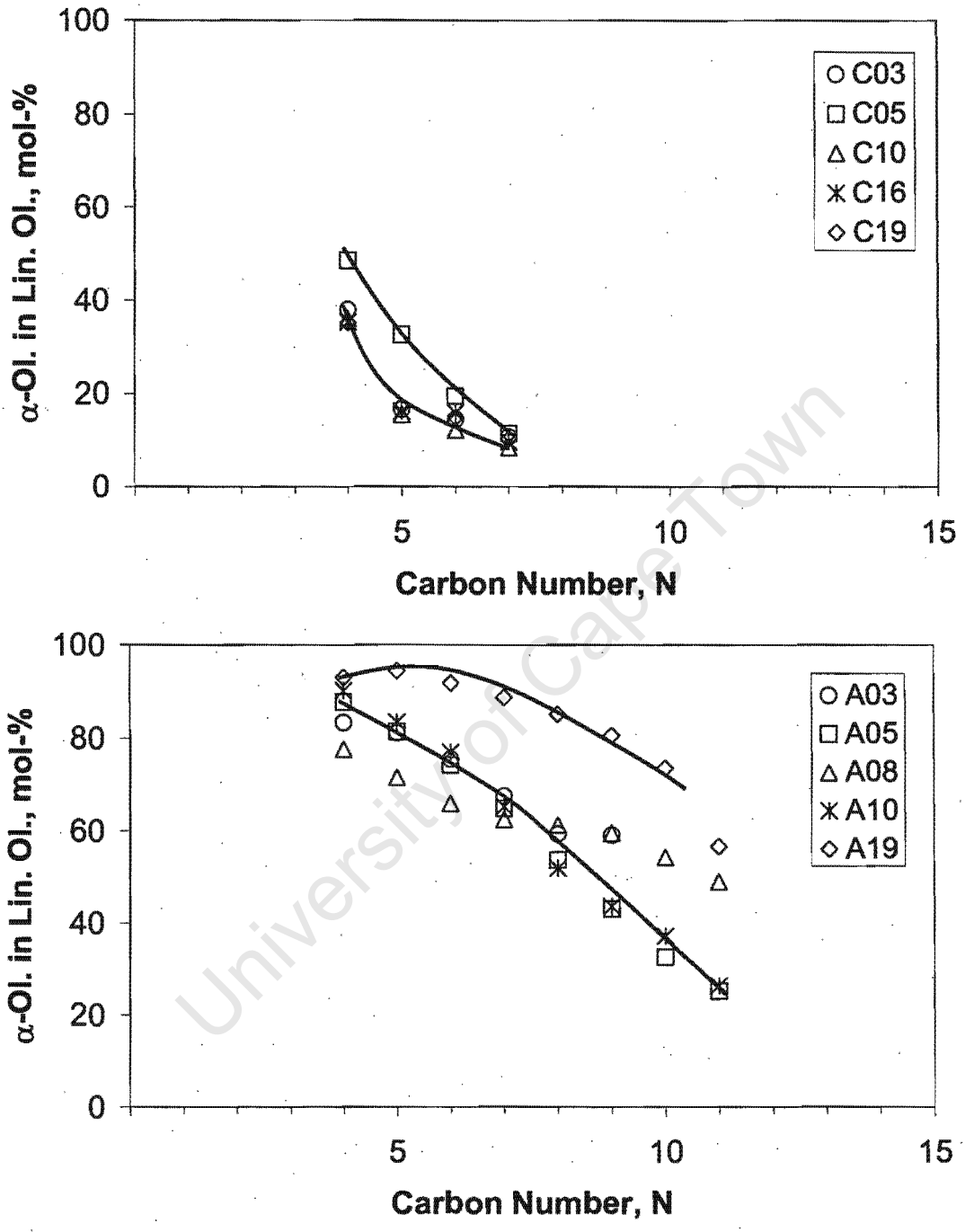

Figure 5.27: Molar content of α-olefins in corresponding fraction of linear olefins as function of carbon number in Fischer-Tropsch synthesis after 60 min time on stream for catalysts Fe/C (*top*) and Fe/Al_2O_3 (*bottom*) with varied crystallite size prepared via precipitation in water-in-oil microemulsions

In conclusion, there are no clear effects of crystallite size on the extent of secondary olefin reactions. Nonetheless as a net effect of constant olefin contents per carbon number and increasing chain growth probabilities with increasing crystallite size or enhanced effects of potassium promotion, an increase in selectivity of long chain α-olefins (C_{5+}) from 7.7 to 13 C-% is obtained in the alumina series after 60 min run time (see Table F.2).

5.5.2.4 Formation of oxygenates

Apart from hydrocarbons, small fractions of oxygenates (<15 C-%), mainly primary alcohols and aldehydes, were found in products of the Fischer-Tropsch experiments conducted. Small amounts of ketones were also detected (see Table F.2). Only little is known about the formation routes of oxygenates. According to Pichler and Schulz (1970) an oxygen containing surface species can be formed via a CO insertion step, Johnston and Joyner (1993) postulated that the same species could be formed by addition of hydroxyl groups to an alkylidene species. Desorption of this species then leads to formation of alcohols or aldehydes respectively.

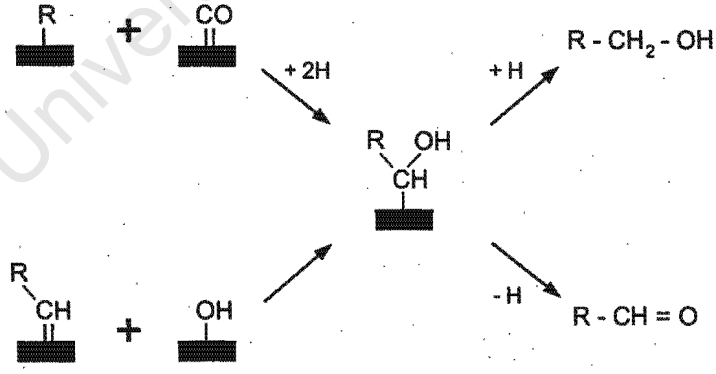

Generally fairly large amounts of alcohols plus aldehydes were found in the products of the experiments of the alumina series at 60 min time on stream (see selectivity of total alcohols and total aldehydes in Table F.2). This can again be ascribed to effects of potassium promotion on the catalysts of this series. Potassium in iron based

Fischer-Tropsch synthesis is known to result in higher oxygenate selectivity (Dry, 2004b), most likely due to inhibition of readsorption of primarily formed oxygenates in analogy to reactions of secondary olefin consumption (Claeys, 1997; Schulz and Claeys, 1999). In the carbon series the formation of alcohols mainly consists of methanol (>90 %), whereas in the alumina series more than 70 % are C_{2+} alcohols. With increasing crystallite size, an increase alcohol in selectivity and the molar content of alcohol plus aldehydes in the fraction of linear C_5 products was found in the alumina series (see Table F.2 and Figure 5.28). This might again be due to effectively enhanced potassium promotion as a result of an increase of the potassium to iron surface ratio with increasing iron crystallite size (or decreasing metal surface area respectively). Note that the reactivity of oxygenates for secondary reactions in Fischer-Tropsch synthesis has been shown to be much larger than that of corresponding α-olefins of the same carbon number (Davis, 1993), which might explain why only oxygenates are affected here and not the olefins (see also previous section).

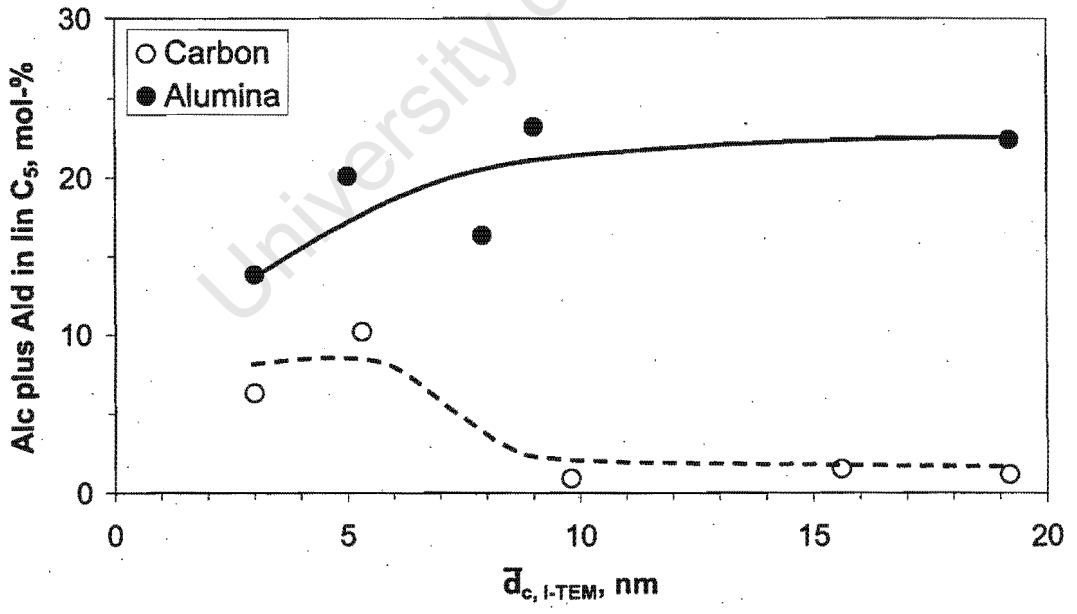

Figure 5.28: Molar content of pentanol(-1) and pentanal in the fraction of linear C_5 products in Fischer-Tropsch synthesis after 60 min time on stream for catalysts Fe/C (○) and Fe/Al_2O_3 (●) with varied iron crystallite size (TEM) prepared via precipitation in water-in-oil microemulsions

An opposite trend of selectivity of long chain oxygenates, and oxygenates content within carbon number fractions, with respect to iron crystallite size was found in the experiments of the carbon series. In this series, effects of potassium promotion were only weak or negligible (see previous section) and the observed selectivity trends should therefore be mainly due to crystallite size effects. Note that in experiment C03 conversion was much lower than in other experiments of the series, which might explain higher oxygenate contents in this series to be due to lower contact time; this does however not apply to experiment C05, in which synthesis gas conversion is similar to that in runs A08 and C10. The relatively high molar content of alcohols and aldehydes in the carbon number fractions of linear products in this experiment (see Figure 5.28) could therefore be related to crystallite size.

It has been speculated that reactions of CO insertion might indeed preferably occur on metal sites with low coordination (Schulz, 2003), i.e. atoms with small numbers of neighbours. The density of such sites is larger in small crystallites, which might explain the preferred formation of oxygenates via CO insertion in this experiment. Enhanced oxygenate selectivity has also been reported on small crystallites in CO hydrogenation studies with rhodium (Ojeda et al., 2004) and cobalt (Barbier et al., 2001) catalysts. This significant finding was only observed in the initial stages of the experiments, where the crystallite sizes are believed to be still intact, i.e. not affected by sintering effects.

5.5.2.5 Formation of branched products

So far only linear products have been discussed, the product spectra obtained in the runs conducted with the model catalysts contain up to 10 C-% branched compounds (almost exclusively monomethyl branched). Generally higher degrees of branching were found in the products of the carbon series (see Table F.2). For the formation of a methyl branched species two reaction pathways have been suggested (Schulz et al., 1988)):

- secondary incorporation of α-olefins (as e.g. proven via co-feeding of ^{14}C labelled propene by Schulz et al. (1970))
- primary formation via combination of an alkylidene and a methyl species.

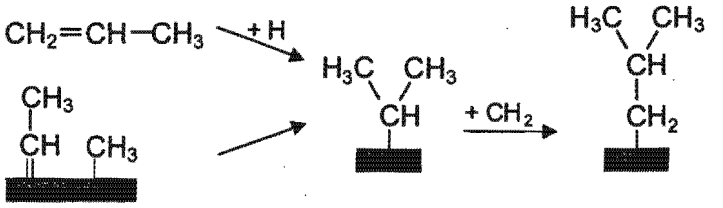

Compared to linear chain growth the formation of branched species is thought to be much more spatially demanding, formation of branched species was therefore considered an ideal probe reaction to characterize mechanistic aspects and spatial constraints on the catalyst surface in Fischer-Tropsch synthesis (Schulz et al., 1994, 1995). High degrees of branching have for example been obtained in initial stages of Fischer-Tropsch experiments, where spatial constraints should be less severe due to a less dense population of the metal surface with surface species (Schulz et al., 1999). A decrease of formation of branched compounds has also been associated with alkali promotion effects (Dry, 1981, 2004a), mainly via neutralisation of acid sites, which would catalyze skeletal isomerisation of readsorbed olefins. Such sites are introduced by supports such as alumina. Figure 5.29 shows molar iso/n ratios obtained in the C_5 fractions of the experiments with the two series of model catalysts after 60 min time on stream.

Note that the same trends were found in other carbon number fractions (not shown). With the catalysts of the alumina series a decrease of the iso/n ratios with increase of crystallite size was obtained, which might again be assigned to enhanced alkali promotion effects due to effectively increasing potassium to metal surface ratios. It is unlikely that olefins are involved in the formation of branched compounds in both series conducted seeing how little olefin readsorption was affected within each series. It is therefore suggested that potassium rather affects the primary formation

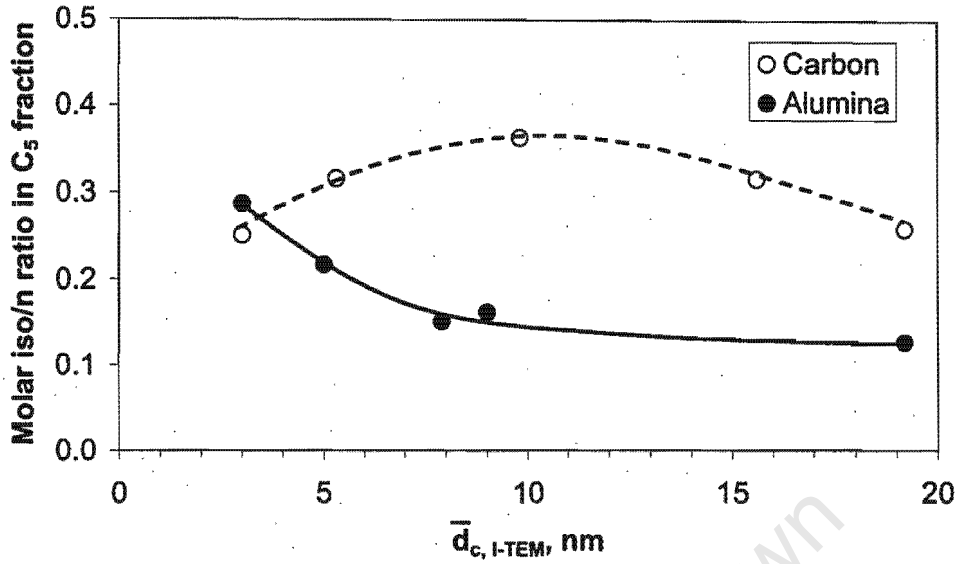

Figure 5.29: Molar ratio of methyl branched to linear products in the C_5 fraction in Fischer-Tropsch synthesis after 60 min time on stream for catalysts Fe/C (○) and Fe/Al_2O_3 (●) with varied iron crystallite size (TEM) prepared via precipitation in water-in-oil microemulsions

of branched compounds e.g. via electronic or steric effects.

Also assuming secondary olefin reaction to play no role in the experiments of the carbon series, where no effects of potassium are believed to mask selectivity, the increase of iso/n ratios with increasing crystallite size (<10 nm) might therefore be crystallite size related. It can be speculated that the spatially very demanding formation of branched compounds requires certain configurations of large ensembles of metal atoms, which might be present in higher densities in big crystallites. The decrease of iso/n ratios in crystallites larger than 10 nm can however currently not be explained. The above findings regarding chain branching are again more pronounced in the initial stages of the experiments.

5.5.2.6 Summary of product selectivity results and conclusions

Generally positive effects on product selectivity with decreasing methane selectivity, increase of chain growth probability, selectivity of long chain α-olefins and oxygenates have been observed with increasing crystallite size in the alumina supported model catalysts. These findings can either be due to direct effects of iron crystallite size on selectivity or they can be a result of enhanced effects of potassium promotion as the ratio of the fixed amounts of potassium in the catalysts to metal surface increases with increasing crystallite size in the model catalysts.

The influence of potassium seems to be much weaker or even negligible in the series with the carbon supported model catalysts, here extensive double bond isomerisation of α-olefins has been observed, which is indicative of the absence of any alkali promotion effects. It is therefore likely that the higher methane selectivity, the corresponding lower chain growth probabilities and higher molar oxygenate contents obtained in the Fischer-Tropsch experiments with the small crystallites supported on carbon are a true reflection of crystallite size effects therefore possibly implying structure sensitivity of Fischer-Tropsch selectivity as previously suggested by others (Barbier et al., 2001; Schulz et al., 2002; Claeys and Schulz, 2004; Ojeda et al., 2004).

In analogy to similar reactions known from homogeneous catalysis. It is proposed that reactions of CO insertion accounting for enhanced formation of oxygenates preferably occur on sites of low coordination which are present in higher concentrations on surfaces of small crystallites. Furthermore, it is suggested that reactions of chain growth might require certain configurations "ensembles" of iron atoms which are larger than those required for methane formation only. These "ensembles" will be present at lower concentrations in small crystallites, therefore accounting for lower chain growth probabilities. Assuming correctness of this concept with further decrease of crystallite size a point might be reached where no chain growth will be possible anymore and only C_1 products (methane and methanol) are formed. Almost pure methane (<99 C-%) is also the product which one would expect if all reaction

steps of product formation were in thermodynamic equilibrium and CO dissociation instead of product desorption might become the rate determining step. It is therefore only at this point that structure sensitivity would also impact on activity of Fischer-Tropsch synthesis. As the obtained product selectivities are still only weakly affected in the conducted experiments, it might be concluded that the observed low activity of small crystallites is indeed due to other effects such as oxidation of iron or iron carbide phases as proposed in section 5.4.

Chapter 6

Concluding Remarks and Recommendations

Preparation of nanocrystallites and supported model catalysts

One major objective of this work has been to prepare model type catalysts with varied iron crystallite size. This was successfully achieved by employing a microemulsion technique, which was used to provide well defined sizeable microreactors (reversed micelles) in which precipitation of nanocrystallites was conducted. Size control was accomplished by varying composition of the ternary microemulsion system, in particular via varying water-to-surfactant ratios. Characterisation of the microemulsion system and the resulting nanocrystallites showed a strict linear relationship of water-to-surfactant ratio and micelle size as well as crystallite size.

Adding support during the precipitation in microemulsions resulted in two series of model catalyst with discrete crystallite sizes which remained widely unchanged upon reductive pretreatment. Some of the crystallites on the support were present as clusters, which might have made their sintering during reaction more likely. Although sintering effects, which were obtained on spent catalysts after 5 day time on stream, are not believed to occur in the initial phases of the Fischer-Tropsch exper-

iments and therefore not impact on the interpretations made in this work, ideally the crystallites should be homogeneously distributed for the model type catalysts needed for the studies done.

Very little work has been described in literature on attempts to deposit nanocrystallites obtained from microemulsions onto supports. Improvement of catalyst homogeneity might be obtained by applying ultrasound during the deposition step either during addition of the support to the microemulsion system or alternatively pre-prepared nanocrystallites could be redispersed in a suitable solvent and then contacted with the support material followed by slow drying under vacuum. The nature of the support material, such as porosity and surface charge might play a crucial role during the deposition of nanocrystallites onto the support material. It is however not believed that *in situ* preparation of support material e.g. via hydrolysis of TEOS would lead to the desired results as a part of the crystallites might be encapsulated by the formed SiO_2 structure and therefore become inaccessible.

Fischer-Tropsch reaction work

Testing of the model type catalysts in Fischer-Tropsch reaction has clearly shown lower metal surface specific Fischer-Tropsch activity of small crystallites. It has been proposed that this might be a result of reoxidation as small crystallites have been suggested to reoxidise more readily than larger ones or bulk phases. Analyses of the spent catalyst has however shown severe sintering. In order to prove the possibility of reoxidation of small crystallites at Fischer-Tropsch conditions, ideally an *in situ* characterisation of the catalyst phase composition should be applied. Alternatively very short experimental runs could be done followed by thorough phase and crystallite size analyses.

Some of the experimental results from the Fischer-Tropsch runs with the model catalyst seem to indicate structure sensitivity of Fischer-Tropsch selectivity. The interpretation of the selectivity data is however believed to be hampered by a possible

effect of potassium, which was loaded at constant weight loadings to the catalyst. With increasing iron crystallite size the effective ratio of potassium to the metal surface area increased with increasing iron crystallite size in the catalyst. To simplify interpretation of such model studies it is therefore recommended to use model catalysts with different crystallite sizes which are either not alkali promoted or optimum potassium levels have to be found for each crystallite size on a given support material.

Bibliography

Abrevaya, H.: 1990, 'Fischer-Tropsch synthesis process employing a moderated ruthenium catalyst'. *US Patent* (4 945 116).

Abrevaya, H. and W. M. Targos: 1987, 'Microemulsion impregnated catalyst composite and use thereof in a synthesis gas conversion process'. *US Patent* (4714692).

Adesina, A. A.: 1996, 'Hydrocarbon synthesis via Fischer-Tropsch reaction: travails and triumphs'. *Appl. Catal A: General* **138**, 345.

Agostiano, A., M. Catalano, M. L. Curri, M. D. Monica, L. Manna, and L. Vasanelli: 2000, 'Synthesis and structural characterisation of CdS nanoparticles prepared in a four-components "water-in-oil" microemulsion'. *Micron* **31**, 253.

Agrell, J., K. Hasselbo, K. Jansson, S. G. Järås, and M. Boutonnet: 2001, 'Production of hydrogen by partial oxidation of methanol over Cu/ZnO catalysts prepared by microemulsion technique'. *Appl. Catal. A: General* **211**, 239.

Amelse, J. A., L. H. Schwartz, and J. B. Butt: 1981, 'Iron alloy Fischer-Tropsch catalysts : III. Conversion dependence of selectivity and water-gas shift'. *J. Catal.* **72**, 95.

Anderson, K. G. and J. G. Ekerdt: 1985, 'Study of Fischer-Tropsch synthesis over Fe/SiO_2: Effect of diethylamine on hydrocarbon and alcohol production'. *J. Catal.* **95**, 602.

Anderson, R. B.: 1956, *Catalysts for the Fischer-Tropsch Synthesis*, Vol. IV of *Catalysis*, p. 29. Van Nostrand-Reinhold: New York.

Anderson, R. B.: 1984, *The Fischer-Tropsch Synthesis.* Academic Press, New York.

Anderson, R. B., B. Seligman, J. F. Schultz, and M. A. Elliot: 1952, 'Fischer-Tropsch Synthesis: Some important variables of the synthesis of iron catalysts'. *Ind. Eng. Chem.* **44**(10), 391.

Andreeva, D., V. Idakiev, T. Tabakova, A. Andreev, and R. Giovanoli: 1996, 'Low-temperature water-gas shift reaction on Au/α-Fe_2O_3 catalyst'. *Appl. Catal. A: General* **134**, 275.

Arakawa, H. and A. T. Bell: 1983, 'Effect of potassium promotion on the activity and selectivity of iron Fischer-Tropsch catalysts'. *Ind. Eng. Chem. Process Des. Dev.* **22**(4), 97.

Atkins, P. W.: 1990, *Physical Chemistry.* Oxford University Press, Oxford, 4^{th} edition.

Barbier, A., A. Tuel, I. Arcon, A. Kodre, and G. A. Martin: 2001, 'Characterisation and catalytic behaviour of Co/SiO_2 catalysts: Influence of dispersion in the Fischer-Tropsch reaction'. *J. Catal.* **200**, 106.

Barnes, H. A., J. F. Hutton, and K. Walters: 1989, *An Introduction to Rheology.* Elsevier Science Publisher B. V., Amsterdam.

Bartholomew, C. H.: 1987, 'Mechanisms of Ni Catalyst Poisoning'. In: B. Delmon and G. F. Froment (eds.): *Catalyst Deactivation*, Vol. 34 of *Stud. Surf. Sci. Catal.* Elsevier, Amsterdam, p. 81.

Bartholomew, C. H.: 1991, 'Recent developments in Fischer-Tropsch catalysis'. In: L. Guczi (ed.): *Trends in CO Activation*, Vol. 64 of *Stud. Surf. Sci. Catal.* Elsevier, Amsterdam, Chapt. 8, p. 158.

Bartholomew, C. H.: 2001, 'Mechanisms of catalyst deactivation'. *Appl. Catal A: General* **212**, 17.

Bartholomew, C. H., G. D. Weathbee, and G. A. Jarvi: 1979, 'Sulfur poisoning of nickel methanation catalysts : I. in situ deactivation by H_2S of nickel and nickel bimetallics'. *J. Catal.* **60**, 257.

Bergeret, G. and P. Gallezot: 1997, 'Particle size and dispersion measurements'. Vol. 2 of *Handbook of heterogeneous catalysis.* VCH, Weinheim, Federal Republic of Germany, Chapt. 3, p. 439.

Bian, G., A. Oonuki, N. Koizumi, H. Nomoto, and M. Yamada: 2002, 'Studies with a precipitated iron Fischer-Tropsch catalyst reduced by H_2 or CO'. *J. Mol. Catal. A: Chemical* **186**, 203.

Bitter, J. H., K. Seshan, and J. A. Lercher: 1999, 'Deactivation and Coke Accumulation during CO_2/CH_4 Reforming over Pt Catalysts'. *J. Catal.* **183**, 336.

Blekkan, E. D., A. Holmen, and S. Vada: 1993, 'Alkali promotion of alumina-supported cobalt Fischer-Tropsch catalysts studied by TPR, TPD and pulse chemisorption'. *Acta Chem. Scand* **47**, 275.

Boudart, M.: 1984, 'Structure sensitivity of hydrocarbon synthesis from CO and H_2'. *J. Phys. Chem.* **88**, 11.

Boutonnet, M., J. Kizling, V. Minsta-Eya, A. Choplin, R. Touroude, G. Maire, and P. Stenius: 1987, 'Monodisperse colloidal metal particles from nonaqueous solutions: Catalytic behavior in hydrogenation of but-1-ene of platinum, palladium, and rhodium particles supported on pumice'. *J. Catal.* **103**, 95.

Boutonnet, M., J. Kizling, P. Stenius, and G. Maire: 1982, 'The preparation of monodisperse colloidal metal particles from microemulsions'. *Colloid Surf.* **5**, 209.

Bromfield, T. C. and N. J. Coville: 1999, 'The effect of sulfide ions on a precipitated iron Fischer-Tropsch catalyst'. *Appl. Catal A: General* **186**, 297.

Bukur, D. B., D. Mukesh, and S. A. Patel: 1990, 'Promoter effects on precipitated iron catalysts for Fischer-Tropsch synthesis'. *Ind. Eng. Chem. Res.* **29**, 194.

Bukur, D. B., K. Okabe, M. P. Rosynek, C. P. Li, D. J. Wang, K. R. P. M. Rao, and G. P. Huffman: 1995, 'Activity studies with a precipitated iron catalyst for Fischer-Tropsch synthesis: 1. Characterisation studies'. *J. Catal.* **155**, 353.

Capek, I.: 2004, 'Preparation of metal nanoparticles in water-in-oil (w/o) microemulsions'. *Adv. Colloid Interface Sci.* **110**, 49.

Caponetti, E., L. Pedone, D. C. Martino, V. Pantó, and V. T. Liveri: 2003, 'Synthesis, size control and passivation of CdS nanoparticles in water/AOT/n-heptane microemulsions'. *Mater. Sci. Eng. C* **23**, 531.

Catlow, C. R. A., L. Ackermann, R. G. Bell, D. H. Gay, S. Holt, D. W. Lewis, M. A. Nygren, G. Sastre, D. C. Sayle, and P. E. Sinclair: 1997, 'Modelling of structure, sorption, synthesis and reactivity in catalytic systems'. *J. Mol. Catal. A: Chemical* **115**, 431.

Claeys, M.: 1997, 'Selektivität, Elementarschritte und Kinetische Modellierung bei der Fischer-Tropsch-Synthese'. Ph.D. thesis, Universität Fridericiana Karlsruhe.

Claeys, M. and H. Schulz: 2004, 'Effects of internal mass transfer on activity and selectivity in iron based Fischer-Tropsch syntheses'. *Prepr. Pap.-Am. Chem. Soc., Div. Pet. Chem.* **49(2)**, 195.

Claeys, M. and E. van Steen: 2004, 'Basic studies'. In: A. Steynberg and M. Dry (eds.): *Fischer-Tropsch Technology*, Vol. 152 of *Studies in Surface Science and Catalysis*. Elsevier, Amsterdam, Chapt. 8, p. 601.

Corolleur, C., D. Tomanova, and F. G. Gault: 1972, 'The mechanisms of hydrogenolysis and isomerization of hydrocarbons on metals : VII. Isomerization of labeled

hexanes and hydrogenolysis of methyl (^{13}C) cyclopentane on a 10% platinum-alumina catalyst'. *J. Catal.* **24**, 401.

Craxford, S. R. and E. Rideal: 1939, 'Die Fischer-Tropsch-Synthese von Kohlewasserstoffen und einige verwandte Reaktionen'. *Brennstoff-Chem.* **20**, 263.

Davis, B. H.: 1993, '^{14}C Tracer studies of the Fischer-Tropsch synthesis'. In: *Preprints - Catalysis and catalytic processing.* Cape Town, South Africa, p. 305.

de Gennes, P. G. and C. Taupin: 1982, 'Microemulsions and the flexibility of oil/water interfaces'. *J. Phys. Chem.* **86**, 2294.

de Koster, A. and R. A. van Santen: 1991, 'Molecular orbital studies of the adsorption of CH_3, CH_2 and CH on Rh(111)'. *J. Catal.* **127**, 141.

Delmon, B., P. Grange, P. A. Jacobs, and G. Poncelet: 1987, 'Preparation of catalysts IV'. Elsevier, Amsterdam.

Donnelly, T. J. and C. N. Satterfield: 1989, 'Product distributions of the Fischer-Tropsch synthesis'. *Appl. Catal.* **52**, 93.

Dry, M. E.: 1981, *Catalysis Science and Technology*, Vol. 1, p. 159. Springer Verlag, New York.

Dry, M. E.: 1990, 'The Fischer-Tropsch process - commercial aspects'. *Catal. Today* **6**, 183.

Dry, M. E.: 1993, 'Conversion of Syngas to Fuels and Chemicals'. In: *Preprints - Catalysis and catalytic processing.* Cape Town, South Africa.

Dry, M. E.: 2004a, 'Chemical concepts used for engineering purposes'. In: A. Steynberg and M. E. Dry (eds.): *Fischer-Tropsch Technology*, Vol. 152 of *Stud. Surf. Sci. Catal.* Elsevier, Amsterdam, Chapt. 3, p. 196.

Dry, M. E.: 2004b, 'FT catalysts'. In: A. Steynberg and M. E. Dry (eds.): *Fischer-Tropsch Technology*, Vol. 152 of *Stud. Surf. Sci. Catal.* Elsevier, Amsterdam, Chapt. 7, p. 533.

Dry, M. E. and G. J. Oosthuizen: 1968, 'The correlation between catalyst surface basicity and hydrocarbon selectivity in the Fischer-Tropsch synthesis'. *J. Catal.* **11**, 18.

Duvenhage, D., N. Coville, and R. Espinoza: 1994, 'Fischer-Tropsch precipitated iron catalysts: Deactivation studies'. *Stud. Surf. Sci. Catal.* **88**, 3501.

Eastoe, J., B. H. Robison, A. J. W. G. Visser, and D. C. Steytler: 1991. *J. Chem. Soc. Faraday Trans.* **87**, 1899.

Eilers, J., S. A. Posthuma, and S. Sie: 1990, 'The Shell Middle Distillate synthesis Process (SMDS)'. *Catal. Letters* **7**, 253.

Eriksson, S., U. Nylén, S. Rojas, and M. Boutonnet: 2004, 'Preparation of catalysts from microemulsions and their applications in heterogeneous catalysis'. *Appl. Catal A: General* **265**, 207.

Erley, W., P. McBreen, and H. Ibach: 1983, 'Evidence for CH_x surface species after the hydrogenation of CO over an Fe(110) single crystal surface'. *J. Catal.* **84**, 229.

Ertl, G., H. Knözinger, and J. Weitkamp: 1997. In: G. Ertl, H. Knözinger, and J. Weitkamp (eds.): *Handbook of heterogeneous catalysis.* VCH, Weinheim, Federal Republic of Germany, Chapt. 3, p. 439.

Espinoza, R. L., A. P. Steynberg, B. Jager, and A. C. Vosloo: 1999, 'Low Temperature Fischer-Tropsch synthesis from a Sasol Perspective'. *Appl. Catal. A: General* **186**, 13.

Ferguson, J. and Z. Kemblowski: 1991, *Applied Fluid Rheology.* Elsevier Science Publisher Ltd, London.

Fischer, F. and H. Tropsch: 1926. *Brennstoff-Chemie* **7**, 97.

Fischer, F., H. Tropsch, and D. Dilthes: 1925. *Brennstoff-Chemie* **6**, 265.

Flory, P.: 1936, 'Molecular size distribution in linear condensation polymers'. *J. Amer. Chem. Soc.* **58**, 1877.

Forzatti, P. and L. Lietti: 1999, 'Catalyst deactivation'. *Catal. Today* **52**, 165.

Friedel, R. A. and R. B. Anderson: 1950, 'Composition of synthetic liquid fuels. 1. Product distribution and analysis of C_5-C_8 paraffin isomers from cobalt catalysts'. *J. Amer. Chem. Soc.* **72**, 121.

Haggin, J.: 1991, 'Several issues drive research for new catalysts for methane conversion'. *Chem. Eng. News* **22**.

Hall, A. G., A. Duangchan, and K. Smith: 1998, 'Characterisation of dispersed hydroprocessing catalysts prepared in reverse micelles'. *Can. J. Chem. Eng.* **76**, 744.

Hanaoka, T., T. Hatsuta, T. Tago, M. Kishida, and K. Wakabayashi: 2000, 'Control of the rhodium particle size of the silica-supported catalysts by using microemulsion'. *Appl. Catal. A: General* **190**, 291.

Hanaoka, T., H. Hayashi, T. Tago, M. Kishida, and K. Wakabayashi: 2001, 'In situ immobilization of ultrafine particles synthesised in a water/oil microemulsion'. *J. Colloid Interf. Sci.* **235**, 235.

Hanaoka, T., W. Y. Kim, M. Kishida, H. Nagata, and K. Wakabayashi: 1997, 'Enhancement of CO hydrogenation activity of Rh/SiO_2 with low rhodium content'. *Chem. Lett.* **7**, 645.

Hayashi, H., L. Z. Chen, T. Tago, M. Kishida, and K. Wakabayashi: 2002, 'Catalytic properties of Fe/SiO_2 catalysts prepared using microemulsion for CO hydrogenation'. *Appl. Catal. A: General* **231**, 81.

Hilmen, A. M., D. Schanke, K. F. Hanssen, and A. Holmen: 1999, 'Study of the effect of water on alumina supported cobalt Fischer-Tropsch catalysts'. *Appl. Catal A: General* **186**, 169.

Hindermann, J. P., G. J. Hutchings, and A. Kiennemann: 1993, 'Mechanistic aspects of the formation of hydrocarbons and alcohols from CO hydrogenation'. *Cat. Rev. Sci. Eng.* **35**, 1.

Hota, G., S. Jain, and K. C. Khilar: 2004, 'Synthesis of CdS-Ag_2S core-shell composite nanoparticles using AOT-n-heptane-water microemulsions'. *Colloids and Surfaces A: Physicochem. Eng. Aspects* **232**, 119.

Hou, M. J., M. Kim, and D. O. Shah: 1988, 'A light scattering study on the droplet size and interdroplet interaction in microemulsions of AOT-oil-water system'. *J. Colloid Interf. Sci.* **123**, 398.

Huang, Y. J. and J. Schwarz: 1987, 'The effect of catalyst preparation on catalytic activity: I. The catalytic activity of Ni/Al_2O_3 catalysts prepared by wet impregnation'. *Appl. Catal.* **30**, 239.

Iglesia, E.: 1997, 'Design, synthesis, and use of cobalt-based Fischer-Tropsch synthesis catalysts'. *Appl. Catal.* **161**, 59.

Iglesia, E., S. C. Reyes, R. J. Madon, and S. L. Soled: 1993, 'Selectivity control and catalyst design in the Fischer-Tropsch synthesis: sites, pellets, and reactors'. *Adv. Catal.* **39**(2), 221.

Ingelsten, H. H., R. Bagwe, A. Palmqvist, M. Skoglundh, C. Svanberg, K. Holmberg, and D. O. Shah: 2001, 'Kinetics of the formation of nano-sized platinum particles in water-in-oil microemulsions'. *J. Colloid Interf. Sci.* **241**, 104.

Ioannides, T. and X. Verikios: 1993, 'Influence of the carrier on the interaction of H_2 and CO with supported Rh'. *J. Catal.* **140**, 353.

Jacobs, G., P. M. Patterson, T. K. Das, M. Luo, and B. H. Davis: 2004, 'Fischer-Tropsch synthesis: effect of water on Co/Al_2O_3 catalysts and XAFS characterisation of reoxidation phenomena'. *Appl. Catal A: General* **270**, 65.

Jager, B. and R. L. Espinoza: 1995, 'Advances in low temperature Fischer-Tropsch synthesis'. *Catalysis Today* **23**, 17.

Jin, Y. and A. K. Datye: 2000, 'Phase transformation in iron Fischer-Tropsch catalysts during Temperature-Programmed Reduction'. *J. Catal.* **196**, 8.

Johnston, O. and R. Joyner: 1993, 'Structure function relationships in heterogeneous catalysis: the embedded surface molecule approach and its application'. In: L. Guczi, F. Solymosi, and P. Tetenyi (eds.): *Proc. "10th Int. Congr. on catalysis", Budapest 1992*, Vol. 75A of *Stud. Surf. Sci. Catal.* p. 165, Elsevier, Amsterdam.

Jun, K. W., H. S. Roh, K. S. Kim, J. S. Ryu, and K. W. Lee: 2004, 'Catalytic investigation for Fischer-Tropsch synthesis from bio-mass derived syngas'. *Appl. Catal A: General* **259**, 221.

Kaiser, R.: 1969, 'Chromatographie in der Gasphase'. Bibliographisches Institut, Mannheim, band *iii*, 2. edition.

Kaminsky, M., N. Winograd, G. Geoffroy, and M. A. Vannice: 1986, 'Direct SIMS observation of methylidyne, methylene and methyl intermediates on a Ni(III) methanation catalyst'. *J. Am. Chem. Soc.* **108**, 1315.

Kazansky, V. B., A. V. Zaitsev, V. Y. Borovkov, and A. L. Lapidus: 1988, 'Infrared diffuse reflectance study of alkali promoted iron/alumina and cobalt/alumina Fischer-Tropsch catalysts prepared by decomposition of carbonyls'. *Appl. Catal.* **40**, 17.

Khiew, P. S., S. Radiman, N. M. Huang, and M. S. Ahmad: 2003, 'Studies on the growth and characterisation of CdS and PbS nanoparticles using sugar-ester nonionic water-in-oil microemulsion'. *J. Crys. Growth* **254**, 235.

Kinugasa, T., A. Kondo, S. Nishimura, Y. Miyauchi, Y. Nishii, K. Watanabe, and H. Takeuchi: 2002, 'Estimation of size of reverse micelles formed by AOT and SDEHP based on viscosity measurements'. *Colloids and Surfaces A: Physicochem. Eng. Aspects* **204**, 193.

Kishida, M., K. Umakoshi, J. Ishiyama, H. Nagata, and K. Wakabayashi: 1996, 'Hydrogenation of carbon dioxide over metal catalysts prepared using microemulsion'. *Catal. Today* **29**, 355.

Kock, A., H. Fortuin, and J. Geus: 1985, 'The reduction behaviour of supported iron catalysts in hydrogen or carbon monoxide atmospheres'. *J. Catal.* **96**, 261.

Kölbel, H. and M. Ralek: 1980. *Cat. Rev. Sci. Eng.* **21**, 225.

Kuipers, E. W., I. H. Vinkenburg, and H. Oosterbeek: 1995, 'Chain length dependence of α-olefin readsorption in Fischer-Tropsch synthesis'. *J. Catal.* **152**, 199.

Kung, H. H. and M. C. Kung: 2003, 'Heterogeneous catalysis: what lies ahead in nanotechnology'. *Appl. Catal. A: General* **246**, 193.

Kung, H. H. and M. C. Kung: 2004, 'Nanotechnology: applications and potentials for heterogeneous catalysis'. *Catal. Today* **97**, 219.

Li, S., S. Krishnamoorthy, A. Li, G. D. Meitzner, and E. Iglesia: 2002, 'Promoted iron-based catalysts for the Fischer-Tropsch synthesis: design, synthesis, site densities and catalytic properties'. *J. Catal.* **206**, 202.

Lide, D. R. and H. V. Kehiaian: 1994, *CRC Handbook of thermophysical and thermochemical data.* CRC Press, Boca Raton.

Limin, Q., M. Jiming, C. Humin, and Z. Zhenguo: 1996, 'Preparation of $BaSO_4$ nanoparticles in non-ionic w/o microemulsions'. *Colloids and Surfaces A: Physicochem. Eng. Aspects* **108**, 117.

Lin, H. Y., Y. W. Chen, and C. Li: 2003, 'The mechanism of reduction of iron oxide by hydrogen'. *Thermochim. Acta* **400**, 61.

Lin, Z.-Z., T. Okuhara, M. Misono, K. Tohji, and Y. Udagawa: 1986, 'Pronounced effect of particle size on selectivity observed for carbon monoxide hydrogenation over ruthenium-alumina catalysts'. *J. Chem. Soc. Chem. Commun.* p. 1673.

Liu, Y.: 1992, 'Untersuchungen zur Selektivität der Fischer-Tropsch-Synthese an Kobalt- und Eisenkatalysatoren'. Ph.D. thesis, Technische Hochschule Darmstadt.

Lopez-Quintela, M. A. and J. Rivas: 1993, 'Preparation of ultrafine Nd-Fe-B magnetic particles by chemical reduction in microemulsions'. *J. Colloid Interf. Sci.* **158**, 446.

Lox, E. S. and G. F. Froment: 1993, 'Kinetics of the Fischer-Tropsch reaction on a precipitated promoted iron catalyst. 2. Kinetic modelling'. *Ind. Eng. Chem. Res.* **32**, 71.

Luo, M. and B. H. Davis: 2003, 'Fischer-Tropsch synthesis: activation of low-alpha potassium promoted iron catalysts'. *Appl. Catal A: General* **246**, 171.

Maitlis, P. M., R. Quyoum, H. C. Long, and M. L. Turner: 1999, 'Towards a chemical understanding of the Fischer-Tropsch reaction: alkene formation'. *Appl. Catal A: General* **186**, 363.

Mansker, L. D., Y. J. Dragomir, B. Bukur, and A. K. Datye: 1999, 'Characterisation of slurry phase iron catalysts for Fischer-Tropsch synthesis'. *Appl. Catal A: General* **186**, 277.

Marion, G. M., D. C. Catling, and J. S. Kargel: 2003, 'Modeling aqueous ferrous iron chemistry at low temperatures with application to Mars'. *Geochimica et Cosmochimica Acta* **67**, 4251.

McVicker, G. B. and M. A. Vannice: 1980, 'The preparation, characterization, and use of supported potassium-Group VIII metal complexes as catalysts for CO hydrogenation'. *J. Catal.* **63**, 25.

Menon, P. G.: 1990, 'Coke on catalysts-harmful, harmless, invisible and beneficial types'. *J. Mol. Catal.* **59**, 207.

Moulijn, J. A., A. E. van Diepen, and F. Kapteijn: 2001, 'Catalyst deactivation: is it predictable? What to do?'. *Appl. Catal. A: General* **212**, 3.

Nagy, J. B., A. Gourgue, and G. Derouane: 1983. In: P. Grange and P. A. Jacobs (eds.): *Preparation of Catalysts III*, Vol. 16 of *Stud. Surf. Sci. Catal.* Elsevier, Amsterdam, p. 193.

Newsome, D. S.: 1980, 'The water-gas shift reaction'. *Cat. Rev. Sci. Eng.* **21**, 275.

Nijs, H. and P. A. Jacobs: 1980, 'Metal particle size distributions and Fischer-Tropsch selectivity. An extended Schulz-Flory model'. *J. Catal.* **65**, 328.

Ojeda, M., S. Rojas, M. Boutonnet, F. Perez-Alonso, F. J. Garcia-Garcia, and J. L. G. Fierro: 2004, 'Synthesis of Rh nano-particles by the microemulsion technology: Particle size effect on the CO+H_2 reaction'. *Appl. Catal A: General* **274**, 33.

Ozin, G. A.: 1992. *Adv. Mater.* **4**, 612.

Phala, N.: 2004, 'A theoretical investigation in heterogeneous gold catalysis'. Ph.D. thesis, University of Cape Town.

Pichler, H.: 1952, 'Twenty-five years of synthesis of gasoline by catalytic conversion of carbon monoxide and hydrogen'. *Adv. Catal.* **4**, 271.

Pichler, H. and H. Schulz: 1970, 'Neuere Erkenntnnisse auf dem Gebiet der Synthese von Kohlenwasserstoffen aus CO und H_2'. *Chem.-Ing. Techn.* **42**, 1162.

Pileni, M. P. (ed.): 1989, 'Structure and Reactivity in Reverse Micelles', Vol. 65 of *Stud. Phys. Theor. Chem.* Elsevier, Amsterdam.

Pileni, M. P.: 1993, 'Water in oil colloidal droplets used as microreactors'. *Adv. Colloid Interface Sci.* **46**, 139.

Pileni, M. P.: 2003, 'Nanocrystals: fabrication, organisation and collective properties'. *C. R. Chimie* **6**, 965.

Pillai, V., P. Kumar, M. J. Hou, P. Ayyub, and D. O. Shah: 1995, 'Preparation of nanoparticles of silver halides, superconductors and magnetic materials using water-in-oil microemulsions as nano-reactors'. *Adv. Colloid Interface Sci.* **55**, 241.

Rainer, D. R., M. C. Wu, D. I. Mahon, and D. W. Goodman: 1996, 'Adsorption of CO on $Pd/Al_2O_3/Ta(110)$ model catalysts'. *J. Vac. Sci. Technol. A* **14(3)**, 1184.

Raje, A. P., R. J. O'Brien, and B. H. Davis: 1998, 'Effect of potassium on iron -based catalysts for Fischer-Tropsch synthesis'. *J. Catal.* **180**, 36.

Rao, K. R. P. M., F. E. Huggins, V. Mahajan, G. P. Huffman, V. U. S. Rao, B. L. Bhatt, D. B. Bukur, B. H. Davis, and R. J. O'Brien: 1995, 'Mössbauer spectroscopy study of iron-based catalysts used in Fischer-Tropsch synthesis'. *Top. Catal.* **2**, 71.

Ren-Yuan, T., Z. Su, W. Chengyu, L. Dongbai, and L. Liwu: 1987, 'An in-situ combined temperature programmed reduction Mössbauer spectroscopy of alumina supported iron catalysts'. *J. Catal.* p. 440.

Reuel, R. C. and C. H. Bartholomew: 1984a, 'Effects of support and dispersion on the CO hydrogenation activity/selectivity properties of cobalt'. *J. Catal.* **85**, 78.

Reuel, R. C. and C. H. Bartholomew: 1984b, 'The stoichiometries of H_2 and CO adsorptions on cobalt: Effects of support and preparation'. *J. Catal.* **85**, 63.

Rhodes, C., G. J. Hutchings, and A. M. Ward: 1995, 'Water-gas shift reaction: finding the mechanistic boundary'. *Catal. Today* **23**, 43.

Rostrup-Nielsen, J. R.: 1974, 'Coking on nickel catalysts for steam reforming of hydrocarbons'. *J. Catal.* **33**, 184.

Rostrup-Nielsen, J. R.: 1991. In: C. H. Bartholomew (ed.): *Catalyst Deactivation*, Vol. 68 of *Stud. Surf. Sci. Catal.* Elsevier, Amsterdam, p. 85.

Rostrup-Nielsen, J. R. and D. L. Trimm: 1977, 'Mechanisms of carbon formation on nickel-containing catalysts'. *J. Catal.* **48**, 155.

Ruckenstein, E. and D. B. Dadyburjor: 1983. *Rev. Chem. Eng.* **1**, 251.

Sabatier, P. and J. B. Senderens: 1902, 'New syntheses of methane'. *J. Soc. Chem. Ind.* **21**, 504.

Sachtler, W. M. H. and M. Ichikawa: 1986, 'Catalytic site requirements for elementary steps in syngas conversion to oxygenates over promoted rhodium'. *J. Phys. Chem.* **90**, 4752.

Sasol: 2003, 'Sasol launches new global industry in Qatar'. *News Centre.* Sasol internet: www.sasol.com/sasol.

Schulz, G. V.: 1935, 'The relation between reaction rate and composition of the reaction product in macropolymerisation processes'. *Z. Physik. Chem.* **B30**, 379.

Schulz, H.: 1999, 'Short history and present trends of Fischer-Tropsch synthesis'. *Appl. Catal A: General* **186**, 3.

Schulz, H.: 2003, 'Major and minor reactions in Fischer-Tropsch synthesis on cobalt catalysts'. *Topics in Catalysis* **26(1-4)**, 73.

Schulz, H., K. Beck, and E. Erich: 1988, 'Mechanism of the Fischer-Tropsch process'. *Stud. Surf. Sci. Catal.* **36**, 457.

Schulz, H. and M. Claeys: 1999, 'Reactions of α-olefins of different chain length added during Fischer-Tropsch synthesis on a cobalt catalyst in a slurry reactor'. *Appl. Catal A: General* **186**, 71.

Schulz, H., E. Erich, H. Gorre, and E. van Steen: 1990, 'Regularities as a key for discriminating surface reactions and formation of the dynamic system'. *Catal. Lett.* **7**, 157.

Schulz, H. and S. Nehren: 1986, 'Die Herstellung von Gas/Dampf - Eichgemischen für die Gaschromatographie'. *Erdöl und Kohle - Erdgas - Petrochemie* **39**, 93.

Schulz, H., Z. Nie, and F. Ousmanov: 2002, 'Construction of the Fischer-Tropsch regime with cobalt catalysts'. *Catal. Today* **71**, 351.

Schulz, H., B. R. Rao, and M. Elstner: 1970, '^{14}C-Studien zum Reaktionsmechanismus der Fischer-Tropsch-Synthese'. *Erdöl und Kohle* **22**, 651.

Schulz, H., G. Schaub, M. Claeys, and T. Riedel: 1999, 'Transient initial kinetic regimes of Fischer-Tropsch synthesis'. *Appl. Catal A: General* **186**, 215.

Schulz, H., E. van Steen, and M. Claeys: 1994, 'Selectivity and mechanism of Fischer-Tropsch synthesis with iron and cobalt catalysts'. Vol. 81 of *Stud. Surf. Sci. Catal.* Elsevier, Amsterdam, p. 455.

Schulz, H., E. van Steen, and M. Claeys: 1995, 'Specific inhibition as the kinetic principle of Fischer-Tropsch synthesis'. *Topics in Catalysis* **2**, 223.

Schwuger, M., K. Stickdorm, and R. Schomacker: 1995. *Chem. Rev.* **95**, 849.

Shultz, J. F., L. J. E. Hofer, F. S. Karn, and R. B. Anderson: 1962, 'Studies of the Fischer–Tropsch synthesis'. *J. Phys. Chem.* **66**, 501.

Sie, S. T., M. M. G. Senden, and H. M. H. van Wechem: 1991, 'Conversion of natural gas to transportation fuels via the shell middle distillate synthesis process (SMDS)'. *Catal. Today* **8**(4), 371.

Sjöbolm, J., R. Lindberg, and S. E. Friberg: 1996, 'Microemulsions- phase equilibria characterization, structures, applications and chemical reactions'. *Adv. Colloid Interface Sci.* **65**, 125.

Song, K. C. and Y. Kang: 2000, 'Precipitation of high surface area tin oxide powders by a homogeneous precipitation method'. *Mater. Lett.* **42**, 283.

Song, K. C. and J. H. Kim: 1999, 'Preparation of nanosize tin oxide particles from water-in-oil microemulsions'. *J. Colloid Interf. Sci.* **212**, 193.

Song, K. C. and J. H. Kim: 2000, 'Synthesis of high surface area tin oxide powders via water-in-oil microemulsions'. *Powder Technology* **107**, 268.

Stenius, P., J. Kizling, and M. Boutonnet: 1984, 'Liquid suspension of particles of a metal belonging to the platinum group and a method for the manufacture of such a suspension'. *US Patent* (4,424,261).

Steynberg, A. P.: 2004, 'Introduction to Fischer-Tropsch technology'. In: A. Steynberg and M. Dry (eds.): *Fischer-Tropsch Technology*, Vol. 152 of *Studies in Surface Science and Catalysis*. Elsevier Science, Chapt. 1, p. 1.

Steynberg, A. P., M. E. Dry, B. H. Davis, and B. B. Breman: 2004, 'Fischer-Tropsch reactors'. In: A. Steynberg and M. Dry (eds.): *Fischer-Tropsch Technology*, Vol. 152 of *Studies in Surface Science and Catalysis*. Elsevier Science, Chapt. 2, p. 64.

Steynberg, A. P., R. L. Espinoza, B. Jager, and A. C. Vosloo: 1999, 'High Temperature Fischer-Tropsch synthesis in commercial practice'. *Appl. Catal. A: General* **186**, 41.

Storch, H. H., N. Golumbic, and R. B. Anderson: 1951, *The Fischer-Tropsch and Related Synthesis*. John Wiley & Sons, Inc., New York.

Tanford, C.: 1972, 'Micelle shape and size'. *J. Phys. Chem.* **76**, 3020.

Tauster, S. J., S. C. Fung, and R. L. Garten: 1978, 'Strong metal-support-interaction: group VIII noble metals support on TiO_2'. *J. Amer. Chem. Soc.* **100**, 170.

Tijmensen, M. J. A., A. P. C. Faaij, C. N. Hamelinck, and M. R. M. van Hardeveld: 2002, 'Exploration of the possibilities for production of Fischer-Tropsch liquids and power via biomass gasification'. *Biomass and Bioenergy* **23**, 129.

Trimm, D. L.: 1983, 'Catalyst design for reduced coking (review)'. *Appl. Catal.* **5**, 263.

van der Laan, G. P.: 1999, 'Kinetics, selectivity and scale up of the Fischer-Tropsch synthesis'. Ph.D. thesis, University of Groningen.

van Hardeveld, R. and F. Hartog: 1969, 'The statistics of surface atoms and surface sites on metal crystals'. *Surf. Sci.* **15**, 189.

van Steen, E., M. Claeys, M. E. Dry, J. van de Loosdrecht, E. L. Viljoen, and J. L. Visagie: 2005, 'Stability of nano-crystals: Thermodynamic analysis of oxidation and re-reduction of cobalt in water/hydrogen mixtures'. *J. Phys. Chem. B* **109**, 3575.

van Steen, E. and H. Schulz: 1999, 'Polymerisation kinetics of the Fischer-Tropsch CO hydrogenation using iron and cobalt based catalysts'. *Appl. Catal. A: General* **186**, 309.

Vanhove, D., P. Makambo, and M. Blanchard: 1979, 'Selective catalytic synthesis of linear paraffins from CO and H_2 over cobalt supported catalysts'. *J.C.S. Chem. Comm.* p. 605.

Vannice, M. A.: 1975, 'The catalytic synthesis of hydrocarbons from carbon monoxide and hydrogen'. *J. Catal.* **37**, 449.

Vannice, M. A.: 1977, 'The catalytic synthesis of hydrocarbons from H_2/CO mixtures over the group VIII metals'. *J. Catal.* **50**, 228.

Wang, C. J. and J. G. Ekerdt: 1984, 'Evidence for alkyl intermediates during Fischer-Tropsch synthesis and their relation to hydrocarbon products'. *J. Catal.* **86**, 239.

Wanke, S. E. and P. C. Flynn: 1975, 'A model of supported metal catalysts sintering. I. Development of model'. *Cat. Rev. Sci. Eng.* **12**, 93.

Weber, A. P., M. Seipenbusch, and G. Kasper: 2003, 'Size effects in the catalytic activity of unsupported metallic nanoparticles'. *J. Nanopart. Res.* **5**, 293.

Zaera, F.: 2004, 'Mechanistic requirements for catalytic active sites'. *J. Phys.: Condens. Matter* **16**, 2299.

Appendix A

Anderson-Schulz-Flory Polymerisation Kinetics

The molar content of Fischer-Tropsch products decreases with increasing carbon number according to the so-called Anderson-Schulz-Flory (ASF) polymerisation kinetics described by the following equation:

$$\lg(x_N) = N\lg(p_g) + \lg\frac{(1-p_g)}{p_g} \tag{A.1}$$

where x_N is the mole fraction of products having N carbon atoms and p_g is the probability of chain growth. Here the probability of chain growth is assumed to be independent of chain length.

The derivation of equation A.1 is based on the hydrocarbon synthesis chain growth and desorption scheme shown in Figure A.1. The proposed basic model neglects

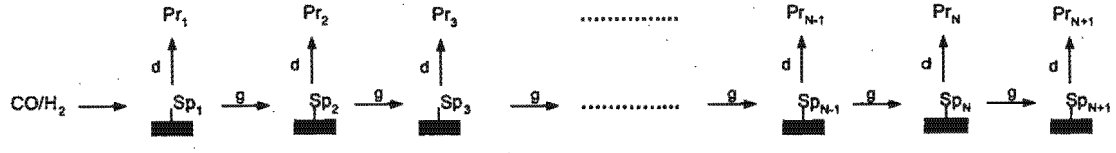

Figure A.1: Kinetic scheme of Fischer-Tropsch hydrocarbon chain growth and desorption

the formation of oxygenates and branched hydrocarbons and makes the assumption that only one sort of product Pr_N can desorb. A mass balance around a surface species Sp_N at steady state results in:

$$r_{f,Sp_N} = r_{c,Sp_N} \tag{A.2}$$

Eq. A.2 implies that:

$$r_{g,Sp_{N-1}} = r_{d,Sp_N} + r_{g,Sp_N} \tag{A.3}$$

Product, Pr_N, is formed by the desorption of surface species, Sp_N, this results in:

$$r_{f,Pr_N} = r_{d,Sp_N} \tag{A.4}$$

Therefore;

$$r_{f,Pr_N} = \frac{r_{d,Sp_N}}{r_{d,Sp_N} + r_{g,Sp_N}} \cdot \left(r_{d,Sp_N} + r_{g,Sp_N}\right) \tag{A.5}$$

Definitions:

$$\text{Desorption probability :} \quad p_{d,N} = \frac{r_{d,Sp_N}}{r_{d,Sp_N} + r_{g,Sp_N}} \tag{A.6}$$

$$\text{Chain growth probability :} \quad p_{g,N} = \frac{r_{g,Sp_N}}{r_{d,Sp_N} + r_{g,Sp_N}} \tag{A.7}$$

From these definitions, it follows that:

$$p_{d,N} + p_{g,N} = 1 \tag{A.8}$$

Substituting Eqs. A.3 and A.6 into Eq. A.5:

$$r_{f,Pr_N} = p_{d,N} \cdot \frac{r_{g,Sp_{N-1}}}{r_{d,Sp_{N-1}} + r_{g,Sp_{N-1}}} \cdot \left(r_{d,Sp_{N-1}} + r_{g,Sp_{N-1}}\right) \tag{A.9}$$

Now substituting modified Eqs. A.3 and A.7 into Eq. A.9:

$$r_{f,Pr_N} = p_{d,N} \cdot p_{g,N-1} \cdot \frac{r_{g,Sp_{N-2}}}{r_{d,Sp_{N-2}} + r_{g,Sp_{N-2}}} \cdot \left(r_{d,Sp_{N-2}} + r_{g,Sp_{N-2}}\right) \tag{A.10}$$

It follows from Eq. A.10 that:

$$r_{f,Pr_N} = p_{d,N} \cdot p_{g,N-1} \cdot p_{g,N-2} \cdot \frac{r_{g,Sp_{N-3}}}{r_{d,Sp_{N-3}} + r_{g,Sp_{N-3}}} \cdot \left(r_{d,Sp_{N-3}} + r_{g,Sp_{N-3}}\right) \qquad (A.11)$$

An analogous balance can be made for the surface species Sp_{N-3}, Sp_{N-4}, etc. to Sp_1:

$$r_{f,Pr_N} = p_{d,N} \cdot p_{g,N-1} \cdot p_{g,N-2} \cdots\cdots\cdots p_{g,2} \cdot \frac{r_{g,Sp_1}}{r_{d,Sp_1} + r_{g,Sp_1}} \cdot \left(r_{d,Sp_1} + r_{g,Sp_1}\right) \qquad (A.12)$$

which leads to:

$$r_{f,Pr_N} = p_{d,N} \cdot p_{g,N-1} \cdot p_{g,N-2} \cdots\cdots\cdots p_{g,2} \cdot p_{g,1} \cdot r_{f,Sp_1} \qquad (A.13)$$

Since all product compounds are formed starting from a C_1 species, the sum of the formation rates of all products, Pr_N ($N = 1, 2, \ldots, \infty$), must equal the consumption rate of the species Sp_1, the chain starter:

$$r_{f,Sp_1} = \sum_{N=1}^{\infty} r_{f,Pr_N} \qquad (A.14)$$

The molar content of a product compound x_N with N carbon atoms in the total organic product spectrum is:

$$x_N = \frac{r_{f,Pr_N}}{\sum_{N=1}^{\infty} r_{f,Pr_N}} = p_{d,N} \cdot p_{g,N-1} \cdot p_{g,N-2} \cdots\cdots\cdots p_{g,2} \cdot p_{g,1} \qquad (A.15)$$

If the probability of chain growth p_g is assumed to be independent of chain length N then Eq. A.15 becomes:

$$x_N = p_g^{N-1} \cdot p_d = p_g^{N-1} \cdot (1 - p_g) \qquad (A.16)$$

Taking logarithms to both sides of Eq. A.16, we get:

$$\lg(x_N) = (N-1)\,p_g + \lg(1-p_g) \tag{A.17}$$

Eq. A.17 is equal to:

$$\lg(x_N) = N\lg(p_g) + \lg\frac{(1-p_g)}{p_g} \tag{A.18}$$

Eq. A.18 is the Anderson-Schulz-Flory (ASF) equation that describes the product distribution with p_g being the only parameter. A plot of $\lg(x_N)$ against carbon number N gives a straight line from which p_g can be deduced.

Appendix B

BET Nitrogen Desorption Plots

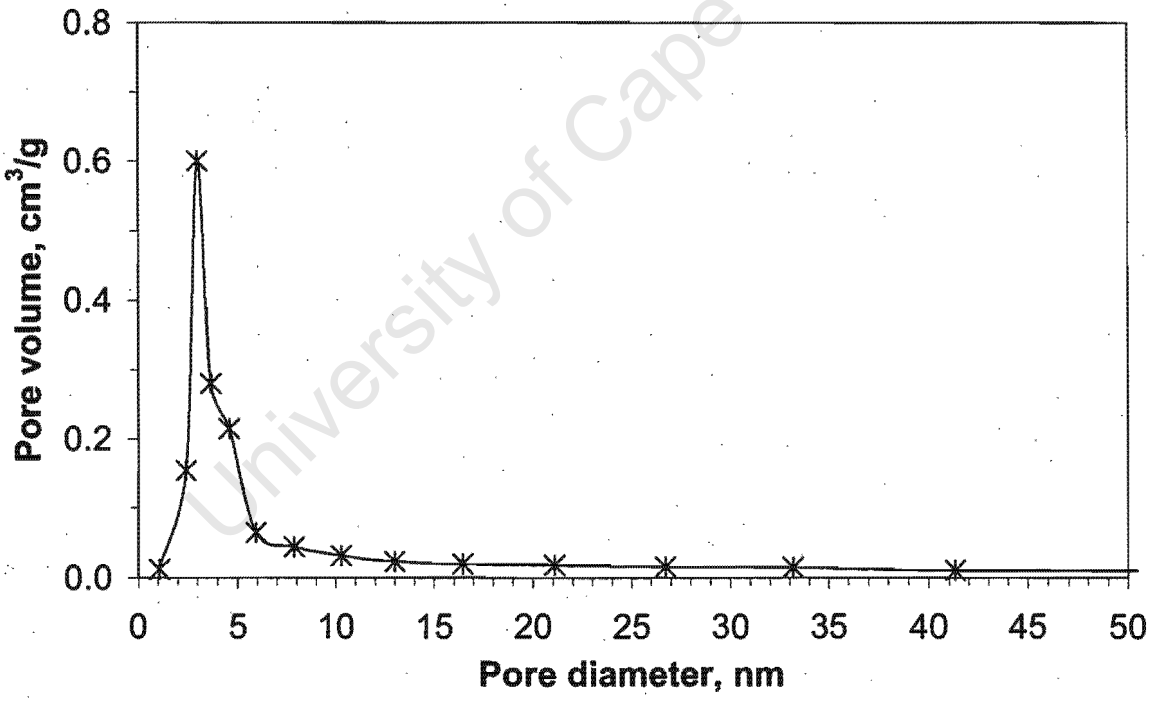

Figure B.1: dV/dlog(D) Desorption pore volume plot of activated carbon used as support material. BET surface area: 1243.9 m^2/g; BET Average pore diameter: 2.03 nm

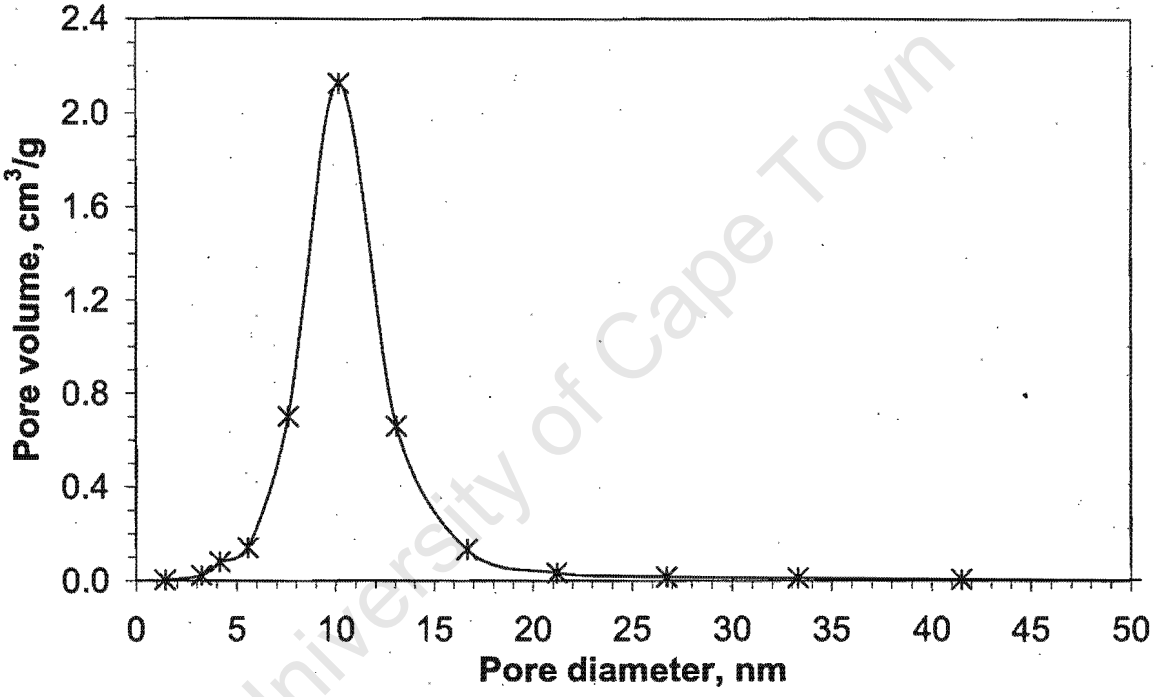

Figure B.2: dV/dlog(D) Desorption pore volume plot of alumina used as support material. BET surface area: 161.7 m^2/g; BET Average pore diameter: 11.47 nm

Appendix C

Ampoule Breaker

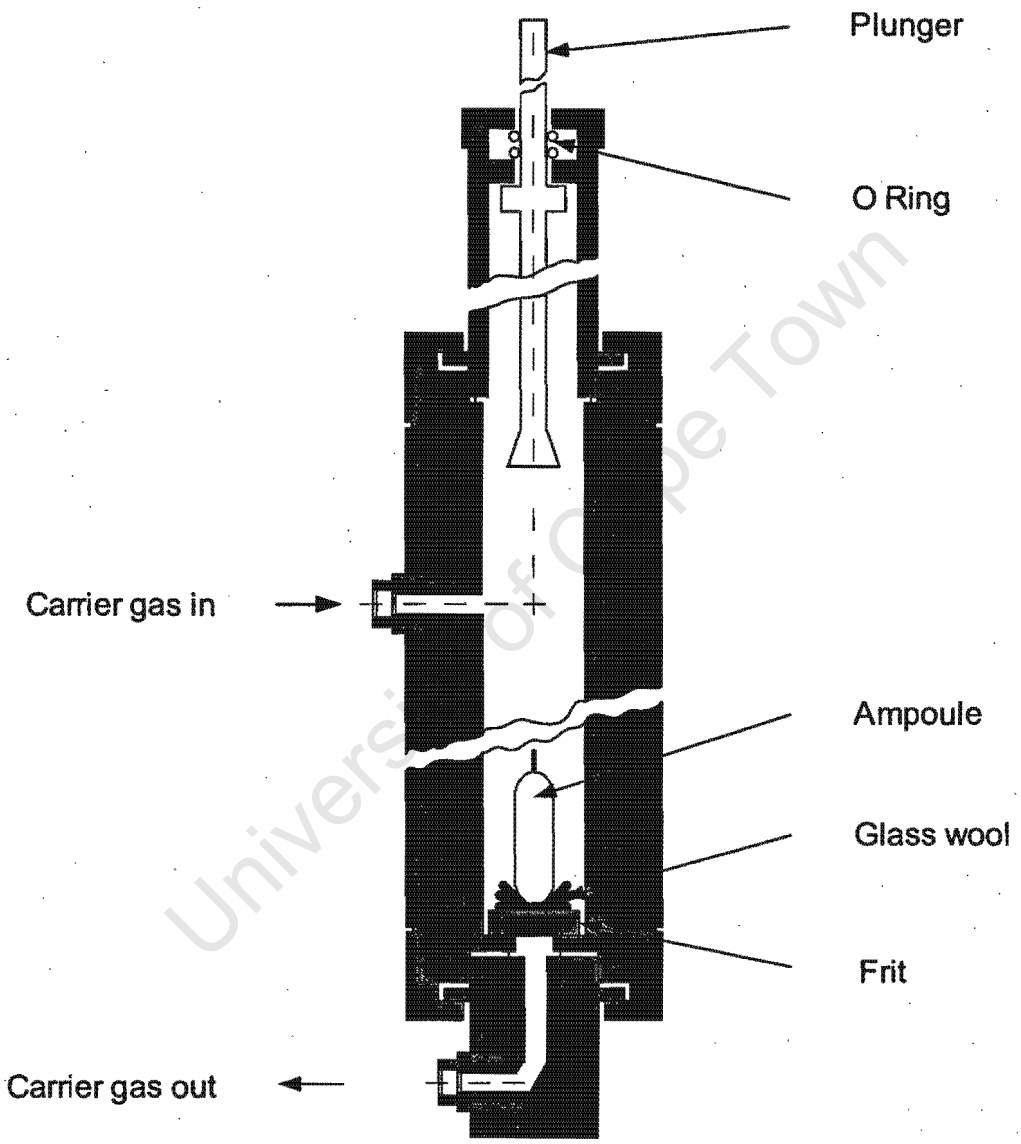

Figure C.1: Ampoule breaker system of GC FID analysis

Appendix D

SEM Pictures of catalysts

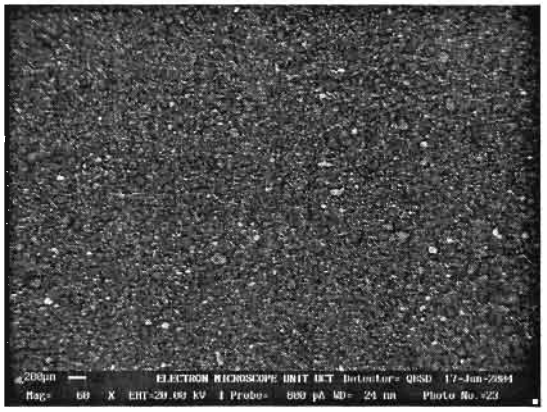

(a) C05

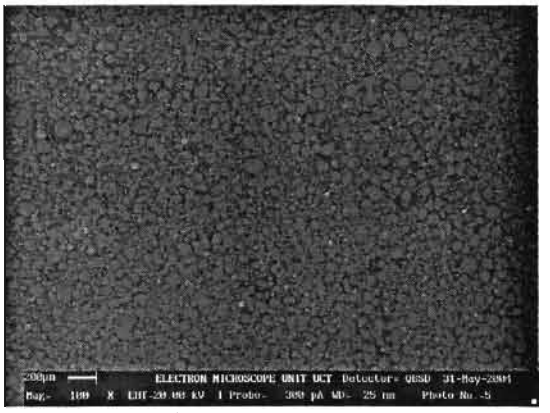

(b) A05

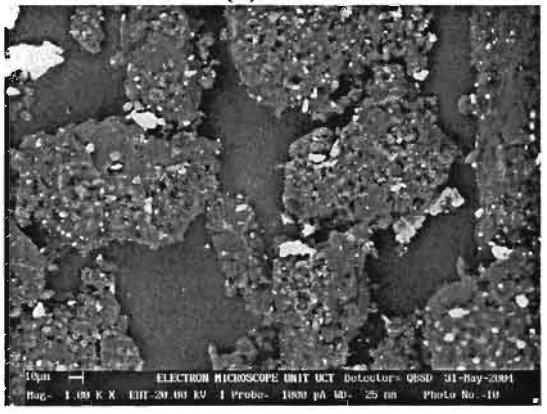

(c) C10

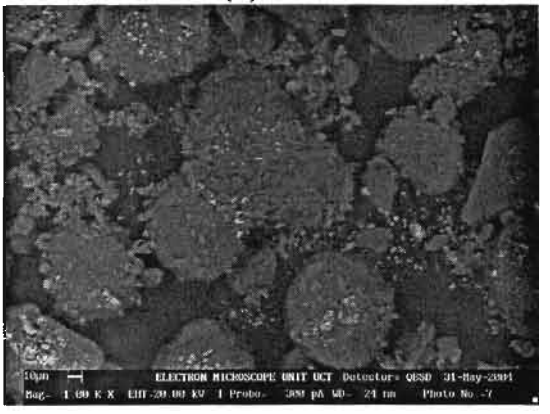

(d) A10

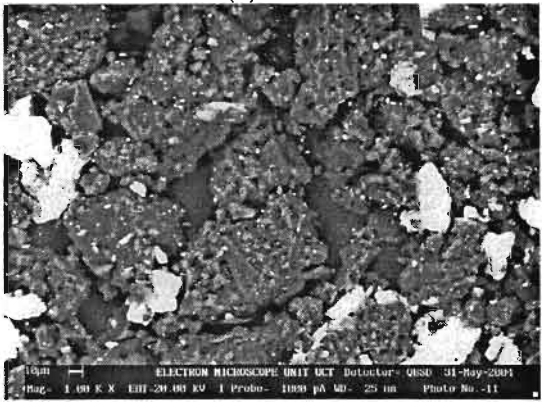

(e) C16

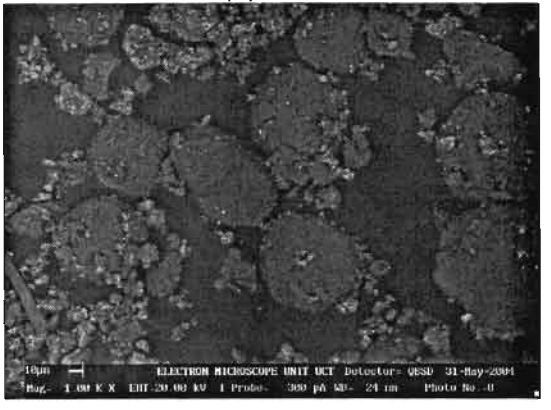

(f) A16

Figure D.1: SEM pictures of supported fresh catalysts with varied crystallite size prepared via precipitation in water-in-oil microemulsions; *left*: carbon supported catalysts; *right*: alumina supported catalysts

Appendix E

Theoretical Modelling of Reverse Micelle Size

An ideal reverse micelle diagram showing the water pool part and the surfactant film part separated from the surrounding oil phase is illustrated in Figure E.1.

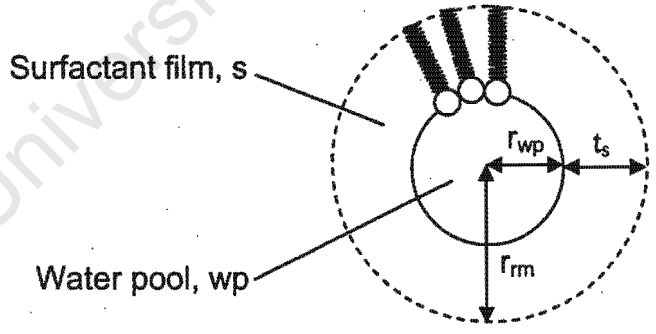

Figure E.1: Description of the reverse micelle dimensions

Assuming that the micelle particles are spherical and have uniform particle size at a particular water-to-surfactant weight ratio, ω_{wt}, the aggregation number, n_{ag}, is constant. The volume fraction, ϕ of the dispersed spherical particles in solution is

defined by Kinugasa et al. (2002) as:

$$\phi = N_A V_{rm} C_{rm} = \frac{N_A V_{rm} C_s}{n_{ag}} \tag{E.1}$$

V_{rm} is the volume of a reverse micelle, C_{rm} is the concentration of reverse micelles, C_s is the concentration of the surfactant and N_A is Avogadro's constant. From Figure E.1, V_{rm} and V_{wp}, may be expressed in terms of the radius of the micelle, r_{rm}, the radius of the waterpool, r_{wp}, and the thickness of the surfactant layer, t_s:

$$V_{rm} = \frac{4\pi r_{rm}^3}{3} \tag{E.2}$$

$$V_{wp} = \frac{4\pi r_{wp}^3}{3} \tag{E.3}$$

$$r_{rm} = r_{wp} + t_s \tag{E.4}$$

Using equations E.3 and E.4, V_{rm} can be re-written as:

$$V_{rm} = \frac{4\pi}{3}\left[\left(\frac{3V_{wp}}{4\pi}\right)^{\frac{1}{3}} + t_s\right]^3 \tag{E.5}$$

V_{wp} can be expressed based on volume of a water present, V_w, and the total number of reverse micelles present in the solution, N_{rm}:

$$V_{wp} = \frac{V_w}{N_{rm}} = \frac{V_w n_{ag}}{N_A V_T C_s} \tag{E.6}$$

with V_T the total volume of the reverse micelle system. Substituting equation E.6 into E.5 gives:

$$V_{rm} = \frac{4\pi}{3}\left[\left(\frac{3V_w n_{ag}}{4\pi N_A C_s V_T}\right)^{\frac{1}{3}} + t_s\right]^3 \tag{E.7}$$

Consequently, equation E.1 can be re-written as:

$$\phi = \frac{4\pi N_A C_s}{3n_{ag}}\left[\left(\frac{3V_w n_{ag}}{4\pi N_A C_s V_T}\right)^{\frac{1}{3}} + t_s\right]^3 \tag{E.8}$$

The thickness of the surfactant layer, t_s, is equivalent to length of the surfactant. The expression for a hydrocarbon chain length $t_s(\text{Å}) = 1.5 + 1.265N$ (Tanford, 1972) is useful when estimating the length of the surfactant, N is the number of carbon atoms in the chain. If the volume fraction of dispersed particles, ϕ is known (from viscosity correlations), then aggregation number, n_{ag}, can be calculated using equation E.8. This in turn permits the determination of water pool radius, r_{wp}:

$$r_{wp} = \left(\frac{3V_w n_{ag}}{4\pi N_A C_s V_T}\right)^{\frac{1}{3}} \tag{E.9}$$

Rearranging Equation E.8 for n_{ag} and substituting the resulting equation into equation E.9 gives:

$$r_{wp} = \left(\frac{V_w}{V_T}\right)^{\frac{1}{3}} \left(\frac{t_s}{\phi^{\frac{1}{3}} - \left(\frac{V_w}{V_T}\right)^{\frac{1}{3}}}\right) \tag{E.10}$$

The volume fraction of suspended particles can also be estimated from known composition of the microemulsions and densities of the respective aqueous and surfactant phases. This approach does not include particle-particle interactions and particle-medium interactions. The known mass of water, m_w, and surfactant phase, m_s, are given by:

$$m_w = V_w \rho_w = \frac{4}{3}\pi r_{wp}^3 \rho_w \tag{E.11}$$

$$m_s = V_s \rho_s = \frac{4}{3}\pi \left(r_{rm}^3 - r_{wp}^3\right) \rho_s \tag{E.12}$$

ρ_w and ρ_s are densities of water and surfactant phases respectively. The water-to-surfactant weight ratio, ω_{wt} is equal to:

$$\frac{m_w}{m_s} = \omega_{wt} = \frac{r_{wp}^3 \rho_w}{\left(r_{rm}^3 - r_{wp}^3\right) \rho_s} \tag{E.13}$$

Rearranging equation E.13 and substituting equation E.3 for r_{wp}:

$$r_{rm}^3 = \frac{\rho_w + \omega_{wt}\rho_s}{\omega_{wt}\rho_s} r_{wp}^3 = \frac{\rho_w + \omega_{wt}\rho_s}{\omega_{wt}\rho_s} \frac{3}{4\pi} V_{wp} \tag{E.14}$$

Substituting equation E.14 into E.2 and then equation E.6 for V_{wp}:

$$V_{rm} = \frac{\rho_w + \omega_{wt}\rho_s}{\omega_{wt}\rho_s} \frac{V_w n_{ag}}{N_A C_s V_T} \tag{E.15}$$

Accordingly, equation E.1 can be re-written as:

$$\phi = \frac{\rho_w + \omega_{wt}\rho_s}{\omega_{wt}\rho_s} \frac{V_w}{V_T} \tag{E.16}$$

It is worth noting that equation E.16 is independent of the aggregation number, n_{ag}. Therefore, reverse micelle size can be estimated without viscosity information directly by substituting equation E.16 into E.10 to obtain:

$$r_{wp} = \frac{t_s}{\left(\frac{\rho_w + \omega\rho_s}{\omega\rho_s}\right)^{\frac{1}{3}} - 1} \tag{E.17}$$

Appendix F

Tables of Selected Results

Table F.1: Selected results of Fischer-Tropsch experiments after 10 min time on stream with Fe/C and Fe/Al_2O_3 catalysts with varied crystallite size prepared via precipitation in water-in-oil microemulsions

	Carbon supported catalyst					Alumina supported catalyst				
Catalyst sample	**C03**	**C05**	**C10**	**C16**	**C19**	**A03**	**A05**	**A08**	**A10**	**A19**
$\bar{d}_{c,l-TEM}$, **nm**	3.0	5.3	10.2	15.6	19.2	3.0	5.0	8.0	9.0	19.2
$S_{g,Fe}$, m^2/g	6.27	3.43	2.97	1.91	1.60	8.16	4.74	3.41	3.31	1.89
GHSV[a]	110	118	116	121	117	290	287	297	300	269
$(H_2/CO)_{inlet}$, **vol/vol**	1.98	1.99	1.98	1.99	1.98	2.00	1.94	2.00	2.00	2.09
Conversion, %										
H_2	43.5	43.1	53.0	44.8	28.8	17.0	18.62	26.9	6.11	13.9
CO	44.8	57.5	75.4	60.5	37.4	17.4	14.74	21.4	6.8	20.1
CO_2-Selectivity, C-%	8.0	18.6	14.9	16.1	18.3	0.0	0.0	0.0	0.0	9.8
r_{FT}[b]	1.80	3.99	6.24	7.94	5.56	1.58	2.25	4.67	1.53	6.17
Partial pressures (reactor exit), bar										
H_2	15.6	16.2	14.8	15.9	17.6	19.4	18.3	18.0	19.6	19.3
CO	7.7	6.1	3.9	5.7	7.8	9.7	9.9	9.7	9.8	8.6
H_2O	5.2	5.1	8.3	5.9	2.9	0.9	1.5	2.2	0.6	1.7
CO_2	0.5	1.5	1.8	1.4	0.9	0.0	0.0	0.0	0.0	0.3
Selectivities of volatile organic compounds, C-%										
n-Paraffins										
C_1	49.3	36.3	26.0	29.5	39.2	29.7	22.1	19.8	19.1	12.7
C_2-C_4	43.5	36.3	44.2	40.3	38.0	17.0	17.5	17.9	13.0	11.7
C_{5+}	0.00	0.00	0.0	1.17	0.0	4.46	12.5	6.27	9.4	10.9
Total	92.7	72.6	70.3	70.9	77.2	51.2	52.1	44.0	41.5	35.3
α-Olefins										
C_2-C_4	3.56	18.3	16.1	16.8	14.3	33.8	27.1	26.9	35.9	31.5
C_{5+}	0.00	0.00	0.00	0.36	0.00	6.29	5.02	5.58	9.5	14.1
Total	3.56	18.3	16.1	17.1	14.3	40.0	32.1	32.5	45.4	45.6
Total β-olefins[c]	1.12	3.68	4.72	5.78	3.10	3.35	5.29	6.01	6.89	3.90
Alcohols										
C_1	1.35	3.19	5.92	2.21	3.83	1.25	1.71	1.50	0.85	0.81
C_2	0.00	0.26	0.00	0.13	0.00	0.84	2.22	1.94	0.23	2.38
C_{3+}	0.00	0.00	0.00	0.21	0.00	0.36	2.28	2.10	0.99	4.47
Total	1.35	3.45	5.92	2.55	3.83	2.45	6.21	5.54	2.06	7.66
Total aldehydes	0.00	0.02	0.00	0.10	0.00	0.66	0.10	6.19	0.58	1.22
Total ketones	0.00	0.00	0.00	0.01	0.00	0.00	0.26	2.97	0.57	1.66
Total iso-cpds[d]	1.22	1.99	2.93	3.57	1.54	2.29	3.94	2.77	2.95	4.63
C_5-Fraction, mol-%										
Ol in lin HCns[e]	na	na	na	65.1	na	72.0	57.1	66.9	69.3	69.4
Ol in iso HCns[f]	na	na	na	54.5	na	76.9	59.1	38.6	75.8	61.5
α-Ol in lin Ol[g]	na	na	na	16.4	na	78.8	69.8	67.3	76.2	90.7
α-Ol in iso Ol[h]	na	na	na	34.9	na	61.6	81.8	84.1	82.4	90.8
Oxyg. in lin HCns[i]	na	na	na	0.00	na	8.6	6.6	14.8	11.4	15.7
iso/n (mol/mol)	na	na	na	0.51	na	0.23	0.19	0.29	0.21	0.23
Chain growth probability, %										
lin HCns ($C_3 - C_7$)	na	na	na	na	na	45.0	51.4	47.2	54.2	57.7
lin HCns ($C_{10} - C_{14}$)	na	na	na	na	na	na	62.9	na	na	na

[a] ml(NTP)$[H_2+CO]/g_{cat}/hr$
[b] formation rate of organic products, μmol-$CO/m^2_{Fe}/s$)
[c] olefins with internal double bonds
[d] branched compounds
[e] molar content of olefins in linear C_5 hydrocarbons
[f] molar content of olefins in branched C_5 hydrocarbons
[g] molar content of α-olefins in linear C_5 olefins
[h] molar content of α-olefins in branched C_5 olefins
[i] molar content of pentanol and pentanal in linear C_5 products

Table F.2: Selected results of Fischer-Tropsch experiments after 60 min time on stream with Fe/C and Fe/Al_2O_3 catalysts with varied crystallite size prepared via precipitation in water-in-oil microemulsions

	Carbon supported catalyst					Alumina supported catalyst				
Catalyst sample	**C03**	**C05**	**C10**	**C16**	**C19**	**A03**	**A05**	**A08**	**A10**	**A19**
$d_{c,l-TEM}$, nm	3.0	5.3	10.2	15.6	19.2	3.0	5.0	8.0	9.0	19.2
$S_{g,Fe}$, m^2/g	6.27	3.43	2.97	1.91	1.60	8.16	4.74	3.41	3.31	1.89
GHSV[a]	110	118	116	121	117	290	287	297	300	269
$(H_2/CO)_{inlet}$, vol/vol	1.98	1.99	1.98	1.99	1.98	2.00	1.94	2.00	2.00	2.09
Conversion, %										
H_2	16.8	49.4	43.2	39.9	34.4	10.5	7.8	14.3	8.3	6.3
CO	18.2	65.0	73.5	53.7	41.7	6.4	8.1	14.4	12.7	13.5
CO_2-Selectivity, C-%	16.4	30.7	25.2	34.3	17.2	0.0	0.6	0.0	0.0	17.0
r_{FT}[b]	0.68	4.24	5.02	6.25	6.47	1.43	1.45	3.69	3.10	7.36
Partial pressures (reactor exit), bar										
H_2	18.2	15.3	14.8	16.1	16.4	19.9	19.1	19.1	19.4	19.7
CO	9.0	5.0	3.9	6.2	7.4	9.4	9.8	9.3	9.2	8.7
H_2O	1.4	4.6	5.9	3.4	3.6	0.6	0.8	1.5	1.3	0.7
CO_2	0.3	2.2	2.3	1.8	0.8	0.0	0.0	0.0	0.0	0.2
Selectivities of volatile organic compounds C-%										
n-Paraffins										
C_1	37.2	24.4	19.8	34.0	26.1	26.6	20.8	22.5	17.5	19.1
C_2-C_4	31.1	28.3	32.1	29.7	31.8	12.7	14.3	16.7	10.0	10.8
C_{5+}	8.9	8.9	11.6	7.3	10.1	5.7	12.6	7.4	10.9	10.3
Total	77.3	61.6	63.5	71.0	68.0	44.9	47.7	46.7	38.4	40.2
α-Olefins										
C_2-C_4	8.9	16.7	13.2	13.2	12.0	29.0	26.9	28.0	31.9	29.5
C_{5+}	0.6	1.6	0.8	0.7	0.9	7.7	7.7	7.5	11.4	12.9
Total	9.51	18.3	14.1	13.8	13.0	36.7	34.6	35.5	43.3	42.4
Total β-olefins[c]	5.25	8.26	8.64	7.22	8.56	3.88	4.54	5.58	5.42	2.60
Alcohols										
C_1	2.59	3.91	4.12	1.83	3.76	1.01	1.01	1.50	0.51	0.46
C_2	0.02	0.02	0.09	0.16	0.04	0.90	2.27	1.35	0.78	1.90
C_{3+}	0.16	0.17	0.11	0.11	0.09	2.44	4.75	3.54	5.20	6.92
Total	2.77	4.10	4.31	2.10	3.89	4.35	8.03	6.39	6.49	9.28
Total aldehydes	0.10	0.17	0.30	0.12	0.29	3.94	1.22	1.97	3.04	2.00
Total ketones	0.35	0.75	0.03	0.05	0.13	2.41	0.44	1.31	0.69	1.17
Total iso-cpds[d]	4.76	6.78	9.16	5.64	6.20	3.77	3.52	2.53	2.65	2.25
C_5-Fraction, mol-%										
Ol in lin HCns[e]	37.5	48.4	42.8	45.7	45.7	71.9	62.9	67.5	69.2	69.0
Ol in iso HCns[f]	46.5	58.1	43.4	50.4	53.2	34.8	53.4	65.2	30.9	53.3
α-Ol in lin Ol[g]	16.7	32.7	15.6	16.3	17.3	81.2	81.4	71.5	83.5	94.5
α-Ol in iso Ol[h]	35.0	48.8	33.6	34.7	35.7	81.7	86.1	88.0	85.2	93.7
Oxyg. in lin HCns[i]	6.32	10.2	0.92	1.53	1.17	13.8	20.1	16.4	23.2	22.4
iso/n (mol/mol)	0.24	0.28	0.36	0.31	0.26	0.29	0.22	0.15	0.16	0.13
Chain growth probability, %										
lin HCns ($C_3 - C_7$)	50.3	50.4	53.2	45.6	51.7	49.9	53.0	48.6	54.0	54.0
lin HCns ($C_{10} - C_{14}$)	na	na	na	na	na	na	67.1	76.8	81.3	70.3

[a] ml(NTP)$[H_2+CO]/g_{cat}/hr$
[b] formation rate of organic products, μmol-$CO/m^2_{Fe}/s$)
[c] olefins with internal double bonds
[d] branched compounds
[e] molar content of olefins in linear C_5 hydrocarbons
[f] molar content of olefins in branched C_5 hydrocarbons
[g] molar content of α-olefins in linear C_5 olefins
[h] molar content of α-olefins in branched C_5 olefins
[i] molar content of pentanol and pentanal in linear C_5 products

Table F.3: Selected results of Fischer-Tropsch experiments after 1500 min time on stream with Fe/C and Fe/Al_2O_3 catalysts with varied crystallite size prepared via precipitation in water-in-oil microemulsions

	Carbon supported catalyst					Alumina supported catalyst				
Catalyst sample	**C03**	**C05**	**C10**	**C16**	**C19**	**A03**	**A05**	**A08**	**A10**	**A19**
$d_{c,l-TEM}$, nm	3.0	5.3	10.2	15.6	19.2	3.0	5.0	8.0	9.0	19.2
$S_{g,Fe}$, m^2/g	6.27	3.43	2.97	1.91	1.60	8.16	4.74	3.41	3.31	1.89
GHSV[a]	110	118	116	121	117	290	287	297	300	269
$(H_2/CO)_{inlet}$, vol/vol	1.98	1.99	1.98	1.99	1.98	2.00	1.94	2.00	2.00	2.09
Conversion, %										
H_2	20.9	40.9	31.5	34.5	23.0	4.6	9.11	13.2	9.46	1.4
CO	23.7	57.5	46.2	44.2	28.5	11.8	10.14	15.9	13.0	10.8
CO_2-Selectivity, C-%	12.1	24.1	21.6	22.4	16.2	0.0	4.0	0.0	0.0	12.8
r_{FT}[b]	0.91	3.72	3.53	5.36	4.34	1.08	1.50	3.45	2.91	3.21
Partial pressures (reactor exit), bar										
H_2	17.7	16.0	17.0	16.7	17.7	20.4	19.1	19.2	19.3	20.2
CO	8.6	5.8	6.8	7.1	8.3	9.4	9.7	9.3	9.3	8.7
H_2O	1.9	3.8	3.2	3.0	2.1	0.2	0.8	1.4	1.2	0.7
CO_2	0.3	1.9	1.3	1.3	0.5	0.0	0.04	0.0	0.0	0.1
Selectivities of volatile organic compounds C-%										
n-Paraffins										
C_1	31.7	27.0	29.5	37.1	31.5	22.7	24.6	22.8	21.1	14.1
C_2-C_4	29.7	25.7	34.0	26.1	26.9	10.4	14.3	15.8	11.2	9.3
C_{5+}	12.84	7.82	10.1	6.40	11.7	6.25	10.8	6.24	9.2	12.2
Total	74.3	60.5	73.5	69.5	70.1	39.3	49.8	44.8	41.6	35.5
α-Olefins										
C_2-C_4	8.45	15.8	9.3	14.3	10.2	27.7	24.9	26.9	29.8	25.1
C_{5+}	0.74	2.38	0.51	0.92	1.10	10.10	8.74	7.64	12.0	16.1
Total	9.18	18.2	9.8	15.2	11.3	37.8	33.6	34.5	41.8	41.2
Total β-olefins[c]	6.64	6.99	5.52	7.24	8.32	3.72	3.63	3.57	3.35	2.80
Alcohols										
C_1	2.79	4.23	2.91	1.77	3.16	0.27	0.98	1.44	0.37	0.40
C_2	0.00	0.13	0.12	0.19	0.00	0.59	3.01	3.73	0.47	0.86
C_{3+}	0.08	0.20	0.07	0.20	0.12	4.15	5.07	4.26	3.61	11.14
Total	2.88	4.56	3.10	2.16	3.28	5.01	9.07	9.43	4.45	12.40
Total aldehydes	0.21	0.79	0.15	0.23	0.16	6.46	0.76	2.18	2.15	2.18
Total ketones	0.08	0.13	0.07	0.09	0.03	4.39	0.54	2.15	0.91	1.61
Total iso-cpds[d]	6.11	7.61	7.02	5.15	6.07	3.29	2.61	3.41	5.76	4.32
C_5-Fraction, mol-%										
Ol in lin HCns[e]	40.1	56.6	36.8	55.4	47.9	72.7	64.1	68.0	69.1	69.4
Ol in iso HCns[f]	41.6	59.9	51.2	57.2	56.6	36.4	59.1	31.5	35.3	44.4
α-Ol in lin Ol[g]	16.8	42.1	14.7	19.1	17.4	86.3	86.0	83.3	92.7	94.8
α-Ol in iso Ol[h]	55.8	59.9	31.8	39.8	35.4	81.9	94.4	92.7	90.1	95.8
Oxyg. in lin HCns[i]	1.38	1.7	1.06	2.03	1.30	30.4	15.8	25.6	22.2	27.8
iso/n (mol/mol)	0.20	0.30	0.31	0.30	0.24	0.28	0.17	0.29	0.40	0.26
Chain growth probability, %										
lin HCns (C_3-C_7)	51.3	45.1	43.1	42.2	51.2	53.4	53.1	48.5	54.9	59.7
lin HCns (C_{10}-C_{14})	na	68.5	68.1	na	na	na	73.2	75.2	72.0	73.5

[a] ml(NTP)$[H_2+CO]/g_{cat}$/hr
[b] formation rate of organic products, μmol-CO/m^2_{Fe}/s)
[c] olefins with internal double bonds
[d] branched compounds
[e] molar content of olefins in linear C_5 hydrocarbons
[f] molar content of olefins in branched C_5 hydrocarbons
[g] molar content of α-olefins in linear C_5 olefins
[h] molar content of α-olefins in branched C_5 olefins
[i] molar content of pentanol and pentanal in linear C_5 products

Table F.4: Selected results of Fischer-Tropsch experiments after 7200 min time on stream with Fe/C and Fe/Al_2O_3 catalysts with varied crystallite size prepared via precipitation in water-in-oil microemulsions

	Carbon supported catalyst					Alumina supported catalyst				
Catalyst sample	**C03**	**C05**	**C10**	**C16**	**C19**	**A03**	**A05**	**A08**	**A10**	**A19**
$d_{c,l-TEM}$, nm	3.0	5.3	10.2	15.6	19.2	3.0	5.0	8.0	9.0	19.2
$S_{g,Fe}$, m^2/g	6.27	3.43	2.97	1.91	1.60	8.16	4.74	3.41	3.31	1.89
GHSV[a]	110	118	116	121	117	290	287	297	300	269
$(H_2/CO)_{inlet}$, vol/vol	1.98	1.99	1.98	1.99	1.98	2.00	1.94	2.00	2.00	2.09
Conversion, %										
H_2	33.8	30.4	37.7	26.7	24.2	5.4	8.15	12.8	8.84	2.0
CO	40.9	47.1	60.1	39.5	31.7	11.8	8.77	16.9	12.9	10.4
CO_2-Selectivity, C-%	15.4	25.7	21.1	23.5	18.5	0.0	7.0	0.0	0.0	11.8
r_{FT}[b]	1.51	2.98	4.23	4.72	4.70	1.07	1.26	3.68	2.90	3.11
Partial pressures (reactor exit), bar										
H_2	16.3	17.2	15.8	16.8	17.6	20.3	19.2	19.2	19.4	20.3
CO	7.3	6.6	5.8	7.0	8.0	9.5	9.9	9.1	9.3	8.8
H_2O	3.3	2.7	4.1	2.3	2.2	0.2	0.7	1.5	1.2	0.7
CO_2	0.8	1.5	1.6	1.1	0.7	0.0	0.1	0.0	0.0	0.1
Selectivities of volatile organic compounds C-%										
n-Paraffins										
C_1	26.7	34.0	31.4	49.7	29.6	20.5	23.8	24.5	18.7	14.1
C_2-C_4	27.1	25.9	25.2	24.1	24.4	8.4	15.6	12.8	12.5	8.6
C_{5+}	12.89	6.78	7.2	4.22	10.8	6.67	10.5	6.52	7.8	6.8
Total	66.7	66.7	63.9	78.0	64.7	35.5	49.9	43.8	39.0	29.5
α-Olefins										
C_2-C_4	8.92	14.3	15.0	10.5	11.1	21.8	26.6	31.3	30.6	19.7
C_{5+}	1.36	1.87	1.75	1.34	1.67	11.72	8.15	8.77	12.5	9.1
Total	10.28	16.1	16.7	11.9	12.8	33.5	34.7	40.0	43.1	28.9
Total β-olefins[c]	9.84	6.64	6.89	4.51	9.61	3.35	3.90	2.93	2.50	2.67
Alcohols										
C_1	3.93	2.72	3.19	1.05	4.28	0.32	1.38	1.29	0.25	0.37
C_2	0.11	0.23	0.80	0.40	0.81	6.24	1.05	2.90	2.89	3.82
C_{3+}	0.18	0.20	0.16	0.22	0.16	5.42	3.13	1.81	5.05	22.12
Total	4.23	3.15	4.15	1.66	5.26	11.98	5.56	6.00	8.19	26.31
Total aldehydes	0.19	0.34	0.17	0.19	0.36	9.16	2.58	2.27	2.24	8.04
Total ketones	0.23	0.16	0.17	0.03	0.06	3.80	1.00	1.93	1.22	1.51
Total iso-cpds[d]	7.37	5.80	6.84	3.23	6.03	2.67	2.35	3.02	3.68	3.03
C_5-Fraction, mol-%										
Ol in lin HCns[e]	50.0	53.4	55.4	57.9	53.0	73.2	63.2	69.6	70.7	70.3
Ol in iso HCns[f]	59.8	58.2	64.3	67.3	60.1	71.8	54.1	32.1	31.1	27.3
α-Ol in lin Ol[g]	16.9	40.4	35.9	42.0	24.2	84.1	82.1	86.9	93.0	90.4
α-Ol in iso Ol[h]	37.0	60.5	51.9	62.0	43.5	92.2	90.3	93.1	95.2	95.0
Oxyg. in lin HCns[i]	1.07	1.3	1.77	2.49	1.15	32.7	10.7	13.3	25.3	31.4
iso/n (mol/mol)	0.23	0.30	0.32	0.26	0.22	0.15	0.13	0.30	0.33	0.38
Chain growth probability, %										
lin HCns (C_3-C_7)	53.8	43.1	44.1	43.9	52.0	55.1	50.5	48.3	53.2	53.9
lin HCns (C_{10}-C_{14})	64.3	65.5	68.4	68.0	60.2	na	72.4	69.5	74.7	77.5

[a] ml(NTP)$[H_2+CO]/g_{cat}$/hr
[b] formation rate of organic products, μmol-CO/m^2_{Fe}/s)
[c] olefins with internal double bonds
[d] branched compounds
[e] molar content of olefins in linear C_5 hydrocarbons
[f] molar content of olefins in branched C_5 hydrocarbons
[g] molar content of α-olefins in linear C_5 olefins
[h] molar content of α-olefins in branched C_5 olefins
[i] molar content of pentanol and pentanal in linear C_5 products

Appendix G

Curriculum Vitae

Name	Evans Itai Mabaso
Date of birth	4th July 1972
Nationality	Zimbabwean
Educational qualifications	
2005 (Submitted)	Ph.D. Chemical Engineering, University of Cape Town, South Africa
2000	M.Sc. Chemical Engineering, University of Cape Town, South Africa
1998	B.Sc. Chemical Engineering, University of Cape Town, South Africa
1992	Advanced Level, Cambridge, Howard High School, Zimbabwe
Awards	
2004	Best Poster Presentation, NANO AFRICA 1, University of Stellenbosch
2003	Travel Grant to Taiwan for IPCAT-3 2003 Conference, University of Cape Town
2001-2004	Chemical Engineering Departmental scholarship, University of Cape Town
2001-2003	National Research Fund grant-holder scholarship, University of Cape Town
1999-2000	Chemical Engineering Departmental scholarship, University of Cape Town
1996-1998	Student scholarship, Zimbabwe Government
1995	University entrance scholarship, University of Cape Town
1994	Deans merit list, UCT
1992	House captain of the year, High School
1991	Old Mutual Mathematics Olympiad Finalist
Offices held	
2003-2004	Interact club manager, Department of Chemical Engineering
2000-2002	Postgraduate representative, Catalysis Research Unit
1990-1992	Senior Prefect, Soccer Captain, High School, Zimbabwe
1990-1992	Patron and President for Mathematics Club, Howard High School, Zimbabwe
Positions of responsibility	
Co-supervisor	S. Mthembu and K. Moeketsi, Honours Project Thesis, UCT, 2001
	S. I. Mazibuko and M. I. Ngubane, Honours Project Thesis, UCT, 2001
	V. Pillay and J. Pai, Honours Project Thesis, UCT, 2002
Mentor	C. Welker from the University of Stuttgart, Germany Research practical, 2002
	R. Prins from Cape Peninsula University of Technology In-service training, 2004
Subwarden	Kilindini Residence, University of Cape Town, 1996
Treasurer	Kilindini Residence committee member, University of Cape Town, 1995
House Captain	Howard High School, Zimbabwe, 1992
Research experience	
2001-2005 Doctoral thesis	Nanosized iron crystallites for Fischer-Tropsch Synthesis
	Supervisor: Dr. Michael Claeys; Co-supervisor: Prof. Eric van Steen
1998-2000 Masters thesis	Ethylbenzene dispropotionation over solid acid catalysts
	Supervisors: A/Prof. Jack Fletcher and Prof. Cyril OConnor
Teaching experience	
2005	Part-time Lecturer in the Department of Chemical Engineering, UCT
2001-2004	Graduate assistant in Catalysis Research Unit, UCT
2000-2003	Teaching assistant in the Department of Mathematics, UCT
1999-2004	Teaching assistant in the Department of Chemical Engineering, UCT
2000-2003	Private tutor at the University of Cape Town